Università degli Studi di Palermo

AREA RICERCA E TRASFERIMENTO TECNOLOGICO
SETTORE DOTTORATI E CONTRATTI PER LA RICERCA
U. O. DOTTORATI DI RICERCA

Dottorato di Ricerca in Tecnologie e Scienze per la Salute dell'Uomo
Dipartimento di Scienze e Tecnologie Biologiche Chimiche e Farmaceutiche (STEBICEF)
SSD CHIM/02

Comparative synthesis and characterization of zinc oxide nanopowders via chemical and biological methods: integration into polymer matrices for surfaces.

IL DOTTORE
Dott.ssa FEDERICA ARCIDIACONO

IL COORDINATORE
Prof. BRUNO GIUSEPPE PIGNATARO

IL TUTOR
Prof. BRUNO GIUSEPPE PIGNATARO

CO-TUTOR
Prof.ssa DELIA CHILLURA MARTINO

CICLO XXXVI
ANNO CONSEGUIMENTO TITOLO 2024.

Università degli Studi di Palermo

AREA RICERCA E TRASFERIMENTO TECNOLOGICO
SETTORE DOTTORATI E CONTRATTI PER LA RICERCA
U. O. DOTTORATI DI RICERCA

Dottorato di Ricerca in Tecnologie e Scienze per la Salute dell'Uomo
Dipartimento di Scienze e Tecnologie Biologiche Chimiche e Farmaceutiche (STEBICEF)
SSD CHIM/02

Comparative synthesis and characterization of zinc oxide nanopowders via chemical and biological methods: integration into polymer matrices for surfaces.

IL DOTTORE
Dott.ssa FEDERICA ARCIDIACONO

IL COORDINATORE
Prof. BRUNO GIUSEPPE PIGNATARO

IL TUTOR
Prof. BRUNO GIUSEPPE PIGNATARO

CO-TUTOR
Prof.ssa DELIA CHILLURA MARTINO

CICLO XXXVI
ANNO CONSEGUIMENTO TITOLO 2024.

ABSTRACT

CHAPTER 1: NANOMATERIALS 1
1.1. NANOMATERIALS 1
1.2. PHYSICAL AND CHEMICAL PROPERTIES 1
1.3. METHODS OF SYNTHESIS 5
1.4. APPLICATIONS 7

CHAPTER 2: ZINC OXIDE 9
2.1. CHEMICAL-PHYSICAL PROPERTIES 9
2.2. SYNTHETIC PROCEDURES FOR ZnO NANOMATERIALS 13
2.2.1. Chemical methods 14
2.2.2. Physical methods 14
2.2.3. Biological method 16
2.3. APPLICATIONS 17

CHAPTER 3: POLYMERIC MATERIALS 20
3.1. CHARACTERISTICS OF A POLYMER 20
3.2. PHYSICAL PROPERTIES 25
3.3. APPLICATIONS 28

CHAPTER 4: MATERIALS AND METHODS 31
4.1. MATERIALS FOR ZnO SYNTHESIS 31
4.2. MATERIALS FOR COPOLYMER SYNTHESIS 31
4.3. CHEMICAL SYNTHESIS OF ZnO 32
4.4. BIOLOGICAL SYNTHESIS OF ZnO 33
4.5. PREPARATION OF YEAST SOLUTION AND IRRADIATION SYSTEM 34
4.6. COPOLYMER SYNTHESIS 35
4.7. COMPOSITE PREPARATION 36
4.8. CHARACTERISATION TECHNIQUES 37
4.8.1. Ultraviolet-visible Spectroscopy 38
4.8.2. X-Ray Diffraction Analysis 38
4.8.3. Scanning electron Microscopy 40
4.8.4. Attenuated total reflectance 41
4.8.5. X-Ray photoelectron spectroscopy 44
4.8.6. Nuclear Magnetic Resonance 47
4.8.7. Photocatalytic activity 49

CHAPTER 5: RESULTS AND DISCUSSION 51
5.1. CHEMICAL SYNTHESIS 51
5.2. BIOLOGICAL SYNTHESIS 65
5.3. COPOLYMER SYNTHESIS 76

CHAPTER 6: PHOTOCATALYTIC TESTS 82
6.1. PHOTOCATALYTIC ACTIVITY OF ZINC OXIDE POWDERS 82
6.2. PHOTOCATALYTIC ACTIVITY OF COPOLYMER/ZnO 91

CONCLUSIONS 94

BIBLIOGRAPHY 96

APPENDIX FIGURES AND TABLES 111

Ph.D ACTIVITIES 115

ABSTRACT

In recent years, nanomaterial science has gained a lot of attention to produce innovative materials with several unique applications; moreover, approaches for nanomaterial production have been studied in depth to obtain new large-scale and cost-effective methods.

This thesis aims to develop and characterize composite materials based on zinc oxide nanoparticles, known for their photocatalytic properties, dispersed into a polymer matrix. These nanoparticles were synthetized using both chemical and biological routes, and the obtained products were characterized and compared through various physical-chemical techniques.

Furthermore, a polymer matrix was synthesized from several components, consisting of polydimethylsiloxane (PDMS), dopamine (Dopa), and isophorone diisocyanate (IPDI), with different chemical and physical properties. This one results in a copolymer with excellent adhesion capabilities.

The following thesis is divided into six chapters, which illustrate the topics covered and explain the techniques used for the synthesis of nanopowders, then describe the work carried out and discuss the results.

In detail, the first chapter introduces the concept of nanotechnology, with particular interest in the development of nanoparticles and the most common applications and production techniques. The second chapter focuses on zinc oxide with a general overview of this catalyst's properties and applications. The third chapter deals with polymeric materials and their characteristics and applications. The fourth chapter highlights the potential of each characterization technique, describing materials and methods used to synthesize and characterize zinc oxide nanoparticles and the polymer matrix.

Results obtained from the characterization are shown in the fifth chapter. Instead, chapter six focuses on the photocatalytic tests performed on the system materials under study.

CHAPTER 1

1. NANOMATERIALS

1.1. NANOMATERIALS

Nanomaterials have at least one dimension in the nanoscale (1-100 nm)[1] and encompass various forms, including nanopowders, nanotubes, thin films, and nanocomposites (Figure 1).

Scaling down to the nanometre level is not just a simple step towards the miniaturisation of matter but a new form in terms of quality and quantity. [2] The matter at the nanoscale no longer exhibits the same behavior as it does at the macroscopic level, mainly attributed to the comparable or great number of surface than internal atoms. [3]

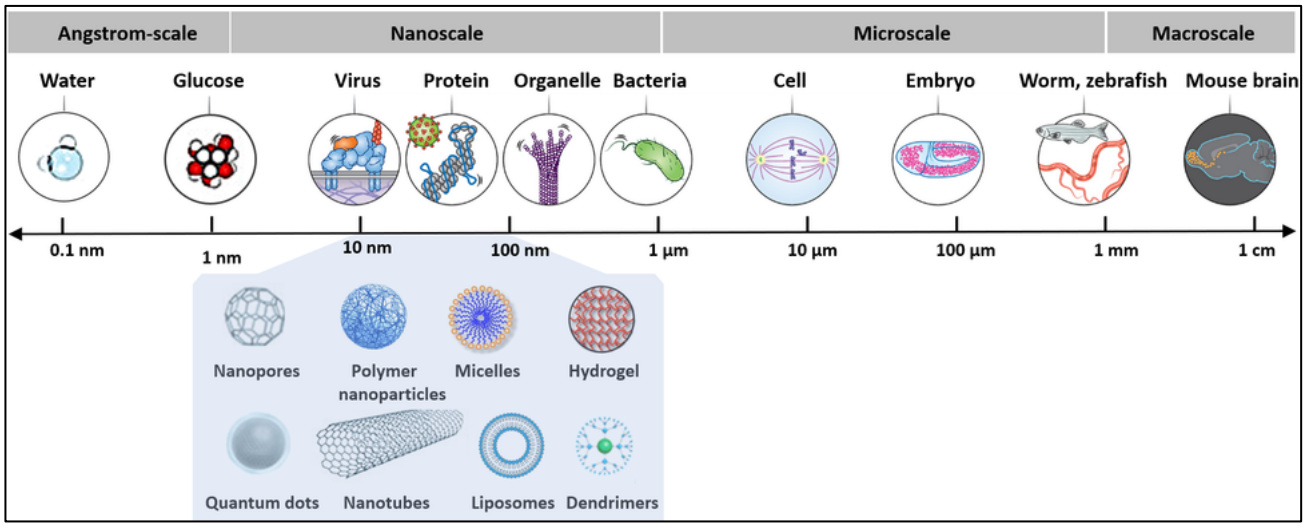

Figure 1. Graphic showing the scale of nanoparticles, including organic compounds, viruses, bacteria, and cells compared to a macroscale.

1.2. PHYSICAL AND CHEMICAL PROPERTIES

Nanoscaled and bulk materials significantly differ in several physical-chemical properties, such as the higher surface area and quantum size effects of the former. These factors, in turn, govern nanomaterials' structural transformations, interaction with light, and even solubility, and enhance their mechanical strength and optical, magnetic, and electrical properties, to name a few.

The atoms near the surface of the nanoscale particles show partial saturation, resulting in an energy state distinct from the rest.[2]

Surface effects are crucial in nanotechnology, especially considering nanomaterials in various states. Nanomaterials in powder form, dispersed in a solvent as colloids, or in thin films display

diverse surface energies and can interact differently with solvents and substrates. Indeed nanomaterials (thin films, dispersed particles, crystalline grains, or coatings) exist in a metastable thermodynamic state stabilized by their interactions with surroundings.[3] These interactions occur at the nanomaterial-surrounding interfaces, which are divided into:

- solid/liquid interface: typical of colloidal nanocrystals and can the inorganic/organic or inorganic/inorganic type.

- solid/solid interface: characteristic of nanocrystals in a solid material, it is generally of the inorganic/inorganic type.[4-5]

For example, metal and semiconductor nanomaterials have different electronic structures than bulk materials and isolated atoms. Various metal nanocrystals feature forbidden bands similar to non-metals, and with decreasing size, the higher proportion of surface atoms increased the reactivity of the particles. The size of nanocrystals directly affects their electronic structure, as shown in Figure 2: unlike bulk materials, the energy levels of electrons in small particles are discrete rather than continuous due to the confinement of the electronic wave functions caused by the physical size of the particles.[6]

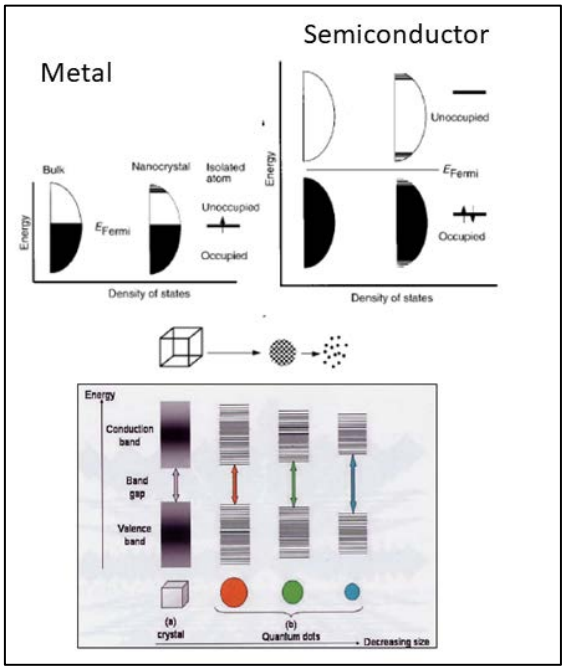

Figure 2: Density of states for metals (left) and semiconductors (right). The Fermi level is in the middle of the band for metals, and kT should exceed the energy jump between levels even at room temperature and for nanometric dimensions. For semiconductors, the jump is larger and increases for smaller sizes (bottom).[6]

Overall, nanomaterials' uniqueness can be rationalized in the following points:

-the high surface area and surface-to-volume ratio determine significantly lower melting points, phase transition temperatures, and lattice constants in nanomaterials.

- minimising the number of nanomaterial defects enables reaching mechanical parameters close to those theoretical andone or two orders of magnitude higher than single crystals.

-the nanomaterial optical properties significantly differ from those of bulk materials. For instance, metal and semiconductor nanomaterials show strong surface plasmon resonance, which depends on their size and shifts the absorption peak, determining their color and, hence, their optical properties. Moreover, the absorbance wavelength of semiconductor nanoparticles shifts to shorter wavelengths due to the increase in the forbidden band;[4]

-the electrical conductivity of nanomaterials proportionally decreases with size due to increased surface scattering, even though it can also increase significantly due to improved microstructural order.

-at the nanoscale, the magnetic properties of nanostructured materials differ significantly from those of bulk materials. The ferromagnetic properties of the latter disappear at a large scale and give way to superparamagnetism due to the high surface energy.[5-6]

-the intrinsic thermodynamic property of nanomaterials and nanostructures is their ability to self-purify from defects. Through successive heat treatments, impurities, structural defects, and dislocations are pushed to the surface and effectively removed. This improvement in structural integrity profoundly affects chemical and physical properties, for instance, improving chemical stability.[7-8]

Generally, nanomaterials are classified into organic nanostructures, such as dendrimers, polymeric nanocarriers, and lipid nanocarriers; metal/plasmonic nanoparticles; semiconducting materials such as quantum dots; and magnetic structures composed of metal, silica, and carbon oxides (nanotubes, graphene, and fullerenes). However, this classification is not always accurate; for instance, organic substances are usually added even to inorganic nanomaterials to stabilize and functionalize them. Thus, nanostructures should be perceived hybrid materials. Nanomaterials can also be distinguished into different categories according to their size and shape. Hence, nanomaterials can be divided in 0D (spheres and clusters), 1D (nanotubes, nanofibres, and nanowires, to name a few), 2D (thin films and surface coatings), and 3D (nanocrystals). As size decreases, the reactivity of nanomaterials increases significantly. In this regard, a 1 nm crystal contains almost 100% of its atoms on the surface, whereas a 10 nm crystal has only 15%. Furthermore, when nanocrystals are small, confinement leads to qualitative changes in their electronic structure, resulting in unique

catalytic properties that differ from those of bulk materials. For example, studying the interaction between silver nanocrystals of different sizes and molecular O_2 revealed that the nanoparticles convert molecular oxygen into atomic oxygen, a phenomenon not observed in bulk materials.

1.3. METHODS OF SYNTHESIS

The synthesis of nanomaterials typically follows two processes: the **top-down** and the **bottom-up** approach. (Figure 3)

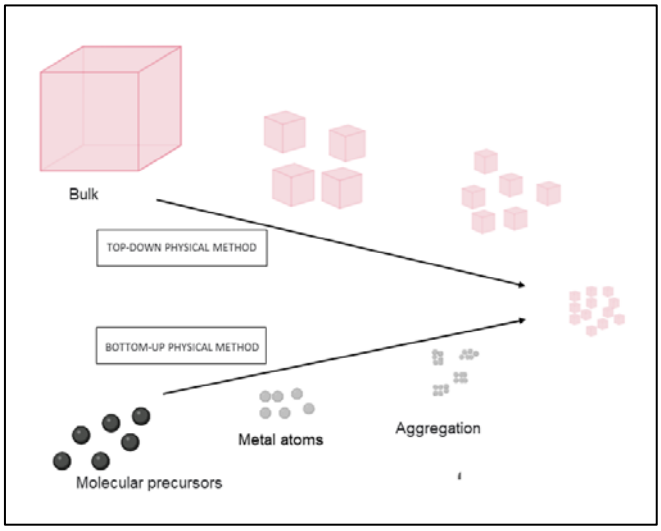

Figure 3. Graphic showing the top-down approach and the bottom-up approach.

The top-down approach involves milling, cyclic cooling, and lithography, to name a few. The milling process enables generating nanoparticles ranging in size from tens to hundreds of nanometres in diameter. However, these nanoparticles have a wide size distribution, possess different morphologies, and may contain impurities from the grinding medium and defects. For instance, when a solid material with low thermal conductivity and high-volume changes in response to temperature variations, the material undergoes cyclic thermal shock and fractures into progressively smaller fragments. This phenomenon can be exploited to produce relatively small particles.[9] However, obtaining particles with specific sizes is challenging, and this method is limited to materials with specific thermal properties. The lithography process involves creating a specific pattern on a substrate by exposing it to light, ions, or electrons and subsequently etching or depositing the material to obtain the desired structure. Although electron and ion beam lithographies offer greater precision and can produce structures with details of less than 10 nm, their low speed and high cost make them impractical for industrial use. As a result, optical lithography remains the most widely used technique despite being less precise.[10]

The bottom-up approach is widely favoured, particularly for nanoparticles. Consequently, many methods have been developed to facilitate this approach. These synthesis methods can be thermodynamically or kinetically controlled. The thermodynamic control involves the

homogeneous nucleation of a chemical species in a very short time, which leads to a sudden supersaturation of the system. Diffusion-controlled growth is then imposed, either by introducing stabilizing polymers into the system or by keeping the concentration of the species in the solution low. Through kinetic control, growth is achieved by spatial control. Nanoparticle growth stops when the species in the system are exhausted. Various confinement systems have been developed for this purpose, including droplets in the vapor or liquid phase and pores in a matrix. Chemical vapor deposition (CVD), often used for carbon-based nanomaterials, involves the chemical reaction of precursors in the vapor phase to form a thin film on the substrate surface. For a precursor to be suitable for CVD, it must have certain characteristics, such as adequate volatility, high chemical purity, stability during evaporation, cost-effectiveness, non-hazardous nature, and long life.[11] In addition, the decomposition of the precursor should not result in the formation of residual impurities. The hydrothermal process is a well-known and widely used method for the synthesis of nanostructured materials, in which a heterogeneous reaction is carried out in an aqueous medium at high pressure and temperature, typically around the critical point, in a sealed vessel. The solvothermal method shares similarities with the hydrothermal method, and the main difference is that the solvothermal method is carried out in a non-aqueous medium. Recently, there has been a significant increase in interest in microwave-assisted hydrothermal methods, which combine the advantages of hydrothermal and microwave techniques. These methods offer interesting and valuable approaches for producing different nanomaterials, such as nanowires, nanotapes, nanosheets, and nanospheres. The sol-gel method is another wet chemical technique commonly used for obtaining various high-quality nanomaterials, and it involves the transformation of a liquid precursor into a sol and then into a gel network structure. This procedure is used to generate metal oxide nanoparticles mostly using metal alkoxides as precursors and includes several steps.[12] First, the metal oxide is hydrolyzed in water or alcohol to form a sol. During the condensation or polycondensation process, hydroxy (M-OH-M) or oxy (M-O-M) bridges are formed and generate metal-hydroxy or metal-oxopolymer in solution. Throughout the aging process, polycondensation occurs continuously, resulting in changes in structure, properties, and porosity. As aging progresses, porosity decreases while the distance between colloidal particles increases. Once aging is complete, water and organic solvents are removed from the gel by drying, and calcination is carried out to obtain nanoparticles. Several factors influence the final nanomaterial product, including precursors, hydrolysis rate, aging time, pH, and molar ratio between H_2O and the precursor. As well as being convenient, the sol-gel method has many advantages. It guarantees the production of homogeneous materials, operates at low processing temperatures, and provides a simple means of producing complex composites and nanostructures.[13]

1.4. APPLICATIONS

Nanomaterials, with their unique properties, enable obtaining more efficient, cost-effective, innovative, and cutting-edge products than those currently used. A multitude of sectors benefit from nanotechnology, as summarized in Figure 4.

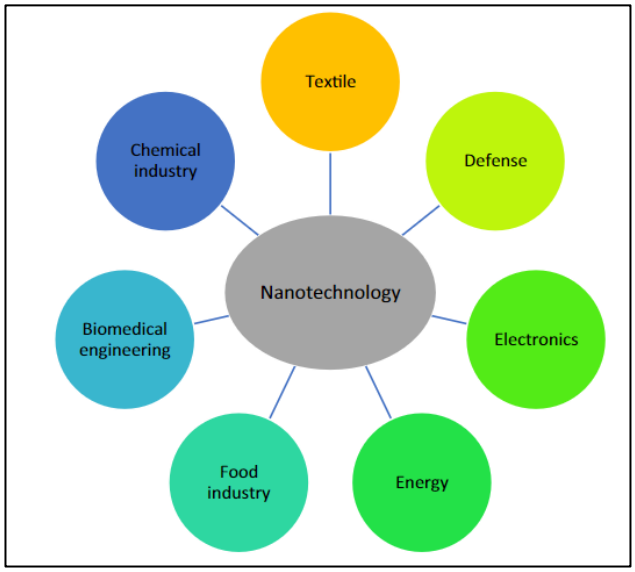

Figure 4. Some relevant areas in which nanotechnologies have found established applications.

For instance, nanomaterials are widely used in paints and wallcoverings to provide surfaces that are easy to clean, scratch, and resistant to microbial attack due to their dirt-repellent properties and exceptional resistance to water penetration. Titanium dioxide (TiO_2), silicon dioxide, and silver nanomaterials are those commonly used in this sector. Nanotechnologies are crucial also for producing light and resistant computer components, reducing their energy consumption, increasing their speed, and improving their data storage capacity. In the textile field, nanomaterials add useful properties to clothing, such as antibacterial protection, UV resistance, and waterproofing (for mountain clothing or tablecloths).

Besides, various personal care products such as sunscreens, moisturizers, hair care articles, and make-up products underwent advances.[14] In sunscreens, TiO_2 and ZnO minerals have been employed for decades as inorganic physical sun blockers, particularly effective in preventing UVB and UVA penetration into the skin, respectively. Nowadays, TiO_2 and ZnO nanomaterials are used in sunscreens to avoid their opaqueness and white-colouring derived from the microsized minerals without reducing their UV-blocking efficacy. Thus, sunscreen products' transparency and cosmetic appeal make people apply them more frequently, ensuring good protection against harmful UV

radiation. The use of nanomaterials in medicine is so intense that an ad-hoc branch of medicine was created - i.e., nanomedicine – in which nanomaterials find application from the diagnosis to the treatment of diseases. Some examples are barium sulfate nanoparticles, which are used as X-ray contrast agents, and nanomaterial drug-delivery systems, where nanotechnology improves the drug's therapeutic by increasing its solubility, absorbability, and distribution in the body, and facilitates the drug's targeted and precise delivery to organs in need of treatment. Nanomaterials are also widely used in food packaging and preservation solutions and as additives to improve food shelf life and yield. Indeed, by incorporating nanomaterials such as nanoclays and TiO_2 in plastic packaging, the latter becomes lighter and more resistant and better limits gas and light contact with the food, preventing its deterioration during storage. Moreover, nanomaterials contribute to the evolution of "smart" packaging through sensors based on nanoparticles that can provide a visual alarm whenever harmful substances in food are present, thus monitoring its state of conservation.[15] Furthermore, nanotechnology can be crucial in addressing several challenges to improve water quality and potability and promote soil health. One of solutions offered by nanotechnology is to use nanoparticles to convert industrial water pollution into harmless substances through chemical reactions. Promising advances in this area include deionization methods using electrodes made of nanoscale fibres. These methods can reduce the costs and energy consumption associated with converting salt water into drinking water.[16]

CHAPTER 2

2. ZINC OXIDE

2.1. CHEMICAL-PHYSICAL PROPERTIES

Recently, zinc oxide (ZnO) has emerged as a highly versatile material renowned for its intrinsic properties such as chemical, thermal, and mechanical stability, remarkable photostability, biocompatibility, and high electrochemical coupling coefficient.[17] Regarding semiconductor classification, zinc oxide falls into the Group II-IV category with an energy gap of 3.37 eV and a binding energy of 60 mV.[18-19] Figure 5 shows the physical properties of this material.

Physical appearance	White, colorless, odorless solid
Crystalline structure	Wurtzite
Molecular Weight	81.38 g/mol
Electron effective mass	60
Melting Point	1,975°C
Density	5.47 g/cm^2
Isoelectric point	9.5–10
Space group	C_{6v}^{4}-$P6_3mc$
Standard molar entropy	43.9 J·K^{-1}mol^{-1}
Standard enthalpy of formation	−348.0 kJ/mol

Figure 5. Physical properties of ZnO.[20]

ZnO has also gained considerable importance in nanotechnology, particularly biomedical and therapeutic applications. Alongside ZnO unique properties, the appeal of this material for nanotechnology relies on the multitude of synthetic procedures available to generate different nanostructure morphologies. ZnO nanomaterials are fundamental for luminescent devices, especially in the green and near UV spectrum[17], light-emitting diodes (LEDs) in both the infrared (IR) and visible spectrum[18], transparent electrode elements for transistors, and solar cells. Crystalline ZnO exists in three forms: zinc blende, wurtzite, and rock salt. The first two forms have a tetrahedral coordination geometry, with each oxygen atom surrounded by four zinc atoms located at the vertices of a tetrahedron and vice versa (Figure 6). Wurtzite ZnO crystallizes in the hexagonal system, while the zinc blend and rock salt forms adopt a cubic system.[20] At standard pressure and

temperature, the thermodynamically stable structure of wurtzite, classified in space group $P_{63}mc$, consists of a hexagonal cell with lattice parameters a=0.325 mm and c=0.521 mm. [21-22]

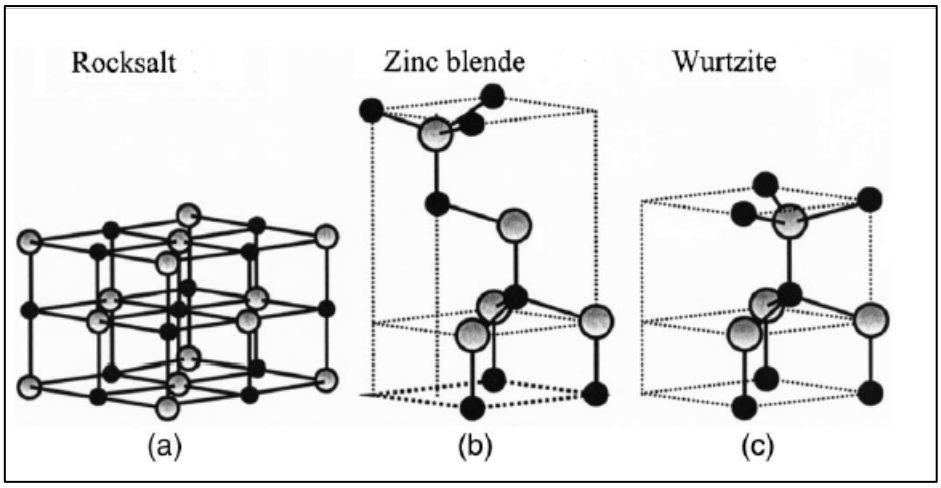

Figure 6. Stick and ball representation of ZnO crystal structures: (a) cubic rocksalt, (b) cubic zinc blende, and (c) hexagonal wurtzite. The shaded grey and black spheres denote Zn and O atoms, respectively.[23]

Figure 7 shows the structure of ZnO wurtzite consisting of two compact interpenetrating hcp sublattices formed by atoms that are displaced from each other along the triple c-axis by an amount of u = 3/8 = 0.375.[22-23] In fractional coordinates, the parameter u represents the bond length parallel to the c-axis, measured in units of c. [22] Each unit cell of the wurtzite structure contains four atoms in each sublattice. Atoms of one type, group II or group VI, are surrounded by four atoms of the other type, forming a tetrahedral coordination at the edges. In real ZnO crystals, however, the wurtzite structure deviates from its ideal arrangement, causing changes in the c/a ratio or u-value. Importantly, there is a significant relationship between the c/a ratio and the u parameter. As the c/a ratio decreases, the u parameter increases, resulting in the maintenance of almost constant tetrahedral spacing despite the distortion of the angles caused by long-range polar interactions.

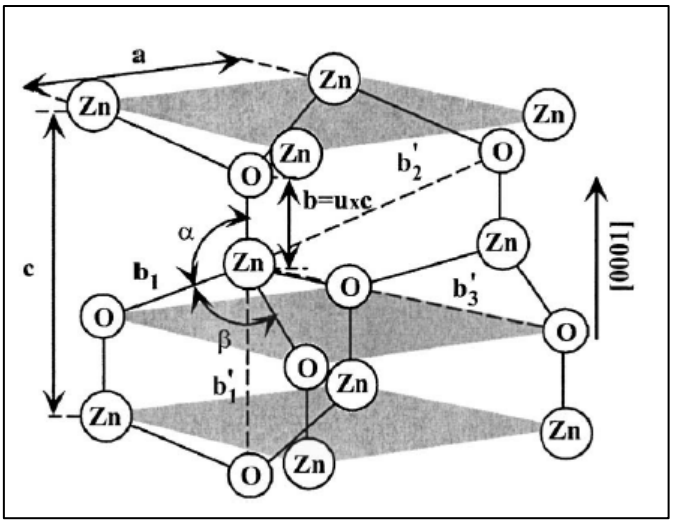

Figure 7. Schematic representation of a wurtzite ZnO structure having lattice constants *a* in the basal plane and *c* in the basal direction; *u* parameter is expressed as the bond length, or the nearest-neighbour distance *b* divided by *c* (0.375 in ideal crystal), and α and β (109.47° in ideal crystal) are the bond angles.[23]

None of the above three structures show inversion symmetry, indicating the crystallographic polarity of the crystal. This polarity determines the direction of the bonds, in particular the closed structure planes (111) in the zinc-blende, as well as the corresponding basal planes (0001). in the wurtzite structure, differ from the planes designated $(\bar{1}\,\bar{1}\,\bar{1})$and $(000\bar{1})$ respectively.[23] By convention, the axis (0001)[24] points from the O plane to the Zn plane, representing the positive z direction. In simpler terms, if the bonds extend from the cation (Zn) to the anion (O) along the c direction, the polarity is that of Zn. Similarly, if the c-direction bonds extend from the anion (O) to the cation (Zn), the polarity is that of O. In the wurtzite structure of ZnO, in addition to the widely used face (0001) and its corresponding growth direction (0001), there are numerous secondary planes and directions within the crystal structure. The crystallographic polarity of wurtzite is evident in the distinction between the plane (0001)and the plane $(000\bar{1})$, resulting in some polar crystallographic directions depending on the presence of Zn^{2+} cations or O^{2-} anions. ZnO crystallographic polarity plays a crucial role in determining various properties, including epitaxy, defect formation, piezoelectricity, and the ability to obtain a wide range of nanostructures.[24] In its solid form, ZnO is white; the colour does not derive from Zn^{2+} due to its d10 electronic configuration, but the presence of defects on the surface is responsible for the d-d transitions that cause the colour change to greenish-yellow. When exposed to high temperatures, ZnO tends to release oxygen, transform into a non-stoichiometric form called $ZnO_{(1-x)}$, and also undergoes a melting process at the high temperature of 1975°C. At temperatures slightly above 1700°C, it can sublime without decomposing, even when exposed to ambient pressure. In terms of electronic band structure, the fusion of the 4s orbitals of Zn^{2+} forms the conduction band, while the valence band is

the combination of the 3d orbitals of Zn^{2+} with the 2p wave functions of O^{2-}.[25] Due to the hexagonal geometry of the crystal field and the presence of spin-orbit coupling, the valence band is split into three distinct energy sublevels at different energy levels. The excitonic binding energies calculated for the three possible combinations between the conduction band and the three valence bands show a striking similarity. Under normal conditions, the photoluminescence spectrum of ZnO can be observed at room temperature, with the emission band showing a significant broadening of about 100 meV centered at 3.37eV. This poorly structured band is due to several events such as interactions between excitons or defects on the surface or dopants that can lead to interaction with excitons.[26] The study and fabrication of nanostructured systems, including thin nanofilms and solid materials with nanoscale crystallites, have made significant progress in this field. These systems have demonstrated high efficiency in stimulated emission. Moreover, ZnO, known for its low toxicity, biocompatibility, and biodegradability, has been deemed safe by the US Food and Drug Administration (FDA).[27]

2.2. SYNTHETIC PROCEDURES FOR ZnO NANOMATERIALS

There are several approaches to obtaining ZnO nanoparticles, depending on the desired morphology and structure for a particular purpose. To date, three kinds of procedures have been identified, namely chemical, physical, and biological methods. Physical methods need expensive equipment, high pressure and temperature, and significant space requirements for installing said the equipment.[28] These methods also produce stable and well-defined nanostructures. The most common approach is the chemical synthesis, which enables the production of nanoparticles with a precise control over their morphology, structure, and chemical properties. Biological approaches have emerged as environmentally friendly alternatives, particularly suitable for medical and pharmaceutical applications.[29] A schematic illustration of the three methods used is shown in Figure 8.

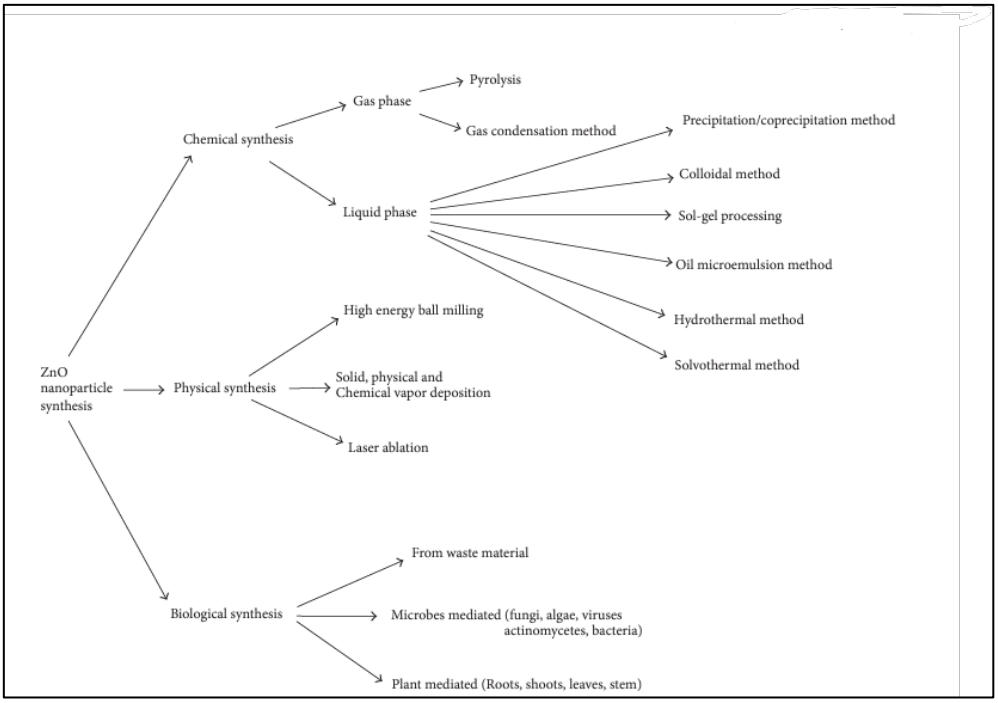

Figure 8. Major synthetic techniques used for ZnO nanoparticle synthesis.[29]

2.2.1. Chemical methods:

ZnO nanomaterials can be synthetized through various chemical methods, classified according to their physical state: solid, liquid, or vapor phase. These approaches use affordable chemical reagents, require basic equipment, and are more cost-effective than physical methods.[21]

- Precipitation methods allow nanomaterials to acquire different properties. Overall, the process involves a reaction between a solution containing zinc salts and a precipitating agent, resulting in the precipitation of the zinc oxide precursor.[19] This step is followed by a heat treatment to promote significant aggregation of the ZnO particles. Several factors, including solution concentration, pH, calcination temperature, and precipitation time, play a crucial role in regulating the different morphologies of zinc oxide.
- The sol-gel technique involves the creation of colloidal solutions that undergo a gel transformation. Metal alkoxides are used as precursors and undergo condensation, polymerization, and hydrolysis reactions to achieve the desired result. The development of nanoparticles by the sol-gel method is influenced by several factors, including the characteristics of the alkyl group and the solvent, as well as the concentration and temperature of the solvent.[21] Although this method is suitable for industrial production, it has the disadvantage of relying on expensive synthetic precursors.
- Hydrothermal methods required an autoclave and the heating of the substrate mixture at temperatures between 100 and 130 °C. Yet, these approaches do not need organic solvents or the final calcination step to obtain nanomaterials, as the cooling phase initiates their nucleation and growth. The size and morphology of the nanoparticles are determined by the composition of the initial mixture and the operating parameters of the process.[22] This process results in a final product with remarkable crystallinity and purity.

2.2.2. Physical methods

Physical methods include several processes, such as chemical and physical vapor deposition, ultrasonic irradiation, thermal evaporation, and laser ablation.

- Chemical vapor deposition (CVD) is very popular method to obtain and grow ZnO crystals on a substrate. The process can be divided into five distinct phases, as shown in Figure 9.

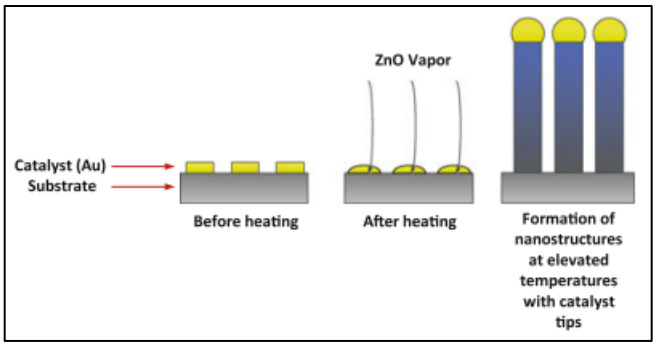

Figure 9. Diagram of vapor–liquid–solid deposition. The Au catalyst forms eutectic alloy drops that become supersaturated allowing for ZnO nanowires to form. [30]

In the initial and subsequent stages, the reactants disperse and adhere to the adsorbent substrate, followed by a surface chemical reaction that forms a solid deposit. At elevated temperatures, the gaseous by-products desorb from the surface, which occurs at higher temperatures than in the physical deposition process.[30] There are different types CVD, such as atmospheric pressure chemical vapor deposition (APCVD), low-pressure chemical vapor deposition (LPCVD), and plasma chemical vapor deposition (PECVD).

- In the physical vapor deposition (PVD) process, the material, typically in a sublimated state, is introduced into an oven (as shown in Figure 10) where it is heated to two different temperatures.

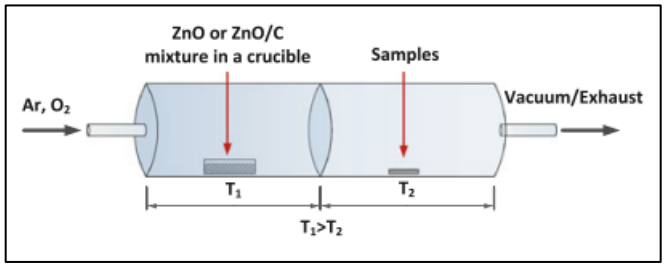

Figure 10. Diagram of physical vapor deposition. The two-temperature zone furnace consists of high temperature zone where sublimation occurs and a low-temperature zone where sublimated ZnO deposits onto the substrates. Ar is usually used as the carrier while O2 is used as the reactant gas. [30]

ZnO sublimates in the higher temperature zone and is then deposited onto the substrate under lower temperature conditions. To facilitate the ZnO transport between the two regions of the furnace, air is used as a carrier.

2.2.3. Biological method

Using biological organisms such as plants, bacteria, algae, and fungi (as shown in Figure 11), biological ZnO synthesis techniques offer many advantages over traditional chemical methods, the most important being their environmental friendliness, as they do not require toxic chemicals. Biological processes require specific conditions, including careful selection of organisms, appropriate culture media, and precise temperature and pH levels[21].

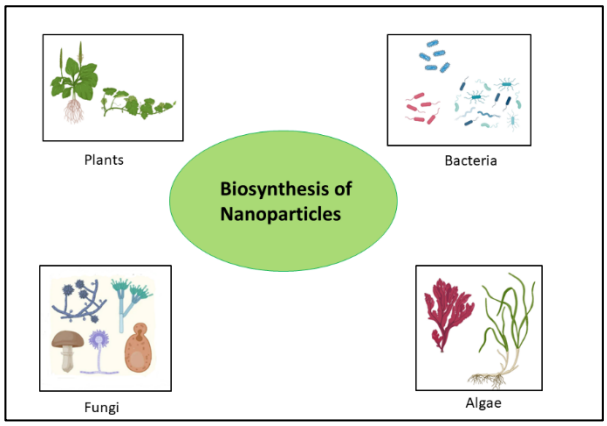

Figure 11. Precursors for the biosynthesis of ZnO nanoparticles

The literature[21] identifies two different methods of microbial synthesis: intracellular and extracellular. In intracellular production, ions are transported inside the bacterial cells where enzymes facilitate the formation of nanoparticles. Extracellular synthesis involves the interaction between the ions on the bacterial cell surface and the bioactive compounds released, resulting in the formation of oxide particles. Microorganisms such as *Lactobacillus sporogenes* and *Candida albicans* are particularly suited to ZnO synthesis, resulting in the growth of nanoparticles with diameters between 15 and 25 nm.[31]

2.3. APPLICATIONS

The wide use of ZnO in nanotechnology is due to its ability to adopt a variety of nanostructures through different synthesis methods. These structures can manifest themselves in one-dimensional (1D), two-dimensional (2D), and three-dimensional (3D) forms, such as nanomoles, nano rings, nanowires, nanopellets, nanowires and nanoplates, as shown in Figure 12.

.

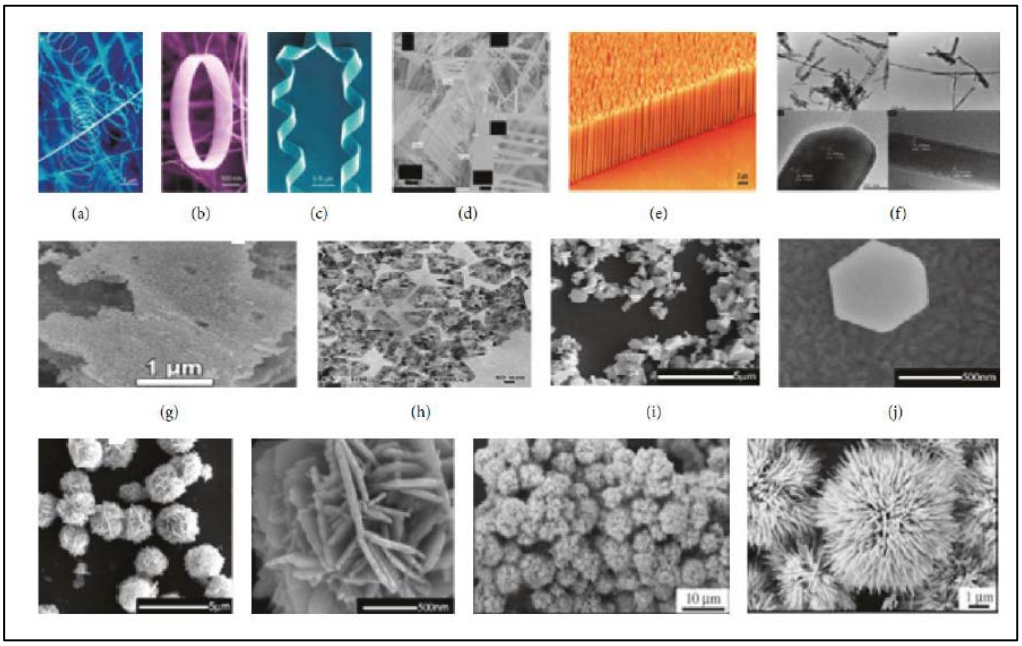

Figure.12. Different structures of ZnO; one dimension: (a) nanospings, (b) nanorings, (c) nanohelix, (d) nanocombs, (e) nanowires, (f) nanorods; two sizes: (g) nanosheets, (h) nanopellets, (i) nanoplates; three dimensions: (k) and (l) nanoflowers, (m) nanomesosphere; (n) nanourchins.[20]

To date, ZnO nanomaterials have found applications in a wide range of industries, from tire manufacturing to ceramics, from pharmaceuticals to agriculture, from paints to chemicals. Moreover, ZnO nanomaterials' antibacterial, disinfectant, and desiccant properties make them a common ingredient in the manufacture of various medicines. (Figure 13).

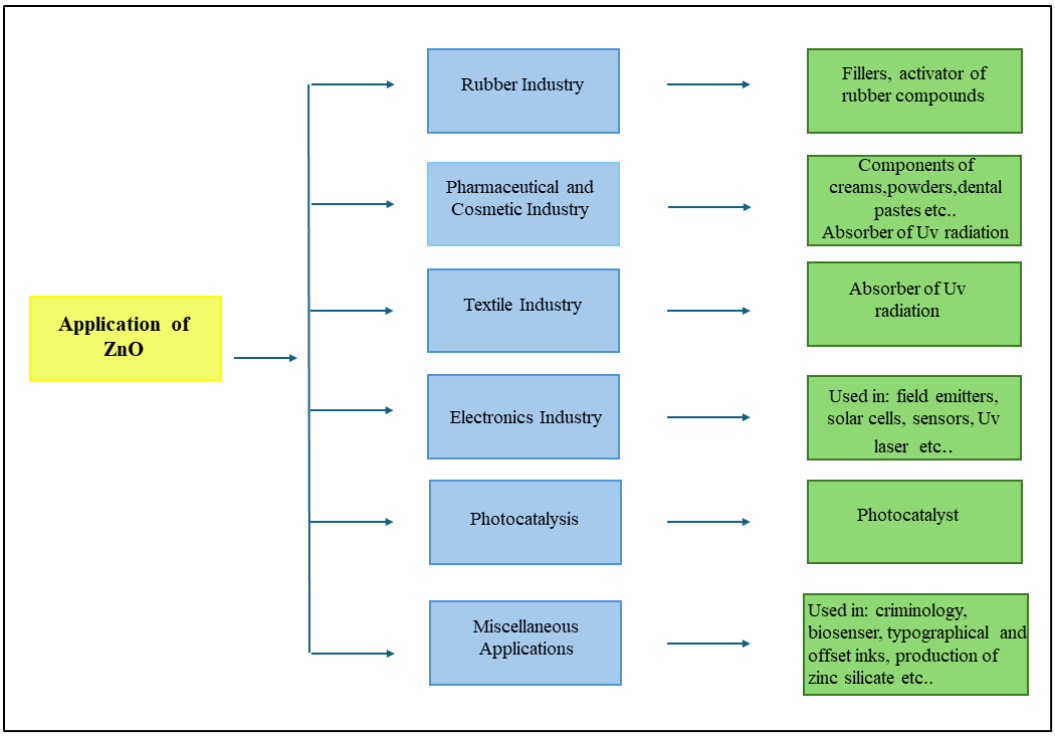

Figure 13. Applications of nano-structured zinc oxide

In particular, ZnO nanostructures have been used as an oral medication for epilepsy and promote faster wound healing, favouring their use in dermatological products to combat inflammation and itching. In higher concentrations, ZnO also has a peeling effect.

In textiles, nanostructured ZnO coatings are more effective at blocking UV radiation and allowing air permeability than their bulk counterparts, [32-33] making the former highly desirable for UV-protective textile coatings.[34-36] Indeed, various methods have been developed to produce UV-protected textiles using ZnO nanostructures. For example, ZnO nanoparticles hydrothermally grown on SiO_2-coated cotton fabric showed excellent UV-blocking properties.[37-39] Significant advances in UV absorption have been made by synthesizing ZnO nanoparticles in a homogeneous phase reaction at high temperatures and then applying them to cotton and wool fabrics or growing arrays of ZnO nano bars on a fibrous substrate using a low-temperature growth technique.[40]

The study of ZnO nanostructures in photocatalysis has also become a focus of scientific research in recent years. Photocatalysis is the process by which light-triggered oxidation or reduction reactions on the surface of a catalyst generate an electron-lacuna pair. In the presence of a photocatalyst, an organic pollutant can be oxidized directly through a photogenerated gap or indirectly through interactions with reactive groups (ROS), such as the hydroxyl radical OH- formed in solution. TiO_2 and ZnO are the most used catalysts.[41] Under UV light intensity, TiO_2 exhibits photocatalytic properties. Although ZnO offers comparable or even higher activity than TiO_2, it is more prone to instability and less susceptible to photo corrosion.[42] Nanosized ZnO, on

the other hand, offers greater stability due to improved crystallinity and reduced defects. Adding other components can enhance the photocatalytic activity of ZnO and extend its range into the visible spectrum.[43] The extraordinary properties of various nanostructures, including ZnO nanowires, nanotubes, and nanoporous materials, have attracted considerable interest in electrochemical biosensing. These advances have proven beneficial in biosensor applications due to their non-toxicity, biosafety, excellent biocompatibility, high electron transfer rate, improved analytical performance, enhanced sensitivity, ease of fabrication, and cost-effectiveness.[44-46] In addition, ZnO has a high isoelectric point (IEP) of around 9.5, making it an ideal substrate for immobilizing low IEP proteins or enzymes such as uricase (IEP ~ 4.6) at a physiological pH of 7.4.[47-49] In addition, ZnO exhibits strong ionic binding (60%) and has minimal dissolution at biological pH values.[50] Numerous researchers have investigated the relationship between the size of inorganic antibacterial agents and their biological activity, and the use of nanocrystalline metal oxides in molecular biology applications is of great interest due to their ability to achieve exceptionally high surface areas.[51-52] Antimicrobial agents based on inorganic chemistry have demonstrated significant efficacy in therapeutic applications.

Padmavathy et al.[53-54] found that ZnO nanoparticles with particle sizes between 0.1 and 1 μm exhibit greater abrasiveness than bulk ZnO. This higher abrasiveness leads to greater mechanical damage to the cell membrane, resulting in a more potent bactericidal effect. The field of nano- and micro-sized oxide materials is experiencing rapid growth, with advances in technology and knowledge occurring at an accelerated rate. These substances can be used to achieve various benefits, such as ceramics with longer lifetimes, transparent sunscreens that effectively shield against both infrared and ultraviolet radiation, and the production of catalysts. These materials also play a vital role in biomedical research, helping to diagnose and treat disease. They can transport drugs directly to the affected cells, minimizing potential side effects.

CHAPTER 3

3. POLYMERIC MATERIALS

3.1. CHARACTERISTIC OF A POLYMER

Polymeric materials are indispensable in numerous aspects of our daily lives. Their unique properties make them valuable and often preferred over conventional materials, resulting in their widespread use in various industries, including construction, food, pharmaceuticals, textiles, medicine, sports, and transportation. The properties of polymers can differ significantly between different materials; thus, it is crucial to understand their structure and behaviour under specific conditions before using them in a particular application.[55]

Polymers are organic substances composed of macromolecules with a significantly high molecular weight. These macromolecules are formed through the repetition of a specific group of atoms known as a "repeating unit”. Most polymers used in modern times are created through synthesis, starting from low molecular weight molecules called "monomers". However, a small part of polymers is derived from natural substances through chemical processes. There are various ways to classify polymers, and the classifications depend on structure, polymerization mechanism, preparation techniques, and thermal behaviour. The origin of the polymer (whether natural or synthetic) is the most obvious basis for classification.[56]

- Natural: Cellulose, and nucleic acids are examples of natural substances found in nature.. These latter are complex polymers derived from biological sources. However, polymers such as cellulose, starch, and natural rubber, which are derived from plants, have a relatively simple structure.[57]
- Synthetic: combining monomers through chemical reactions enables generating several polymers, which can be grouped into different categories, such as fibers, elastomers, plastics, adhesives, resins, and rubbers. Polymers can also be classified according to the chemical composition of their constituent units, which are derived from low molecular weight precursors.

This classification leads to the formation of two major groups:

- Organic polymers (carbon is the main atom in the chain).
- inorganic polymers (the main atom in the chain is not carbon).

Comparing the two classes, organic polymers have some differences from their inorganic counterparts.

Organic polymers tend to decompose or melt at low temperatures, mainly due to the reaction between carbon and oxygen atoms. They also tend to swell or melt when exposed to hot solvents or mineral oils, making them unsuitable for applications such as the automotive industry. In addition, organic polymers often lack elasticity or rubbery properties over a wide range of temperatures and are not sufficiently resistant to ultraviolet radiation. By classifying these materials according to their structural characteristics, a subdivision can be made (Figure 14).

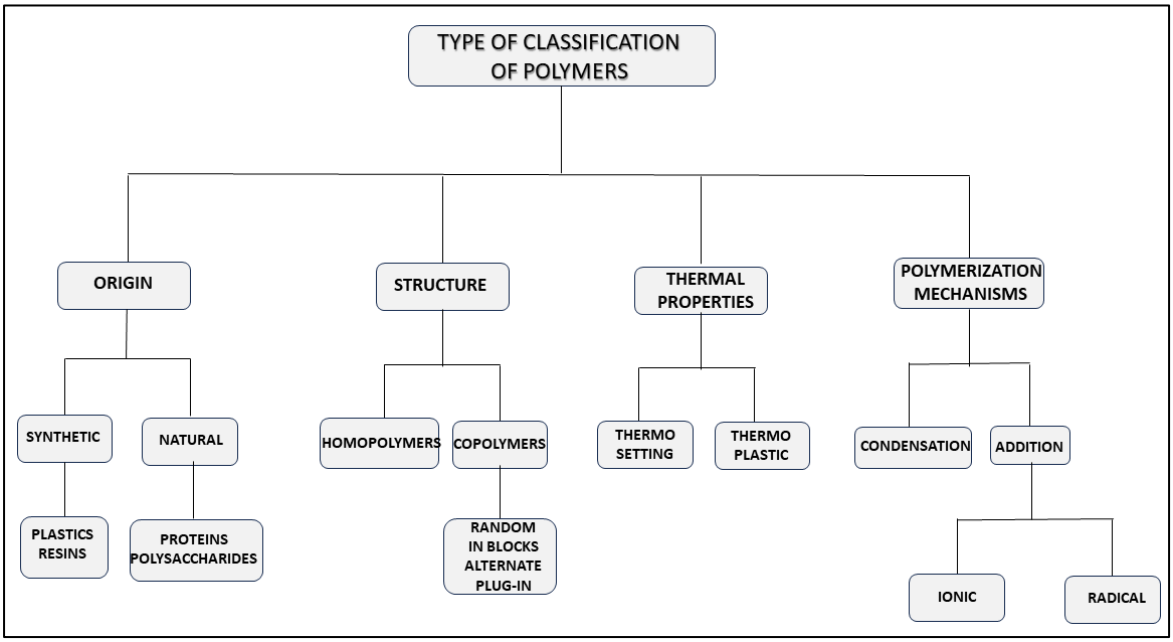

Figure 14. Classification of polymeric materials.

Polymers can also be classified according to the arrangement and displacement of repeating units within the macromolecule. Linear polymers develop in a specific direction. A polymer with a linear structure is characterized by long, filamentous, intertwined macromolecules, the linearity of which results from the arrangement of the constituent structural units.[58] Cross-linked polymers, as illustrated in Figure 15, can be linked to sets of chains connected by intermolecular cross-links, resulting in a dense, immobile, and insoluble three-dimensional network.

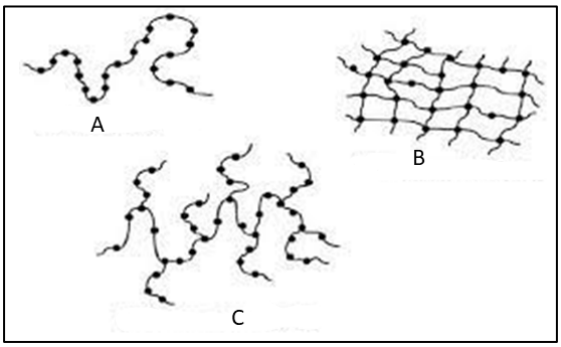

Figure 15. Macromolecular structures of polymers: a) linear, b) cross-linked c) branched.[58]

In terms of structure, polymers can exist in a solid state, although chains mobility and spatial arrangement prevent them from packing together neatly and forming a crystal structure (see Figure 16). Polymethyl methacrylate (PMMA), attactic polystyrene, polyisopropene, polybutadiene, and polycarbonate (PC) are among the first examples of amorphous polymers.[59]

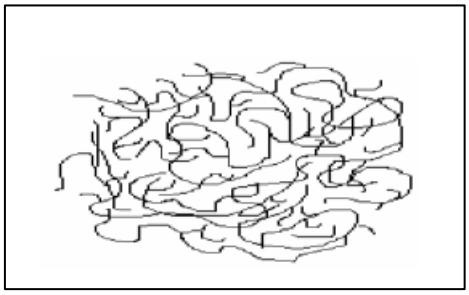

Figure 16 Amorphous polymer.[59]

In crystalline polymers, portion of the chains can be arranged in lamellar crystals about 10-20 nm thick, with parallel chains perpendicular to the crystal surface. Consisting of interconnected chains, these structures form crystalline substructures but also contain amorphous regions, leading to their more accurate classification as semi-crystalline, with their unique spherulitic structure, in which lamellar regions are formed in three directions.[60]

The arrangement of the monomers along the polymer chain determines their classification as homopolymers or copolymers. In the former case, the chain is composed of repeating units of the same monomer. A good example of a homopolymer is polypropylene.

Copolymers, on the other hand, are formed by the repetition of two or more monomers, resulting in the formation of chains. The incorporation of a second monomer into the primary polymer chain allows the manipulation of many properties of significant practical importance, even when the second component is present in small quantities. The position of the second monomer, its proportionate concentration, and the impact of the second component on both the synthesis process and the final structure of the macromolecule are factors that affect the reaction mechanism and the configuration of the chains in the solid phase, thus exerting a profound influence on the physical and chemical properties of the copolymer. To fully understand the structure of a copolymer, it is necessary to determine several parameters and be able to calculate them using kinetic or statistical models,[61] which provide information on the linking processes of the monomer units and their distribution within the chains.

Firstly, it is important to determine the relative amounts of monomers A and B and their distribution. In addition, the nature of the repeating units derived from monomers A and B should be compared with the intrinsic properties of each monomer. The order of incorporation of monomer A about

monomer B, the size of polymer chains and their distribution, and the occurrence of branching, cyclization, or cross-linking are also fundamental features of copolymers. The former influences the formation of monomer sequences of different lengths and their distribution whereas the latter may result from uncontrolled processes. Moreover, to determine the size of the chain, it is necessary to measure directly the propagation and termination rate constants from which the above quantities can be derived. Copolymers can be classified into four main groups, namely statistical or random, alternating, grafted, and … copolymers. Statistical or random copolymers exhibit a random arrangement of monomers according to the principles of the first-order Markov statistical distribution.[62]

A+B→ …… ABBABAAABABBABAABABBABA……

Alternating copolymers, on the other hand, have a regular and alternating distribution of comonomers.

A + B → … ABABABABABABABABABABABABABABA……

Grafted copolymers have chains of one comonomer hanging from the backbone of the other.

```
A + B →   —A—A—A—A—A—A—A—A—A—
              |         |
              B         B
              |         |
              B         B
              |
              B
```

The synthesis of these copolymers presents several challenges and there are various types of copolymers, each with its own unique characteristics and industrial significance.

Polymeric materials are obtained through the polymerization process, which involves the combination of multiple monomeric molecules. This process allows monomers to join together and form new molecules. The resulting polymer can be called a dimer, trimer, tetramer, or higher depending on the number of monomers present. Macromolecules are formed when the molecular weight exceeds 5000 Daltons.[63]

Regarding the polymerization mechanisms, a differentiation is established between condensation polymers and addition polymers.

In condensation polymer, the polymer chain is formed through the condensation of monomer units and the release of small molecules such as water or alcohol. Polyamides (nylon) 6,6, polyesters (polyethylene terephthalate, urea-formaldehyde, and phenol-formaldehyde resins), polysaccharides (starch, cellulose, and hyaluronic acid), and proteins (enzymes, cytochrome, haemoglobin, myoglobin, collagen, elastin, and more) are all examples of condensation polymers.

Addition polymers refer to a specific type of polymer in which the structural unit, or a multiple thereof, aligns with the starting monomer, and the overall molecular weight of the polymer is determined solely by the combined molecular weights of the monomers within the chain. Polystyrene, polyethylene, polyacrylonitrile, polymethyl methacrylate, and polyvinyl chloride are all examples of additional polymers.[64]

3.2. PHYSICAL PROPERTIES

In terms of chemical-physical properties, we encounter highly soluble and fusible polymers, as well as those with notable resistance to temperature and solvents. Additionally, polymers can vary in transparency: some are transparent, some are translucent, and some are even opaque. These properties are to be attributed to the polymers' chemical composition, including the atoms' arrangement within the structural unit. Furthermore, these features can also be influenced by larger-scale structural characteristics, such as the average length of the macromolecules and the presence of any branching [65] and kinetic and technological processes used to create the superstructure, such as the formation of lamellae or spherulites. It is crucial to consider polymers' molecular weight, any deviations from the linear nature of the macromolecules in the chain, the polarity of the bonds, and the level of crystallinity and molecular cohesion. Unlike other substances, polymers do not have a specific molecular weight, since the number of monomer units can vary depending on the polymerization process. Therefore, the focus is on average molecular weight rather than a fixed value, which is measured by the Degree of Polymerization (DP) – i.e., the number of monomer units per polymer chain. The DP influences polymer's mechanical properties; indeed, an increased DP in linear polymers improves both the constraints that bind the chains together and those that oppose sliding when the material is under tension, resulting in better mechanical properties of the material.[61]

The properties of a polymer are not only affected by its molecular weight; the structural configuration of molecular chains also plays a significant role. The characteristics of the material are determined by the three-dimensional arrangement of the polymer molecules. Chemical compounds having the same brute composition and formula but differing in structure, resulting in distinct chemical properties due to different molecular bonds, are called structural isomers or stereoisomers (Figure 17).

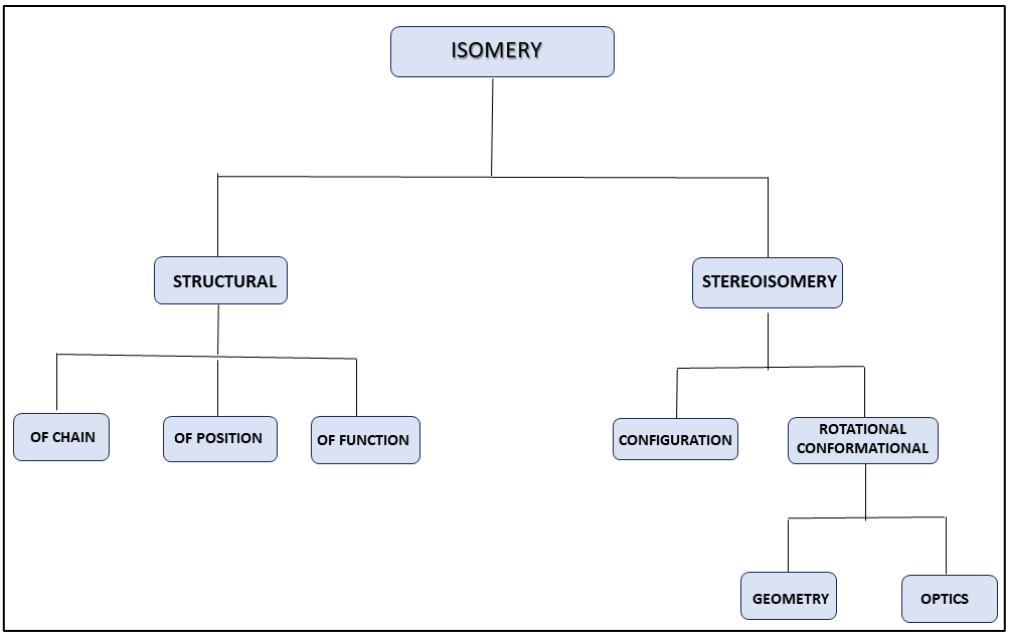

Figure 17. Different types of isomerism

When considering the composition of a polymer, it is important to note that it consists of macromolecules bound together by covalent bonds, forming a cohesive set. These macromolecules are further linked through secondary chemical bonds, such as van der Waals forces and dipole-dipole interactions. In addition, there may be transverse chains, which serve to connect different macromolecules.

Temperature plays a crucial role in shaping the characteristics of materials, including polymers (Figure 18). However, unlike crystalline materials that pass directly from solid to liquid when they reach the melting point, the process is more complex for amorphous or poorly crystalline materials. This complexity comes from the limited movement of the molecules that make up these materials. As the temperature increases, amorphous polymeric materials undergo two distinct transitions, known as glass transition (T_g) and softening (T_r). The glass transition (Tg) marks the transition from a relatively rigid state (called the glass state) to a highly flexible state known as the gummy state. The temperature Trmarks the point of passage from the gummy to the liquid state. When it comes to partially crystalline polymers, the mechanical properties[66] are minimally affected by the glass transition. However, these properties deteriorate significantly when the polymer melts at its melting temperature, Tm.[67]

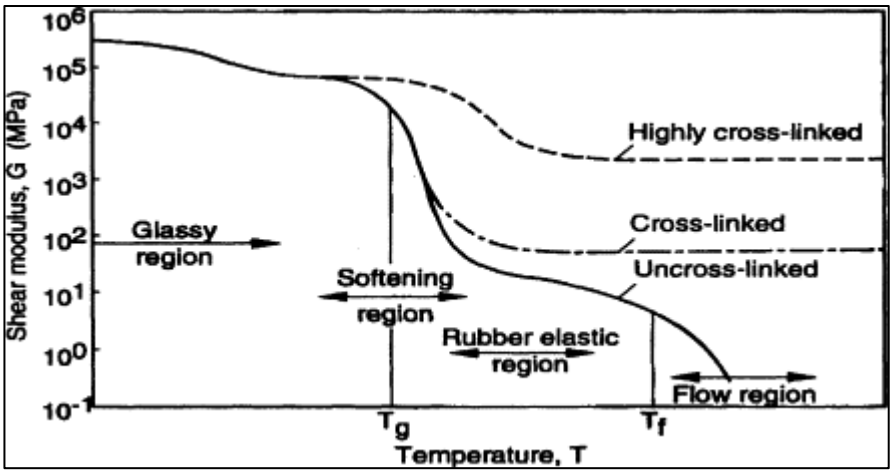

Figure 18. The physical state of polymeric materials as a function of temperature: state transitions.[67]

Glass transition and softening temperatures are of great technological and application interest.
In various production processes, it is crucial to keep the polymer in the temperature range between Tg and Tr. For example, polymethylmethacrylate (PMMA), a rigid polymer, has glass transition temperatures well above room temperature. In contrast, rubber materials have glass transition temperatures below room temperature, making them rigid in colder environments and increasingly flexible when the temperature approaches room temperature. The classification of polymers in thermoplastics and thermosets is mainly determined by the behaviours described above.[68]

On the other hand, polymers cross-linked three-dimensionally do not undergo glass transitions or softening. These materials show no significant changes in properties as the temperature increases until the chemical stability limit (T_L) is reached. Beyond this limit, transformations and/or irreversible degradation occur resulting in loss of the mechanical qualities of the polymer.

3.3. APPLICATIONS

In various fields of application, polymers, with their unique properties, emerged as unquestionably superior materials, becoming the epitome of innovation in the 21st century (Figure 19).

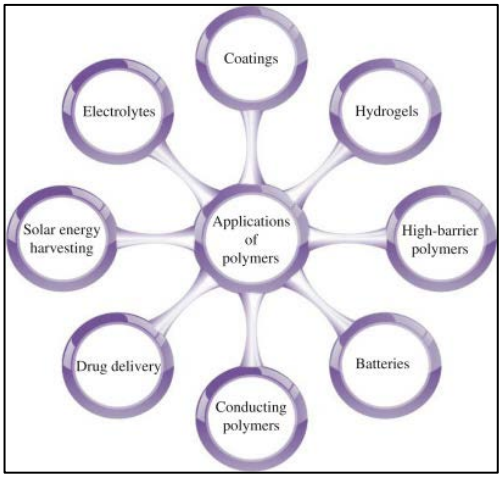

Figure 19. Applications of polymers.

Combining polymers with other materials to form composites often reinforces the latter and optimizes their performance. Consequently, creating polymer matrix composites (PMCs) has proven to be an effective approach to modifying polymer properties.[69] The matrix in PMCs can consist of organic or inorganic polymers, while the reinforcing material can be short or continuous fibres or particles ranging from a few millimetres to the nanometre range. Its main function is to hold the fibres together, transmit to them loads, and distribute them evenly. Conversely, the fibres act as the primary load-bearing element due to their superior strength and modulus.

The combination of polymers with other materialsoffer a range of remarkable properties including lightweight, impressive stiffness, exceptional strength-to-weight ratio, excellent fatigue, wear and corrosion resistance, ease of manufacture, cost-effectiveness, great design versatility, and desirable thermal expansion characteristics.[70-71] These properties make PMCs highly desirable composite materials in a wide range of industries such as automotive, aerospace, medical, civil engineering, electronics, communications, sports, marine, military, energy, industrial, construction, and various household goods applications.[72] Compared to other composites, PMCs are known for their relatively low processing temperatures, making them much easier to manufacture.

The automotive industry appears to be one of the largest users of PMCs due to cost savings and lightweight properties. In vehicle design, the mechanical properties offered by PMCs play a crucial role in meeting the pressing need to reduce the overall weight of cars. This weight reduction

improves fuel efficiency and reduces exhaust emissions, thus helping combat air pollution. Natural fibre polymer composites are the perfect materials for such applications due to their lightweight, impressive strength and stiffness, flexible design possibilities, excellent energy absorption capabilities, effective noise and vibration reduction, corrosion and abrasion resistance, affordability, and biodegradability.[73-75] In the automotive sector, PMCs are used in various components such as door panels, bumper systems, dashboards, roof racks, and chassis. The aerospace industry is a major user of advanced composites.[76-78] Similar to the automotive industry, weight reduction, cost savings, and radiation protection are key considerations for these materials in aerospace. The importance of weight reduction cannot be overstated, as it impacts several factors, including fuel efficiency, speed, number of components, manoeuvrability, and increased range. The aerospace industry benefits greatly from the lightweight nature of polymers, resulting in reduced weight and fuel consumption. Extensive research into nano-reinforced polymer matrices has demonstrated their superior radiation shielding capabilities compared to metallic alternatives. Aluminium is no longer effective for this purpose due to its low electron density and the production of secondary particles. Polymer composites, on the other hand, offer superior shielding capabilities, as they have insulating properties and can be designed with high-Z fillers that are non-toxic and provide better protection against X-rays.[78] Silicone rubber, for example, is widely used in aircraft because of its excellent performance at different temperatures, its resistance to radiation, chemicals, and aging, and its unique electrical insulation properties, while carbon nanoparticles such as graphene, carbon nanotubes, and carbon black have excellent resistance to oxidation in the presence of air.[78-79]

The medical field is at the forefront of exploiting the latest discoveries in polymer composites, which find application for hard and soft tissues, such as bone and skin.[79-83] The remarkable properties of these materials, alongside their biodegradability, biocompatibility, biomimetic properties, and bioresorbability, have led to their widespread use in biomedical applications, such as wound dressings, medical devices, tissue engineering, dental applications, oral tissues, protein immobilization, drug delivery, regenerative medicine, bone and ligament applications, blood vessels, antimicrobial materials, and surgical implants.[79] A wide variety of natural and synthetic polymers are used in biomedicine, including chitosan, collagen, guar gum, alginates, agar, pectin, psyllium, pullulan, starch, cellulose, polyamide (PA), polyglycolic acid (PGA), polylactic acid (PLA), polycaprolactone (PCL), polylactic-co-glycolic acid (PLGA), and polyester amides (PEA). These polymers are often reinforced with fibres.

The use of advanced composites in the marine industry has become widespread in recent years, mainly due to their exceptional engineering properties, weight and cost benefits, alongside the

promotion of environmental sustainability.[84-85] In this regard, the environmental impact of traditional and advanced composites in the marine sector has caused considerable concern. In response, regulatory bodies have introduced stricter guidelines for manufacturing and maintenance practices, prompting manufacturers to explore new materials and processes.[85] To meet the demands of creating high-performance engineering components while prioritizing sustainability, incorporating biodegradable polymer matrix composites has become increasingly necessary. These composites facilitate material recycling, reduce the presence of toxic and hazardous substances, and minimize waste and air pollution. They also offer exceptional mechanical properties, making them a desirable choice for the marine sector.

Regardless of the application field, combining nanotechnology and polymer-based materials has been recognized to develop highly advanced and dynamic materials. Through the exclusive use of nanotechnology in manufacturing, these advanced composites will have enhanced properties necessary for optimal performance.

CHAPTER 4

4. MATERIALS AND METHODS:

4.1. MATERIALS FOR ZnO SYNTHESIS:

Zinc acetate dihydrate Molecular Weight 183.48 (Sigma-Aldrich), Zinc Chloride Molecular Weight 136.30 (Sigma-Aldrich) Zinc Nitrate hexahydrate Molecular Weigh 297.49(Sigma-Aldrich), Sodium hydroxide Molecular Weight 40 (Sigma-Aldrich)

A standardized glycerol-based cryopreserved *S. cerevisiae* pure culture (DSM 1333), purchased from the German collection of microorganisms and cell cultures (DSMZ, Germany, Braunschweig), served as the source for microbial-mediated NP production. The yeast was cultured on YPD (Carl Roth, Germany) agar plates containing 1.7% Agar-Agar (Carl Roth, Germany) at 30 °C for 72 h with subsequent storage at 4 °C.

4.2. MATERIALS FOR COPOLYMER SYNTHESIS:

Poly(dimethylsiloxane), bis(3-aminopropyl) terminated average Mn ~2,500, (Sigma-Aldrich) Dopamine hydrochloride, (Sigma-Aldrich) Isophorone diisocyanate 98%, (Sigma-Aldrich) Dichloromethane ACS reagent ≥99.5%, (Sigma-Aldrich) Diethyl ether, (Sigma-Aldrich) N,N-Dimethylformamide ACS reagent, ≥99.8% 319937-1L(Sigma-Aldrich).

4.3. CHEMICAL SYNTHESIS OF ZnO

The synthesis of ZnO nanomaterial was achieved using zinc acetate, zinc chloride, and zinc nitrate as zinc sources, along with sodium hydroxide (NaOH) as the hydrolysing agent. Initially, each zinc source was dissolved in 75 ml of distilled water. Subsequently, 150 mL of a 0.1 M NaOH solution was slowly added to the zinc solution while vigorously stirring. Then, the resulting solution was exposed to red, blue, or white light for 1 hour. As a control, a synthesis was also conducted under dark conditions, covering the samples with aluminium foil (Fig. 20).

Figure 20. Photographic representation of the chemical synthesis of ZnO with blue light (left), red light (center), and white light (left) in the incubator including an adapted LED system.

After filtration, the white precipitates underwent multiple rinses using distilled water, approximately 4-5 times. They were then subjected to controlled drying in an oven set at 60°C for 24 hours. To expedite the drying process, the precipitates were further exposed to a high temperature of 200°C for 2 hours within the confines of an oven. To ensure accuracy and consistency, the experiments were conducted in triplicate, aiming to ascertain the reproducibility of the obtained results. Table 1 shows the specific quantities of each precursor used in the synthesis of ZnO for chemical products.

Table 1. Quantity of each zinc salt used in the synthesis of ZnO for chemicals.

	quantities of precursor (g)
Zinc Nitrate hexahydrate	2.28
Zinc acetate dihydrate	1.68
Zinc Chloride	1.03

4.4. BIOLOGICAL SYNTHESIS OF ZnO

To create the ZnO nanomaterial, various zinc sources including zinc acetate, zinc chloride, and zinc nitrate were employed, while sodium hydroxide (NaOH) was used as the hydrolysis agent. The procedure involved combining each zinc source with an aqueous yeast solution (*Saccharomyces cerevisiae*), which was then stirred and exposed to white light irradiation for 1 hour. Subsequently, 1 ml of 1.4 M NaOH was slowly added dropwise to the solution. The solution was again irradiated with white light, this time for a total of 24 hours (Figure 21). In addition to the irradiated samples, a synthesis was conducted under the same standard procedure described above but in darkness.

Figure 21. Photography of the apparatus for biological synthesis of ZnO with light in the incubator including an adapted LED system.

Alongside irradiated and non-irradiated samples, a control synthesis was conducted without the addition of yeast. Once white precipitates were obtained, they were centrifuged at a speed of 3800 rotations for 15 minutes. A thorough washing with distilled water was then performed, repeating the process 4-5 times, and finally filtered. The resulting precipitates were dried in an oven at 60°C for 24 hours. To expedite the drying process, the precipitates were subjected to a temperature of 200°C for 2 hours. To ensure accuracy and consistency, the experiments were conducted in triplicate, aiming to ascertain the reproducibility of the obtained results. Table 2 shows the specific quantities of each precursor used in the synthesis of ZnO for biological products.

Tabel 2. mL of each zinc salt solution and yeast solution (CFE) used in the biological synthesis of ZnO.

	quantities of precursor (mL)	yeast solution (CFE) (mL)
Zinc Nitrate hexahydrate (3.2M)	0.2	19.8
Zinc acetate dihydrate (1.6M)	0.4	19.6
Zinc Chloride (3.2M)	0.2	19.8

4.5. PREPARATION OF YEAST SOLUTION AND IRRADIATION SYSTEM.

The Department of Biotechnology and Food Engineering, MCI - The Entrepreneurial School, Maximilianstrasse 2, 6020 Innsbruck, Austria, holds the rights to the yeast synthesis methodology and irradiation equipment used in this study which I conducted for 6 months abroad for my doctoral research.

For yeast cultivation and biomass production under aerobic conditions, approximately 1 mm^3 of a single yeast colony was transferred from an agar plate into a 50 mL YPD medium in a 100 mL Erlenmeyer flask. The culture was incubated at 30 °C and 150 rpm in the dark for 24 h. For the following experiments in triplicates and controls, 1 mL from the previous culture was used to prepare 24 h yeast cultures in 50 mL YPD medium under the same cultivation conditions as before. After 24 24-hour cultivation period, the yeast cultures reached the late stationary growth phase. The yeast suspensions were adjusted to a cell density of OD_600=5, which corresponds to an average total cell count of $2.93 \cdot 10^{14}$ mL^{-1} as determined by counting in a Thoma chamber. Yeast biomass was recovered by centrifugation at 4 °C and 5,440 g for 15 min (Rotanta 460 R, Andreas Hettich GmbH & Co.KG, Germany). The obtained cell pellets were washed thrice with 20 mL ultrapure water with repeated resuspension and centrifugation to remove any remaining medium components.

To generate CFEs, the washed yeast biomass was resuspended in 50 mL of ultrapure water and extracted at 30 °C by shaking at 150 rpm (Minitron, Infors AG, Switzerland) under dark conditions for 72 h. The leached yeast cells were separated at 4 °C and 5,440 g for 15 min, and the supernatant, i.e. the obtained CFE, was filtered through a 0.22 µm membrane (Rotilabo®-syringe filters, PVDF, Carl Roth GmbH + Co. KG, Germany).[86]

To perform standardized light experiments, an irradiation apparatus specially adapted to the incubators used (Minitron, Infors AG, Switzerland) was designed (Figure 22). Illumination of the incubation chamber with a rotation area of 40cm×40cm was provided by a total of nine side- and rear-centred light elements, each composed of seven LEDs emitting white light with a correlated colour temperature of 3100 K (LUXEON Line 3535L, warm white, Lumileds Holding, USA). The desired irradiance was controlled via an app (Casambi, planlicht®). Visible light irradiance was determined at 555 nm by a PM100D radiometer equipped with an S120 VC photodiode power sensor (Thorlabs Inc., Newton, New Jersey, USA).

Irradiation of the reaction mixtures with white light blue light or red light during the NP synthesis step was carried out with an average irradiance of 1.0 ± 0.2 mW cm^{-2} (intensity 100%).[87]

Figure 22. Setup of white light irradiation experiments in the incubator including an adapted LED system [86]

4.6. COPOLYMER SYNTHESIS.

The synthesis process consisted of dissolving 4.25 mL of PDMS and 0.07 g of DOPA in 11.6 mL of dichloromethane and 2.5 mL of dimethylformamide.

After purging the PDMS-dichloromethane and DOPA-dimethylformamide solutions with argon for 10 minutes, they were combined in a 50 mL flask equipped with a magnetic stirrer. A solution containing 0.404 g of IPDI dissolved in 2.5 mL of dimethylformamide was then slowly added drop by drop to the reaction flask while stirring at a speed of 500 rpm and maintaining a temperature below 0 °C. Throughout the reaction, argon was continuously used to protect and maintain the atmosphere below 0°C for a total of 4 hours. When the reaction was complete, the reaction system was cooled to room temperature, and the dichloromethane was removed by vacuum-assisted rotary evaporation. To remove any traces of solvent, the product was subjected to three cycles of ultrasonic washing with deionized water. The resulting aqueous solution was then subjected to liquid-liquid extraction using ethyl ether as the extraction solvent. This extraction procedure was repeated three times. The solution containing the product was then further clarified by the addition of solid anhydrous sodium sulphate and then filtered to remove any remaining impurities. The ethyl ether was removed together with the product by rotary evaporation. Finally, the collected product was dried in a vacuum oven at room temperature for two days until it became a light-yellow sticky substance.

4.7. COMPOSITE PREPARATION

To create a composite of ZnO-copolymer, ZnO nanopowders were dispersed in a solution of copolymer and ethyl acetate. The mixture was vortexed for 30 minutes until a concentration of 5% and 10% w/v was reached. Before deposition, 7 × 25 mm glass microscope substrates were prepared by rinsing them with acetone and EtOH to remove any organic impurities and ensure a consistent coating.

To obtain a final volume of 0.4 mL, the resulting sol from the previous steps was thermally incubated at 80°C for 1 hour, during which time the EtOAc was gradually evaporated. The resulting mixture was then drop-cast onto glass and kept at 80°C until completely dry (Figure 23).

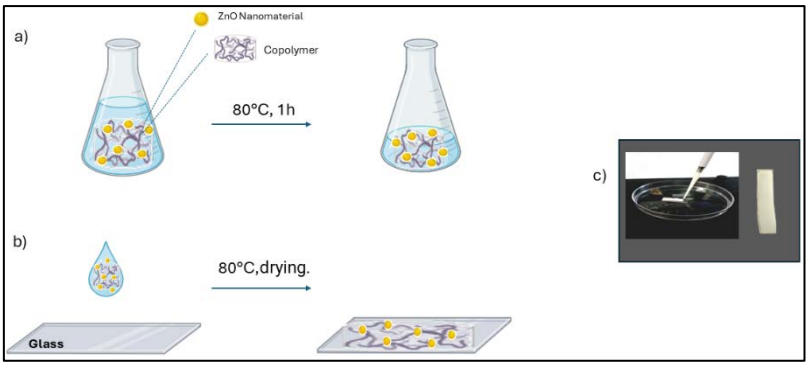

Figure 23. (a) The mixture containing the copolymer and ZnO is heated to 80 °C for 1 hour, allowing partial removal of EtOAc. (b) While still at 80 °C, the nanomaterial/polymer blend is drop-cast onto a glass slide to produce a thick coating until the EtOAc is completely removed by drying the composite film at 80 °C.(c)Photograph of the casting on a glass slide and the resulting system at a concentration of 10% w/v of the ZnO nanomaterial.

4.8. CHARACTERISATION TECHNIQUES

In this thesis, nanostructured zinc oxide was obtained by a precipitation method from different zinc sources and a silicone copolymer comprising PDMS backbones, ureido units, and terminal catechol motifs.

The use of several techniques to characterise the synthesized ZnO powders and copolymer allowed us to obtain detailed information on

1. crystallite and nanomaterial dimensions

2. crystalline phases present.

3. microstructure and morphology.

4. chemical composition.

UV-visible spectroscopy (UV-Visible) allows us to analyse the optical properties of synthesized nanomaterials.

X-ray diffraction (XRD) was used to identify the crystalline phase of zinc oxide. The Scherrer equation was used to estimate the average size of the crystallites making up the powders. In addition, scanning electron microscopy (SEM) provided valuable information on the morphology and shape of the aggregates present in the powders. Furthermore, through the analysis of Attenuated Total Reflection Fourier Transform Infrared Spectroscopy (ATR-FTIR), we successfully identified the presence of both organic and inorganic species by detecting specific functional groups present in the molecules, as evidenced by the formation of distinct signals.

X-ray photoelectron spectroscopy (XPS) was used to determine the elemental chemical state and provide compositional information.

Meanwhile, magnetic resonance spectroscopy (NMR) has provided detailed information on the molecular structure of the copolymer.

4.8.1. Ultraviolet-visible Spectroscopy

To analyse the absorption spectrum of the synthesized nanomaterial, a small amount of each sample was dispersed in isopropanol and placed in a cuvette that allows optical transparency.

Spectra were acquired using a UV–visible spectrophotometer (Specord S600), in the range 200–800 nm, with a wavelength accuracy of ±0.3 nm (reported by the producer).

4.8.2. X-Ray Diffraction Analysis

This technique is based on the phenomenon of coherent scattering, in which X-rays interact with uniformly distributed scattering centres in a pattern similar to that of a crystalline material. These scattering centres are spaced at distances comparable to the wavelength (λ) of the radiation used. (Figure 24).

Bragg's Law (1) is used to explain the phenomenon of constructive interference that occurs when X-rays are scattered from the atomic planes of a crystal.

$$2d_{hkl}\sin\vartheta = n\lambda \qquad (1)$$

n = diffraction order;

λ = wavelength of the incident radiation;

dhkl = interplanar distance between two lattice planes with Miller indices (hkl);

ϑ = angle of incidence formed by the X-ray direction and the family of planes

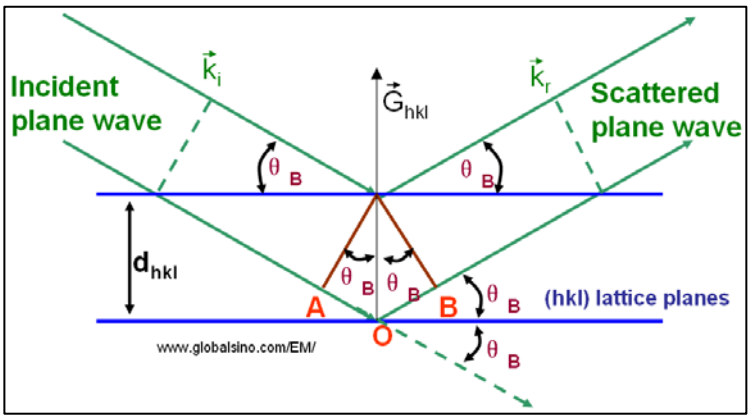

Figure 24. Geometric representation of Bragg's law.

It is important to note that X-ray diffraction is not a surface analysis technique, but rather a method that provides information about the internal structure of materials. The beam entering and leaving the sample is made up of photons, resulting in significant penetration and escape capabilities, known as high penetration depth and high escape depth respectively. In contrast, the impact on the sample is

minimal. A typical diffraction spectrum consists of a sequence of distinct reflections. The intensity, amplitude, and position of each are unique, with the position represented as 2ϑ, which combines the angle of incidence and the collection angle formed by the beam as it interacts with the sample surface. By analysing the reflections, both in terms of position and intensity, and comparing them with reference spectra, it is possible to accurately determine the composition of the material, identify its different crystalline phases, and even determine its preferred orientation, if any.

Scherrer's formula is used to estimate the average size of crystallites. The formula (2) generally applies to the most intense reflection. However, in some diffraction spectra, other reflections of comparable intensity fall near the main reflection and are difficult to resolve. In these cases, it is necessary to introduce into the Scherrer equation the data for a sufficiently intense reflection that can be traced with certainty to a single phase.

$$D = K \frac{\lambda}{\Delta\omega \cos\theta} \qquad (2)$$

D = average diameter of the crystallites;

K = factor dependent on the shape of the particles (equal to one for spherical crystallites);

λ = wavelength of the incident radiation;

Δω = width at half peak height (FWHM, Full Width at Half Maximum);

θ = (2θ)max⁄2, where (2θ)max is the position of the peak.

X-ray diffraction (XRD) patterns of the powder were recorded with a Bruker diffractometer in Bragg-Brentano geometry, using Cu Kα-filtered Ni radiation (λ = 1.54056 Å) and a graphite monochromator in the diffracted beam. The X-ray generator operated at a power of 40 kV and 30 mA; the instrument resolution (divergent slits and 0.5° antiscatter) was determined using standards free of the effect of reduced crystal size and lattice defects. Diffraction patterns were analysed using the MAUD software. In particular, an acquisition range of 20° to 80° was adopted for zinc oxide, with a step width of 0.5°.

4.8.3. Scanning electron Microscopy

The use of electrons to interact with the surface under examination forms the basis of scanning electron microscopy (SEM), an advanced technique in electron microscopy. This technique allows a wide range of magnifications, from 10 to 0.003 microns. The electric field between the anode and cathode is used to accelerate the electron beam, which is then focused precisely on the surface of the solid being examined.

Electron beam generation can be achieved by two methods: thermionic emission from a tungsten or lanthanum hexaboride filament, or using the "field effect", in which a tungsten tip, pure or coated with zirconium oxide, emits electrons by the tunnel effect when a strong electric field is applied. The resulting beam is then focused and narrowed by an array of magnetic lenses. The ferromagnetic material used consists of symmetrical cylindrical coils, each with a perforated hole. These coils serve to focus the lines of force within the magnetic field as the electrons are deflected by the Lorentz force. When in contact with the sample, the electron beam has sufficient energy to induce different phenomena depending on both the properties of the material and the energy of the electrons themselves.

There are two main types of electron scattering: elastic scattering, also known as reflection, and inelastic scattering. In elastic scattering, the electrons undergo minimal changes in momentum as they collide with atoms in the sample. Inelastic diffusion, on the other hand, occurs when electrons lose energy during collisions, leading to various phenomena such as the emission of secondary electrons, Auger electrons, and photons.

The electronics in the analyser collect the electrons according to the type of event from which they originate and ultimately form the image. When the electrons interact with atoms in the sample, they change scattering direction and backscatter. The result is a beam with an intensity and energy distribution corresponding to the number and type of atoms involved in the interaction. As a result, the backscattered electrons provide valuable information about the composition of the sample.

In contrast, secondary electrons are produced when primary electrons enter the sample and collide with the valence electrons of the sample atoms, producing secondary electrons. During their trajectory, the backscattered electrons encounter multiple deflections induced by the atoms, resulting in sufficient energy to displace the electrons from their orbitals before exiting the surface and producing secondary electrons. When investigating surface morphology, secondary electrons are typically observed due to their low energy and originate exclusively from the surface layers. The emission yield of these electrons depends on the orientation of the specific area concerning the incident beam. Figure 25 shows the diagram of an SEM microscope:[88]

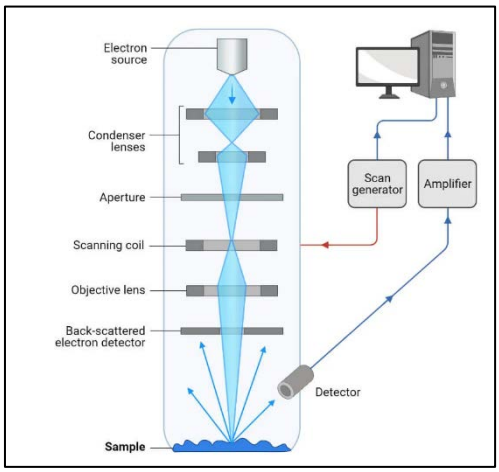

Figure 25. Diagram of an SEM microscope.[88]

The morphology of the samples was analysed by SEM using an ESEM Quanta 200 instrument (FEI, Hillsboro, OR, USA). The samples were attached to an aluminium hub using carbon adhesive tape. SEM micrographs were taken in secondary electron imaging mode using an accelerating voltage of 20.0 kV, spot size 3.5 at a working distance of approximately 10 mm.

4.8.4. Attenuated total reflectance-FTIR.

In recent years, the Attenuated Total Reflectance (ATR) technique has revolutionized the analysis of solid samples by eliminating the major sources of error resulting from complex and inconsistent preparation methods. Achieving uniform matrix ratios throughout the sample and ensuring the stability of some of the compounds used in the preparations were additional challenges. However, the ATR technique reduces or eliminates all these error-causing factors, providing more accurate and reliable results.

Total internal reflection is a phenomenon that occurs when a beam of light passes from an optically denser medium to an optically less dense medium. At a certain angle of incidence, known as the critical angle, light undergoes total internal reflection. This can be seen in Figure 26, where the critical angle is represented by the D ray.

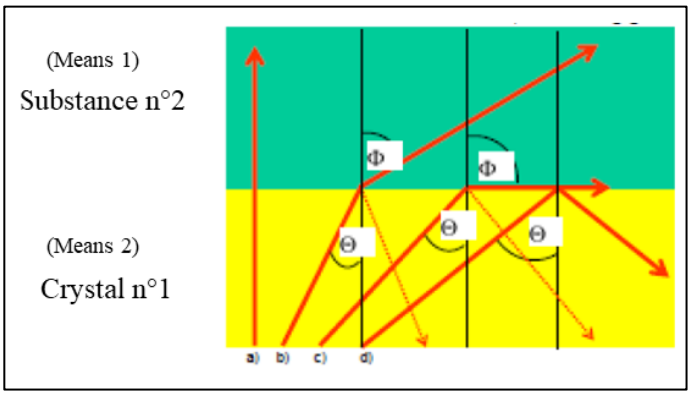

Figure 26. Graphic representation of the phenomenon that occurs when a beam of light passes from an optically denser medium to one that is optically less dense.[91]

A phenomenon known as an evanescent wave occurs when an electromagnetic wave is present in a region of a medium with a lower index of refraction. This wave, which exists for only a fraction of its wavelength, can penetrate the medium. As it passes through the sample, the evanescent wave gradually decreases in intensity, decaying exponentially at a distance of a few microns from the crystal surface. The penetration capability of the evanescent wave is determined by the distance from the sample/crystal interface, the point at which the intensity of the wave decreases to 37% of its original value.

The evanescent wave has several characteristics that distinguish it. First, unlike transverse waves, the evanescent field includes vector components in all spatial directions, giving it a truly unique nature with far-reaching implications (Figure 27).

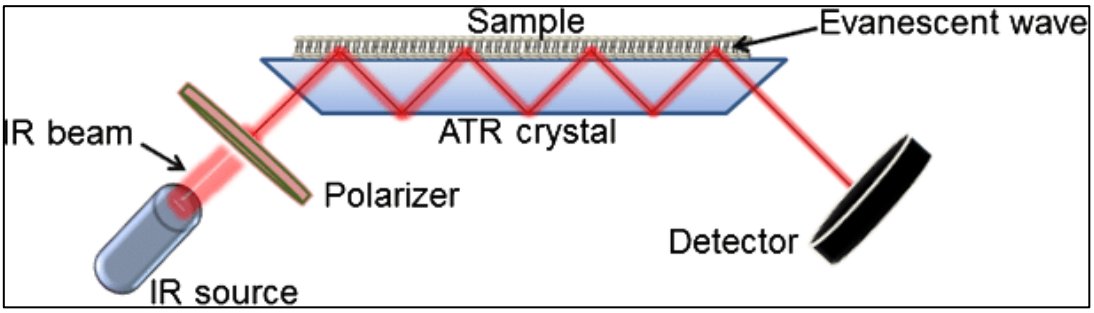

Figure 27. Schematic representation of ATR-FTIR system

Secondly, the intensity of the field decreases with increasing distance from the normal to the surface of the medium, so that it is only present near the surface. ATR-IR spectroscopy is a valuable tool for analysing material surfaces and characterizing thick or highly absorbent substances that can be studied by transmission IR spectroscopy. When dealing with solid materials or thick films, no sample

preparation is required for ATR analysis. In ATR-IR spectroscopy, infrared radiation passes through a transparent IR crystal with a high refractive index, which allows multiple internal reflections.

To initiate the technique, the sample surface is applied to the top surface of a ZnSe or Ge crystal. Once in place, the infrared radiation emitted by the spectrometer enters the crystal and is reflected within it. This process allows the radiation to penetrate the sample by a certain amount at each reflection, known as an evanescent wave. After several reflections, the intensity of the wave is recorded as it leaves the crystal, traveling in the opposite direction to the incident beam. This intensity is then analysed. Certain conditions must be met for the technique to give positive results.

Specifically, the sample must be in direct contact with the crystal, allowing the evanescent wave to extend beyond the crystal for 0.5 μm.

To ensure effective results, the crystals must have a refractive index significantly higher than that of the sample, as most solids and liquids typically have a lower refractive index. Diamond, known for its exceptional durability, chemical inertness, and minimal background noise, is the preferred crystal choice.[88-91]

ATR-FTIR spectra were collected by using an FTIR Bruker Vertex Advanced Research Fourier Transform Infrared spectrometer (Bruker, Billerica, MA, USA) equipped with a Platinum ATR and a diamond crystal, in the 70–4000 cm^{-1} range (lateral resolution of 2 cm^{-1} and 200 scans). A baseline correction of the scattering was performed using OPUS 7.5 software.

4.8.5. X-Ray photoelectron spectroscopy

X-ray photoelectron spectroscopy (XPS), also known as ESCA (electron spectroscopy for chemical analysis), is a method of analysing photoelectrons emitted after the sample has been irradiated with an energy equal to their binding energy. At the heart of XPS analysis is the photoelectric effect (Figure 28).

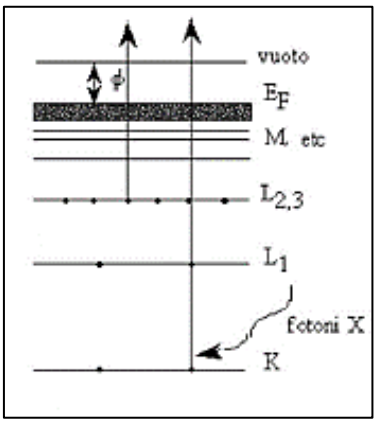

Figure 28. Diagram of the photoemission phenomenon.

This phenomenon occurs when a system is exposed to radiation with electromagnetic energy of specific energy hν. In this scenario, there is a finite probability that a photon will be absorbed, causing an electron to move to an unoccupied level, or that the electron will be emitted as a photoelectron. The energy balance of this process, adjusted for the work function of the solid ϕS, is described by Einstein's relation.

The equation (3):

$$hv = BE + KE + \varphi_s \quad (3)$$

$d$escribes the relationship between the frequency of the incident radiation (ν), the binding energy of the electron (BE), the kinetic energy of the photoelectron (KE), and the work function (ϕ_S). The binding energy is defined concerning the vacuum level, while the kinetic energy depends on the level from which the electron was emitted. By knowing the frequency of the incident radiation and measuring the kinetic energy of the emitted electrons, it is possible to calculate the binding energy of the photoemitted electron.

For photoemission to occur, the incident radiation must have an energy (hν) greater than the binding energy. This condition is crucial because it triggers the release of electrons from different shells and atoms, resulting in the generation of an electron beam of different energies. When X-ray radiation induces photoemission, it creates vacancies in the central energy levels. These vacancies are then

filled by electrons from the outer energy levels. The process of recombination of electron-lacuna pairs can take place either in radiative media, resulting in the emission of X photons (known as X fluorescence), or in non-radiative media, where an Auger electron is emitted from the outer shells (known as Auger recombination).

The photoemitted electrons originate from the outermost layers of the material due to the limited penetration depth of X-rays. Therefore, XPS is a very surface-sensitive technique as it detects electrons mainly near the surface. The thickness of the material analysed is related to the kinetic energy of the photoelectron, which determines its mean free path, Λe.

In XPS (KE > 50 eV) the relationship between Λe and kinetic energy is best represented by the analytical curve (4):

$$\Lambda_e(KE) \propto (KE)\text{^}0.52 \qquad (4)$$

In particular, the distinctive peaks of the photoelectrons correspond to specific binding energy (BE) values for each atom, allowing a qualitative determination of the elements present in the sample.

In addition, the position of the peaks of an element may vary slightly, typically by a few electron volts, depending on the chemical environment or oxidation state of the element. These effects can be due to photoelectronic emission. The binding energy of photoelectronic peaks can vary significantly due to surface conditions. To ensure accurate calculations, a known reference value is selected. To achieve calibration, it is common practice to use the C1 carbon peak as a reference point for surface contamination (284.6 eV). In experimental settings, surface loading can be minimized or eliminated. By using a flood gun, also known as a neutralizer, the surface is exposed to low-energy thermionically generated electrons. Photoelectron spectroscopy not only provides qualitative analysis but also allows further exploration and investigation. Semi-quantitative analysis of the species on the surface is also part of the task.

To obtain quantitative data we use a simplified correlation between peak area and the relative concentration of atoms in an element (5).

$$C_i = 100\frac{A_i}{S_i}\left(\sum_j \frac{A_j}{S_j}\right)^{-1} \qquad (5)$$

An XPS spectrometer consists of several components, including an X-ray source, an ultra-high vacuum photoionization chamber, an electron analyser, an electron counter, and a data acquisition and display processor. The electron analyser uses concentric hemispherical areas (CHA) within an

electrostatic analyser to distinguish electrons based on their kinetic energies as they emerge from the sample surface. Working under UHV (Ultra High Vacuum < 10-7 Pa) conditions is essential for two reasons: firstly, to minimize the number of impacts experienced by the electrons on their way to the analyser.

In addition, due to the high sensitivity of XPS to surface conditions, it is critical to minimize contamination of the sample surface by residual species that may be present in the analytical environment.[92]

The surface chemical composition of the coatings was investigated by XPS using a ULVAC-PHI 5000 Versa Probe II scanning XPS microprobe, an Al Kα source (1486.6 eV), a 128-channel hemispherical analyser, and FAT mode.

4.8.6. Nuclear Magnetic Resonance

The chemical structure of materials can be determined using nuclear magnetic resonance, a technique widely used in scientific research.

We can use the principle that the nuclei of some elements align with an intense, stationary external magnetic field. This phenomenon is only observed in atoms with a non-integer spin, as their spinning nuclei generate a μ magnetic field, making them resemble miniature magnets. This similarity is because the nuclei, which consist of electrical charges, can be compared to circuits driven by current. The atoms commonly used for this purpose are 1H and 13C, both with spin 1/2. Like a compass needle, a spin nucleus will rotate when placed in a magnetic field. This motion is caused by a pair of forces that align the nucleus with the external field. In the case of a nucleus with spin 1/2, there are two possible orientations: one parallel to the field, resulting in low energy, and one antiparallel, resulting in high energy (Figure 29).

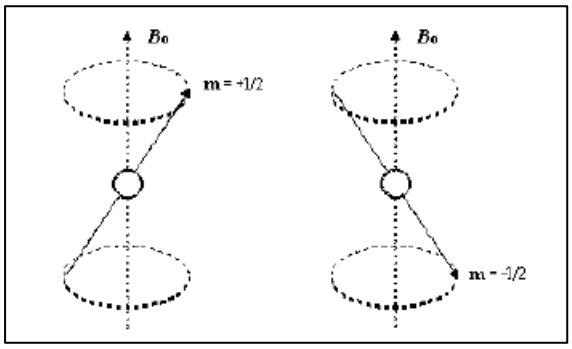

Figure 29. Possible orientations of the nuclei in the presence of a magnetic field.

The transition of a nucleus from one potential orientation to the other can be achieved by absorbing (or emitting) a certain amount of energy, given by (6):

$$E = h\upsilon = 2\mu B \qquad (6)$$

In this equation, h is Planck's constant, and υ is the frequency of the absorbed electromagnetic radiation.

In the spectrum, the NMR signal of a particular nucleus undergoes a shift towards higher or lower frequencies, depending on its chemical environment.

This phenomenon is because electrons, as charged particles, move when subjected to a magnetic field (B_0). As a result, they generate a secondary magnetic field that opposes the applied field, resulting in a shielding of the nucleus (as shown in Figure 30).

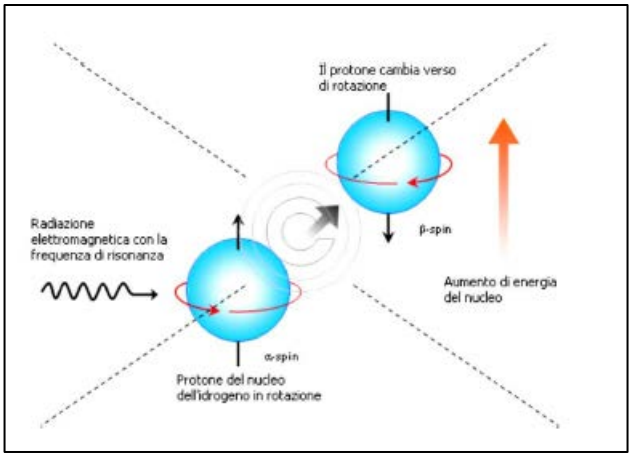

Figure 30. Operating principle of NMR.

The magnitude of the shielding is directly proportional to the electron density, which means that nuclei in an electron-rich environment will experience a reduced magnetic field. Consequently, these nuclei will undergo transitions at lower frequencies than nuclei located in electron-deficient environments.

The chemical shift, which refers to the change in the NMR signal of a particular nucleus, occurs when protons or carbons near electronegative atoms become sheathed. This exposes them to a stronger magnetic field, causing them to move to higher frequencies, resulting in a greater chemical shift in the spectrum. The absolute chemical shift is directly proportional to the strength of the applied field, which means that different instruments will produce different absolute chemical shifts depending on the strength of their magnetic fields.

To solve this problem, it is most advantageous to use the relative chemical shift, denoted δ, as defined by the following equation (7):

$$\delta(ppm) = \frac{\nu r - \nu}{\nu r} * 10^6 \qquad (7)$$

Although it is possible to analyse the nucleus of ^{13}C, the limited abundance of this isotope in nature (only 0.11% compared to ^{12}C) means that only a small number of carbon atoms would line up, resulting in a reduced signal-to-noise ratio.

Different peaks in a 1H NMR spectrum represent hydrogen atoms in different environments or chemical lattices. By looking at the relative area under each peak (since absolute values can vary with solution concentration), we can determine the relationship between the different types of hydrogen atoms present. The area of a peak depends solely on the abundance of the hydrogen atom within the molecule, regardless of its structural attachment. To obtain comparable values, the area of each peak is divided by the number of corresponding hydrogens, which is perfectly aligned with the values given by the chemical formula of the polymer being analyzed.[93]

4.8.7. Photocatalytic activity

To evaluate the photocatalytic performance of the ZnO samples, the degradation of methylene blue (shown in Figure 31) adsorbed on these surfaces was studied. Methylene blue was chosen as a representative pollutant because of its coloured nature, which makes it easy to detect by spectrophotometry. This organic dye naturally loses its colour after prolonged exposure to ultraviolet light, a process that can be enhanced by the presence of substances such as ZnO on the surface on which it is deposited.

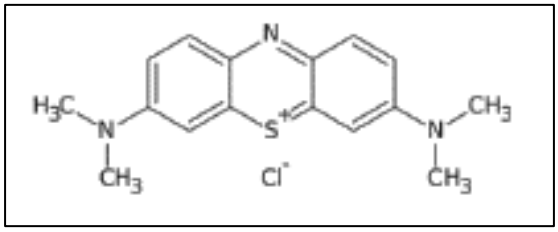

Figure 31. Methylene blue molecule structure.

The mechanism of degradation of organic molecules by zinc oxide follows the same principle as the well-known photodegradation process of titanium dioxide: when ultraviolet light hits the surface of the oxide, it excites electrons from the valence band to the conduction band.

This results in the formation of electron-lacuna pairs (e-, h+). These pairs, if they remain separated, can interact with molecules adsorbed on the surface (see Figure 3.14).

If an electron-donating molecule (D) is present on the surface of the material, it can react with the vacancy to produce an oxidized species (D+) (reaction (1)). Similarly, if an electron-accepting species (A) such as oxygen or hydrogen peroxide is present on the surface, it can react with the electrons in the conduction band to form a reduced species (A-) (reaction (2)).

$D + h^{+} \longrightarrow D^{\cdot +}$ (1)

$A + e^{-} \longrightarrow A^{\cdot -}$ (2)

Semiconducting metal oxides are known for the strong oxidizing power of their vacancies (h+), which can react with water adsorbed on their surface. This leads to the formation of a highly reactive hydroxyl radical (-OH).

Both holes and hydroxyl radicals have strong oxidizing properties, making them effective in reducing a wide range of organic pollutants. [94]

The photocatalytic activity of the zinc oxide nanomaterials (10% w/v) and the ZnO/copolymer coating was evaluated in terms of MB photodegradation in 20 mL, 25 μM aqueous solution). Irradiation was carried out using a solar simulator (ABET Solar Simulator Model 10500) at 1 sun. The distance between the sample and the solar simulator was set using a calibration cell through a tester (1 sun corresponded to 100 mV). Before light irradiation, the coatings were soaked into the MB solution and kept in the dark for 1 h to allow adsorption–desorption equilibrium. Irradiation effects were evaluated at 30-minute intervals by analysing changes in the absorption spectra of the MB solution. Spectra were acquired using a UV–visible spectrophotometer (Specord S600), in the range 200–800 nm, with a wavelength accuracy of ±0.3 nm (reported by the producer). Intensity measurements at 664 nm were used to quantify spectral changes.

CHAPTER 5

5. Results and discussion

5.1. CHEMICAL SYNTHESIS.

The photochemical synthesis of metallic oxide nanoparticles traces back to the 18th century when Schulze discovered that certain silver salts darken when exposed to light.[95] Recent advances in metallic NP research have extended this classic concept of photoreaction to reveal a new application as a synthesis method for nanostructures integrated into light-emitting diodes (LEDs).[96] LEDs have unique characteristics such as narrow band, low divergence angle, and high emission intensity, making them ideal as light sources to excite specific sizes and shapes of metallic NPs in photochemical reactions.[97] This process has several advantages, such as the versatile and environmentally friendly method of photoinduced treatment, easy control of the in-situ generation of reducing agents, and the initiation of nanoparticle formation through photoirradiation. Recent advances in photochemistry and photo-processing techniques have provided researchers with various synthetic approaches to obtain metal nanoparticles under different conditions. The specific size and shape of the nanoparticles are determined by the synthetic conditions, making them crucial in the formulation process.[98]

Radiation-induced processes in solids have attracted much attention, not only for their ability to degrade the properties of materials but also for their potential to enhance or modify these properties.[99] There is extensive documentation of the deleterious effects of radiation on solids and surfaces, including the formation of defects and sputtering caused by cascades of collisions initiated by chain processes.[100]

This thesis aimed to synthesize ZnO nanoparticles by photoinduction using LEDs emitting at different wavelengths and using different precursors. LEDs of different colours have different photon fluxes and deposit different amounts of energy, which can affect the size, surface morphology, and other physicochemical properties of the synthesized nanoparticles. Figure 32 provides a visual representation of the photoinduction mechanism, illustrating the relative wavelengths associated with the three LEDs used in the study.

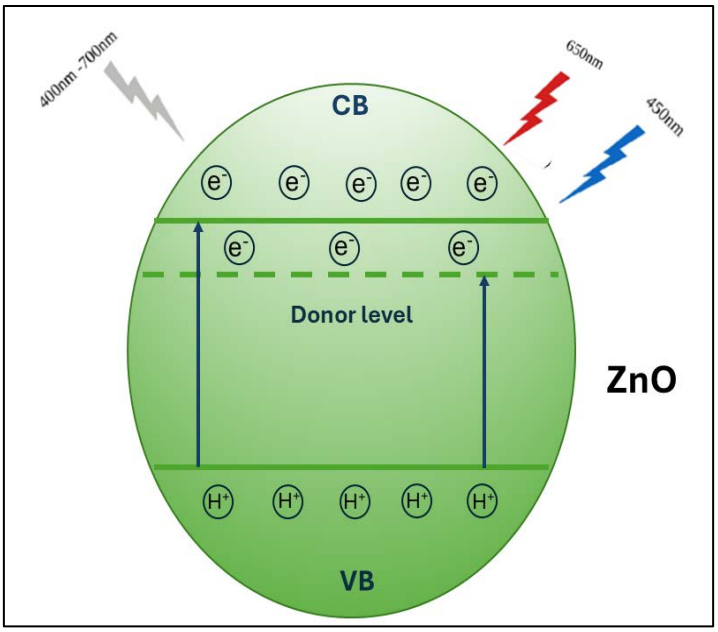

Figure 32. Mechanism of photoinduced ZnO NPs synthesized under different light conditions.

By subjecting the precursors of zinc salts to both irradiated and non-irradiated conditions, it was possible to obtain zinc hydroxide by precipitation, which was recovered by filtration and subjected to heat treatment to obtain ZnO. The latter was then dried and characterized.

To simplify the growth process of zinc oxide in NaOH, we consider the acetate salt reaction as an example:

$$Zn\,(CH_3COO)_2 \cdot 2\,H_2O + NaOH \longrightarrow Zn\,(OH)_2 + 2CH_3COO\,Na + 2H_2O$$

$$Zn\,(OH)_2 + 2H_2O \longrightarrow Zn\,(OH)_4^{2+} + 2H^+$$

$$Zn\,(OH)_4^{2+} \longrightarrow ZnO + H_2O + 2OH^-$$

The synthesis steps are those discussed in detail in the Materials and Methods, section 4.3.

From here onwards, the LED lights will be identified as WL for white light, RL for red light, and BL for blue light, while the term control indicates the absence of irradiation. The samples are identified as ZnO (nitrate), ZnO (acetate), and ZnO (chloride), considering the precursors used in the synthesis, which are indicated in brackets.

The synthesized ZnO nanoparticles were subjected to X-ray diffraction (XRD) analysis. High Score Plus software was used to analyse the XRD spectrum, and 2θ values were used to calculate lattice parameters.

The XRD pattern showed that the nanoparticles belong to space group 186: $P6_3mc$ (ICDD reference number 96-901-1663). The XRD patterns of ZnO nanoparticles synthesized with irradiation of the different precursors and the respective controls (without irradiation) are shown in Figure 33.

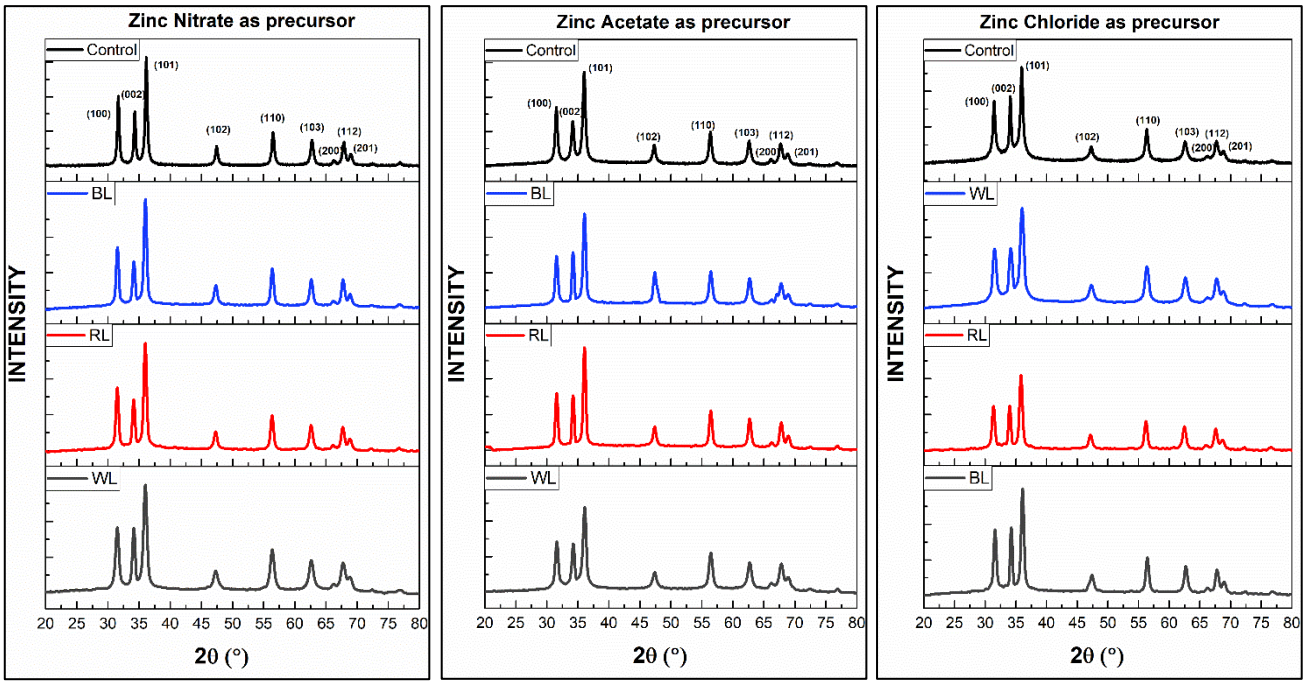

Figure 33. X-ray diffraction (XRD) spectra of ZnO: left XRD spectrum of ZnO synthesized with the precursor zinc nitrate, middle XRD spectrum of ZnO synthesized with the precursor zinc acetate and right XRD spectrum of ZnO synthesized with the precursor zinc chloride with and without irradiation.

Analysis of the spectra showed that no new peaks were detected after exposure to light, suggesting that the latter did not cause crystalline phases to appear or disappear. The average crystallite size, dislocation density, and lattice strain for ZnO synthesized using different precursors and LEDs are presented in Table 3.

Table 3. average crystallite size (D), dislocation density(δ), lattice strain (ε) before and after irradiation with LED lights for samples synthesized with zinc nitrate, zinc acetate, and zinc chloride.

Sample	**ZnO (Zinc nitrate as a precursor)**			**ZnO (Zinc acetate as a precursor)**		
hkl (101)	D(nm)	δ ($10^{-4}nm^{-2}$)	ε (10^{-4})	D(nm)	δ ($10^{-4}nm^{-2}$)	ε (10^{-4})
control	28.3111	12.4763	12.2438	24.2569	16.9953	14.2902
WL	18.8643	28.1007	18.3752	21.2317	22.1835	16.3263
BL	24.2554	16.9973	14.2910	33.9617	8.6700	10.2066
RL	24.2530	17.0007	14.2924	24.2591	16.99221	14.2888
Sample	**ZnO (Zinc chloride as a precursor)**					
hkl (101)	D(nm)	δ ($10^{-4}nm^{-2}$)	ε (10^{-4})			
control	28.2943	12.4912	12.2511			
WL	15.4330	41.9853	22.4606			
BL	24.2613	16.9892	14.2876			
RL	24.2418	17.0165	14.2990			

Using Scherrer's equation (eq. 8),[101] the average crystallite size of ZnO, denoted by D was determined.

$$D = \frac{0.9\lambda}{\beta \cos(\theta)} \qquad (8)$$

D values for ZnO (nitrate), ZnO (acetate), and ZnO (chloride) decreased when using WL. In particular, the crystallite size of ZnO chloride decreased from 28 to 15 nm after WL irradiation compared to the control. Even exposure to blue light and red light caused a decrease in size in almost all samples, in fact, as can be seen from the table, the only exception concerns the ZnO (acetate) sample irradiated with blue light where the size of the crystallites increases compared to control.The thermal effect of the energy emitted by LEDs could cause a thermal effect, which would lead to a slight expansion and deformation of the samples, resulting in changes in the size of the crystallites..

Equation 9 was used to analyse the dislocation density of the prepared samples:[102]

$$\delta = \frac{1}{D^2} \qquad (9)$$

Equation 10 was used to calculate the lattice strain for each of the prepared samples:

$$\varepsilon = \frac{\beta \cos(\theta)}{4} \qquad (10)$$

Lattice deformation is a measure of the distribution of lattice constants resulting from crystal imperfections such as lattice dislocations.[103-104]

The results in Table 3, which show the effects of white light irradiation on three samples (ZnO-nitrate, ZnO-acetate, and ZnO-chloride), demonstrate a decrease in D values and an increase in both density and strain values. In the case of exposure of ZnO to red and blue light, an increase in density and strain values is also observed in this case as in the case of white light. the only exception is given by the ZnO-acetate sample irradiated with blue light where these values are lower than the control. This suggests that the effectiveness of radiation in causing defects in the crystalline structure may be lower than irradiation with white light. This suggests that the effectiveness of the radiation could cause defects in the crystalline structure. The density of dislocations in a material is directly related to lattice deformation and inversely related to crystallite size (D).[105-106]

Table 4 provides a detailed overview of the lattice structure parameters of irradiated and non-irradiated ZnO NPs, including the degree of crystallinity, cell volume, and the length of the Zn–O bond.

Table 4. The lattice structure parameters (2 θ_{001} (°),2 θ_{002} (°), a (Å) c (Å) the degree of crystallinity (% DC), cell volume (V (Å^3)) and the length of the Zn–O bond L (Å)) before and after irradiation with LED lights for samples synthesized with zinc nitrate, zinc acetate, and zinc chloride.

Sample	**ZnO (Zinc nitrate as a precursor)**						
	2 θ_{001} (°)	2 θ_{002} (°)	a (Å)	c (Å)	% DC	V (Å^3)	L (Å)
Control	31.6805	34.3419	3.259	5.218	21.04	47.9876	1.9829
WL	31.5073	34.1729	3.276	5.243	19.99	48.7358	1.9932
BL	31.5298	34.1817	3.274	5.242	22.5	48.6558	1.9921
RL	31.5010	34.1446	3.277	5.248	23.34	48.7940	1.9939
Sample	**ZnO (Zinc acetate as a precursor)**						
	2 θ_{001} (°)	2 θ_{002} (°)	a (Å)	c (Å)	% DC	V (Å^3)	L (Å)
Control	31.3551	34.2212	3.292	5.236	20.62	49.1307	1.9988
WL	31.6331	34.3312	3.263	5.220	18.17	48.1424	1.9851
BL	31.5607	34.2411	3.271	5.233	22.00	48.4813	1.9897
RL	31.5684	34.2427	3.270	5.233	21.69	48.4560	1.9893
Sample	**ZnO (Zinc chloride as a precursor)**						
	2 θ_{001} (°)	2 θ_{002} (°)	a (Å)	c (Å)	% DC	V (Å^3)	L (Å)
Control	31.4735	34.1244	3.280	5.251	20.87	48.9052	1.9955
WL	31.4125	34.1253	3.286	5.251	19.16	49.0893	1.9980
BL	31.6033	34.2638	3.266	5.230	22.31	48.3230	1.9875
RL	31.3624	34.0211	3.291	5.266	21.13	49.3887	2.0020

From the XRD spectra of the samples, the lattice parameters of the hexagonal unit cell, denoted as 'a' and 'c', can be calculated using the equation (11) e (12).[107]

$$a = \frac{\lambda}{\sqrt{3}\ \sin(\theta)_{100}} \qquad (11)$$

$$c = \frac{\lambda}{\sin(\theta)_{002}} \qquad (12)$$

The values of the parameters a and c are strongly influenced by various factors such as the concentration of impurity atoms and the presence of defects. This deviation from the ideal wurtzite crystal structure is due to both crystal structure stability and ionicity.[108] On the one hand, free charge contributes to lattice expansion, which is proportional to the strain potential of the conduction band minimum and inversely proportional to the carrier density and bulk modulus. On the other hand, point defects, such as zinc antisites and oxygen vacancies, and extended defects, such as thread dislocations, also play a significant role in changing the lattice constants.[108]

Unit cell volumes could also be determined using lattice geometry, as shown below (13):[109]

$$V = \frac{\sqrt{3}a^2c}{2} = 0.866a^2c \qquad (13)$$

The Zn-O bond length was calculated using the equation (14):

$$L = \sqrt{\left[\frac{a^2}{3} + c^2(0.5 - \mu)^2\right]} \qquad (14)$$

Where (μ) represents the positional parameter of the wurtzite structure, indicating the amount of atomic displacement relative to the next plane along the c-axis, as defined in the equation (15):

$$\mu = \frac{a^2}{3c^2} + 0.25 \qquad (15)$$

These variations are an indication of the lengthening of the bond length and consequent increase in unit cell-volume or vice versa. Essentially, during irradiation, lattice atoms are displaced from their designated positions within the lattice structure. This displacement gives rise to various crystallographic defects such as interstitials and vacancies, also known as Frenkel pairs.[110] It is interesting to observe that the variation of V (Table 4) in relation to the radiation energy follows a similar trend to the variation of L with respect to the radiation energy. Consequently, the formation of these defects leads to an expansion or contraction of the lattice parameters along the c-axis and/or a-axis. This expansion or contraction can be due to two factors, either the presence of interactions between basal dislocations or the presence of structural defects, in particular oxygen vacancies.[111.]

It is a common phenomenon in nanocrystals that the lattice volume expands or contracts as the crystallite size decreases. This phenomenon is observed in metal nanocrystals such as Au and Pt,[112] and in semiconductor nanocrystals such as Si, ZnS, and CdSe,[113] where a reduction in crystallite size results in a contraction of the lattice volume. This contraction is attributed to the increase in surface tension with decreasing size. However, it is surprising that oxide nanocrystals typically exhibit lattice[114] expansion, as the surface tension should also increase with size reduction, causing the lattice to contract, similar to what is observed in metal nanocrystals.

The main cause of lattice volume expansion in oxide nanocrystals is widely attributed to the formation of defects from oxygen vacancies.[115-116]

Theoretical explanations also support the idea that perfect passivation of the nanocrystal surface can minimize lattice parameter fluctuations. For example, the observed lattice expansion in ZnO nanocrystals may be related to oxygen vacancies, broken coordinates, imperfect surface passivation, or basal dislocations.[117-118]

A comparison of the crystallinity percentages shows that white irradiation has lower crystallinity percentages than blue or red irradiated samples and the control. This suggests that the use of white irradiation would lead to the formation of disorder within the crystal structure.

In addition, the table shows that the positions of the orientation (002) peaks shift after irradiation, indicating a change in the lattice constant c. This variation is thought to be related to residual stresses in the crystal structure of ZnO.

These results serve as clear evidence of the influence of laser irradiation energy on the structural properties of the prepared ZnO NPs.[119]

ATR-FTIR spectra for ZnO NPs are shown in Figure 34. These spectra are of great importance as they allow the identification of functional groups and vibrational shifts at specific wave numbers, which are unique features of each material and compound.

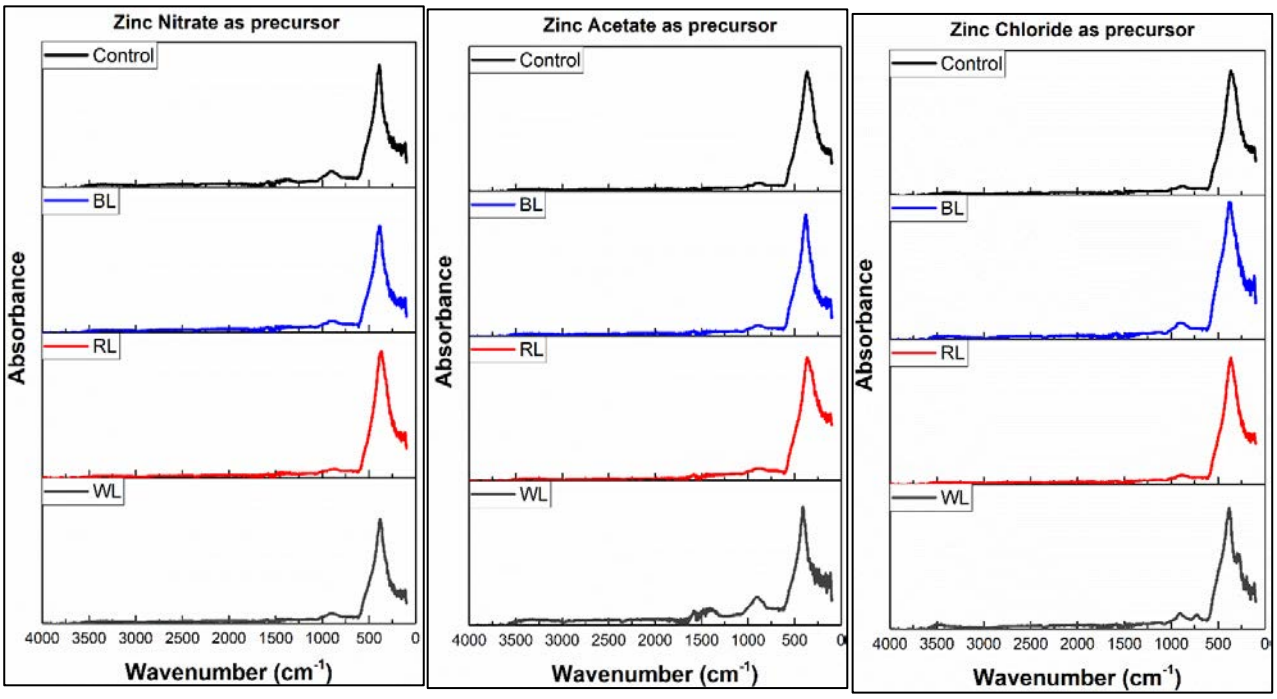

Figure 34. The ATR-FTIR spectra for the ZnO NPs before and after irradiations. left ATR-FTIR spectrum of ZnO synthesized with the precursor zinc nitrate, middle ATR-FTIR spectrum of ZnO synthesized with the precursor zinc acetate, and right ATR-FTIR spectrum of ZnO synthesized with the precursor zinc chloride.

The wavenumber values for the three irradiated samples, together with the corresponding value for the control, are given in Table 5.

Table 5. The wave number values for the three irradiated samples, together with the corresponding value for the control.

Sample	**ZnO(Zinc nitrate as a precursor)**	**ZnO(Zinc acetate as a precursor)**	**ZnO(Zinc chloride as a precursor)**	Assignment
Control	376 cm^{-1}	372 cm^{-1}	373 cm^{-1}	ν Zn-O
WL	381 cm^{-1}	408 cm^{-1}	381 cm^{-1}	ν Zn-O
BL	380 cm^{-1}	380 cm^{-1}	379 cm^{-1}	ν Zn-O
RL	367 cm^{-1}	365 cm^{-1}	366 cm^{-1}	ν Zn-O

The non-irradiated NPs show peaks at 376, 373, and 372 cm^{-1} for ZnO-nitrate, ZnO-acetate, and ZnO-chloride respectively, consistent with the Zn-O stretching vibrational mode and other reports.[120] However, after irradiation, a significant change in the wavenumber values is observed. In all cases, the presence of those bands at those values is evidence of successful synthesis of ZnO. As can be seen from the values shown in the table, blue and white light cause a shift towards higher wave

numbers (therefore higher energies), while with red light the opposite is observed (therefore lower energies), this observed variationis a direct result of the energy emitted by the three LEDs affecting the vibrational and rotational structure of the electronic state of the molecule. Irradiation can lead to changes in the number of atoms on the surface, resulting in surface defects and changes in the lattice parameters of the crystal structure as observed by XRD. These changes eventually manifest themselves as changes in the vibrational stretching mode of ZnO.[121]

The use of materials in optoelectronic devices and biomedical applications is strongly dependent on their optical properties, which are closely related to their atomic structure, electronic band structure, and electrical features. Energy gap (E_g) values serve as a means of determining these properties. An energy gap refers to a specific energy range where the density of electronic states is non-existent. Acting as a barrier to electrons, the energy gap separates two allowable electronic energy states. In contrast to the discrete energies within in individual atoms, materials exhibit bands of electronic energy states known as valence and conduction bands.[122] The valence band is the part of the atomic structure where the outer states are occupied by electrons.

Energy gap calculations have been carried out in numerous studies using different types of materials such as bulk materials, thin films, bio-organic materials, and nanomaterials.[123,124] Various techniques have been used to perform these calculations, including the photoluminescence (PL) method,[123-125] the Cody graph method,[126-128] the Tauc graph method,[129,130] and others.

Of these methods, the Tauc chart method is widely recognized as one of the most used to determine energy gap values. This method requires only UV-Visible spectra to calculate the energy gap.

The E_g value corresponding to the direct band gap transitions can be calculated from $(\alpha h\nu)^2$ versus hν plot, using the formula (16):

$$(\alpha h\nu)^2 = B\left(h\nu - E_g\right) \qquad (16)$$

where A is a constant for direct transitions, a is the optical absorption coefficient, h_ is the photon energy, and Eg is the optical band gap. E_g values were estimated from the intersection of the extrapolated linear part of the $(\alpha h\nu)^2$ curves with the energy axis.[131] As an example, Figure 35 shows the band gap calculated for ZnO control (zinc chloride as a precursor), and Table 6 summarises the observed band gap values.

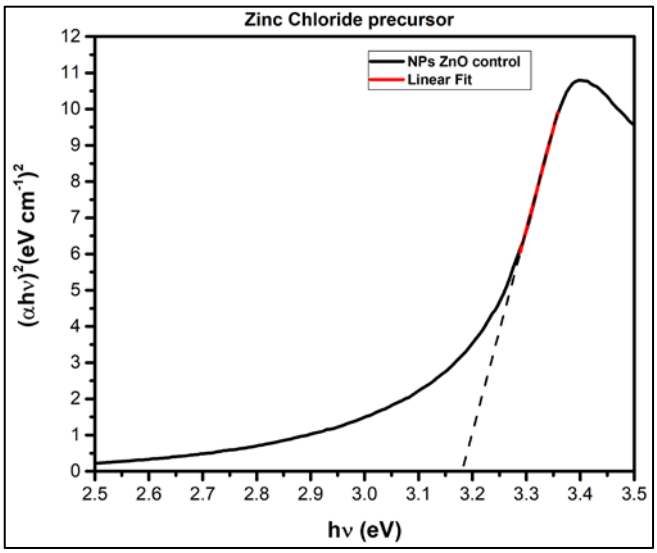

Figure 35. Tauc plot for ZnO NPs synthesized with the precursor zinc chloride without irradiation.

Table 6. Energy gap (E_g) values for the three irradiated samples, together with the corresponding value for the control

E_g (eV)	**ZnO (Zinc nitrate as a precursor)**	**ZnO (Zinc acetate as a precursor)**	**ZnO (Zinc chloride as a precursor)**
Control	3.10±0.03	3.22±0.03	3.22±0.01
WL	2.96±0.12	3.05±0.03	3.07±0.06
BL	3.03±0.04	2.98±0.03	3.15±0.04
RL	2.99±0.05	2.56±0.08	3.04±0.10

The variation in band gap between different samples can be attributed to several factors including structural parameters, carrier concentration, grain size, and defects. The presence of radiation-induced defects can affect the ZnO electronic subsystem and influence the band gap.

According to the existing literature, the reduction in band gap energy can be attributed to the formation of defects and vacancies within the lattice structure. Donor and acceptor defects are among the most common types of defects observed in ZnO.

Several types of donor defects are identified, such as zinc interstitials (Zn_i) and oxygen vacancies (V_o). Similarly, different types of acceptor defects are also identified, including zinc vacancies (V_{Zn}) and interstitial oxygen (O_i). [105]

About oxygen vacancies, it is widely recognized and accepted that their incorporation into ZnO produces a favourable and beneficial improvement in absorption characteristics.[132]

In the study by Wang et al.,[133] it was shown that the absorption edge of the material shifts towards longer wavelengths as the degree of oxygen vacancy increases. This change results in increased sensitivity to visible light. Similarly, Ansari et al.[134] found that the band gap of VO-ZnO nanostructures decreased to about 3.05 eV. Interestingly, the ultraviolet absorption is typically unchanged or slightly increased.[134-136]

By incorporating V_{Zn} into ZnO, there is a consequent improvement in the ability to absorb visible light and a reduction in the band gap. [132] However, this improvement is not as pronounced as that observed in oxygen-deficient ZnO. The formation of extended zinc $(Zn_i)_{ext}$ states at interstitial sites is possible by ionization of the defects, leading to localization of the defects within a disordered lattice.

The incorporation of defects into the lattice structure leads to a change in band gap values, causing both contraction and expansion. Furthermore, these defects can generate states within the band gap itself.[137-138]

These states have the potential to absorb photons below the bandgap threshold, thus affecting the absorption spectra. This can lead to the creation of artifacts and features that may falsely indicate a lower bandgap value than the actual, error-free measurement.[139-140]

Another aspect to consider is radiation. Radiation introduces additional carriers that cause the Fermi level to move towards the conduction band, leading to a reduction in the bandgap.[131]

Examining the data presented in Table 6, we can see that the bandgap values of the irradiated samples in some sample are lower than those of the control samples. This could indicate a shift in the Fermi level, as explained above.

The SEM micrographs in Figures 36, 37, and 38 show the samples exposed to red LED light and the corresponding control samples. Agglomeration of the particles has occurred in both the irradiation and control scenarios and complete separation did not occur.

The formation of particles is accompanied by a strong tendency of these particles to aggregate, a characteristic commonly associated with small particles and van der Waals forces operating at such scales. In addition, the topography of the particles plays a key role in determining the strength of these forces. The presence of rough surfaces has been shown to enhance van der Waals forces by

promoting mechanical interlocking between neighbouring particles, particularly when synthesis takes place in an aqueous environment.[141]

The effect of irradiation on particle morphology was observed for all three precursors, resulting in an interesting transformation. Figures 36,37, and 38 show SEM micrographs of the samples irradiated with Red light and respective controls. This change in morphology can be related to variations in the wavelengths of light used during the process.

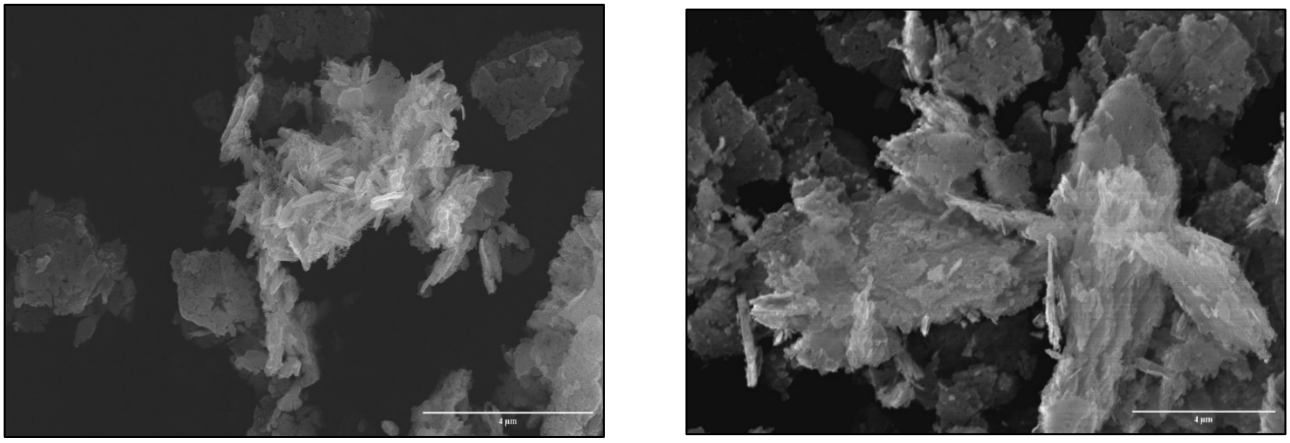

Figure 36. The SEM images of the ZnO powders before and after irradiation with Red light for zinc nitrate precursor. The scale bars in the figure SEM are 4 µm.

After examination of each case, some observations can be made. Regarding the nitrate precursor, there are differences between the two micrographs in Figure 36. In particular, the control sample shows a rod-shaped particle, suggesting growth along a specific direction. However, when exposed to red LED light, a clear change occurs. The rod structure disappears and is replaced by a plate-like morphology composed of clustered particles. The structure seems much more compact and extended.

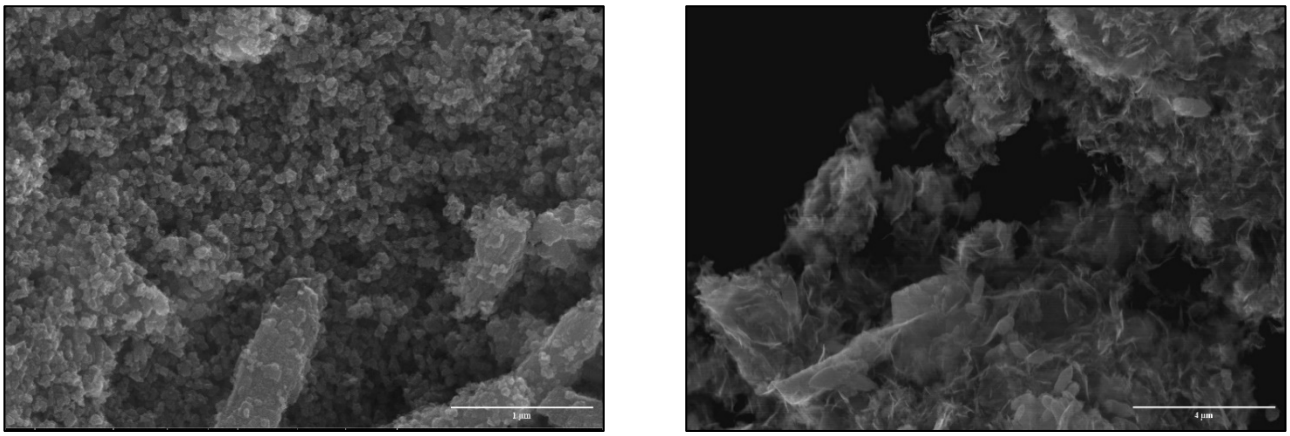

Figure 37. The SEM images of the ZnO powders before and after irradiation with Red light for zinc acetate precursor. The scale bars in the figure SEM are 1 µm and 4 µm.

The situation with the acetate precursor, Figure 37, shows a marked contrast: the effect of radiation on the morphology is much more pronounced than with nitrate. In the control group, we can observe spherical particles with irregular, agglomerated, and well-defined shapes. Under irradiation, however, these structures disappear completely, giving way to a combination of filamentous and rod-like formations.

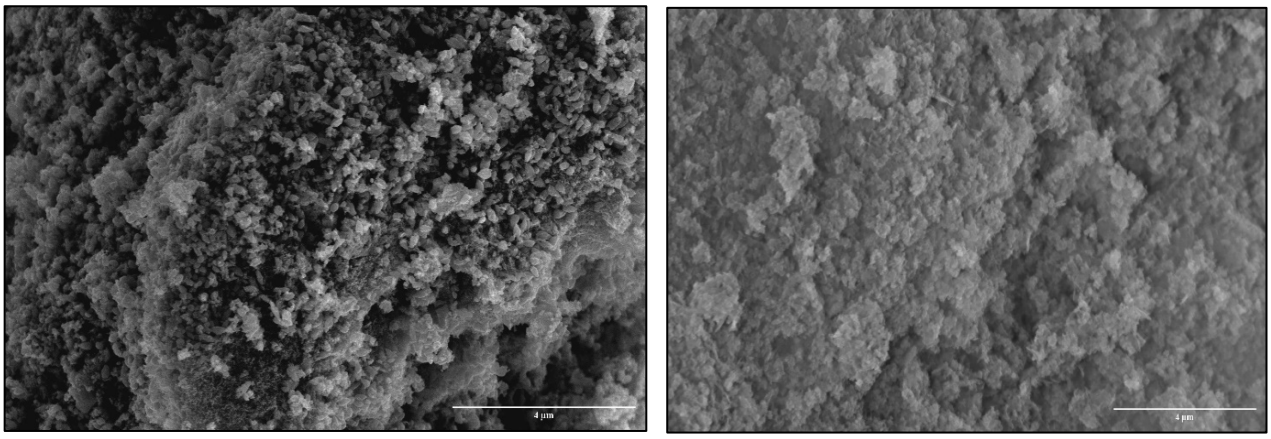

Figure 38. The SEM images of the ZnO powders before and after irradiation with Red light for zinc chloride precursor. The scale bars in the figure SEM are 4 µm.

In Figure 38, the use of zinc chloride as a precursor also leads to clear differences in the morphology of the two samples. Similar to the acetate control, the control sample consists of small, almost uniformly shaped, and densely packed particles.

However, in the red-light micrograph in figure 38 on the right, the particles in the control sample lose their distinct contours and instead form densely packed rough grains with blurred boundaries. The structure seems much more compact and extended.

5.2. BIOLOGICAL SYNTHESIS:

In recent years, green synthesis has attracted increasing attention as a simple, fast, cheap, and environmentally friendly method that uses non-toxic solvents and produces fewer harmful by-products.[142] The synthesis of metal nanoparticles comes from a variety of biological sources, including plant extracts, enzymes, and microorganisms, which can act as reducing, stabilizing, and coating agents for nanoparticle biosynthesis as a new method without environmental concerns and limited clinical applications. In this context, studies on a variety of different microorganisms such as bacteria, yeast, and fungi have shown that yeast has the advantages of high tolerance to metal ions and high metal production, making it a good candidate for nanoparticle synthesis. Enzymes are highly produced substances and their ability to bioaccumulate metals on bacteria.[143-144]

As a probiotic microorganism, the yeast *Saccharomyces cerevisiae* belongs to the division *Ascomycota* and the class *Saccharomycetes*.[145] Commonly known as 'brewer's yeast' or 'baker's yeast', *S. cerevisiae* is widely used in the brewing and baking industries.[146] In particular, it has been approved as safe by the FDA and is used as a biotherapeutic agent.[147,148] In addition, S. cerevisiae has excellent enzymatic activities, making it of great value in the food and pharmaceutical sectors.[149]

This non-pathogenic yeast is easily accessible and contains many bioactive compounds, including proteins and enzymes, that are useful for the environmentally friendly synthesis of nanoparticles. Sriramulu and Sumathi[150] conducted a study in which they used *S. cerevisiae* as a sequestering and reducing agent in a simple and inexpensive method to produce palladium nanoparticles.

S. cerevisiae has significant industrial value and is widely regarded as the ideal choice for NP production due to its physiological and genetic characteristics. Thus, the next phase of research focused on the use of brewer's yeast for the synthesis of ZnO nanoparticles.

The synthesis process involves several steps, which are described in detail in the Materials and Methods, section 4.4. In this discussion, the samples will be referred to as ZnO (N_CFE), ZnO (A_CFE), and ZnO (Cl_CFE), indicating the specific precursors used (nitrate, acetate, and chloride) and the inclusion of brewer's yeast in the synthesis. The corresponding control samples are labelled as ZnO (N), ZnO (A), and ZnO (Cl).

The samples labeled ZnO (N_CFE_WL), ZnO (A_CFE_WL), and ZnO (Cl_CFE_WL) correspond to the synthesis process carried out with three different precursors, together with the inclusion of a brewer's yeast solution and exposure to white light irradiation. The corresponding control samples are designated ZnO (N_WL), ZnO (A_WL), and ZnO (Cl_WL).

Figure 39 shows the XRD patterns of ZnO synthesized by biological methods, with and without exposure to different precursors.

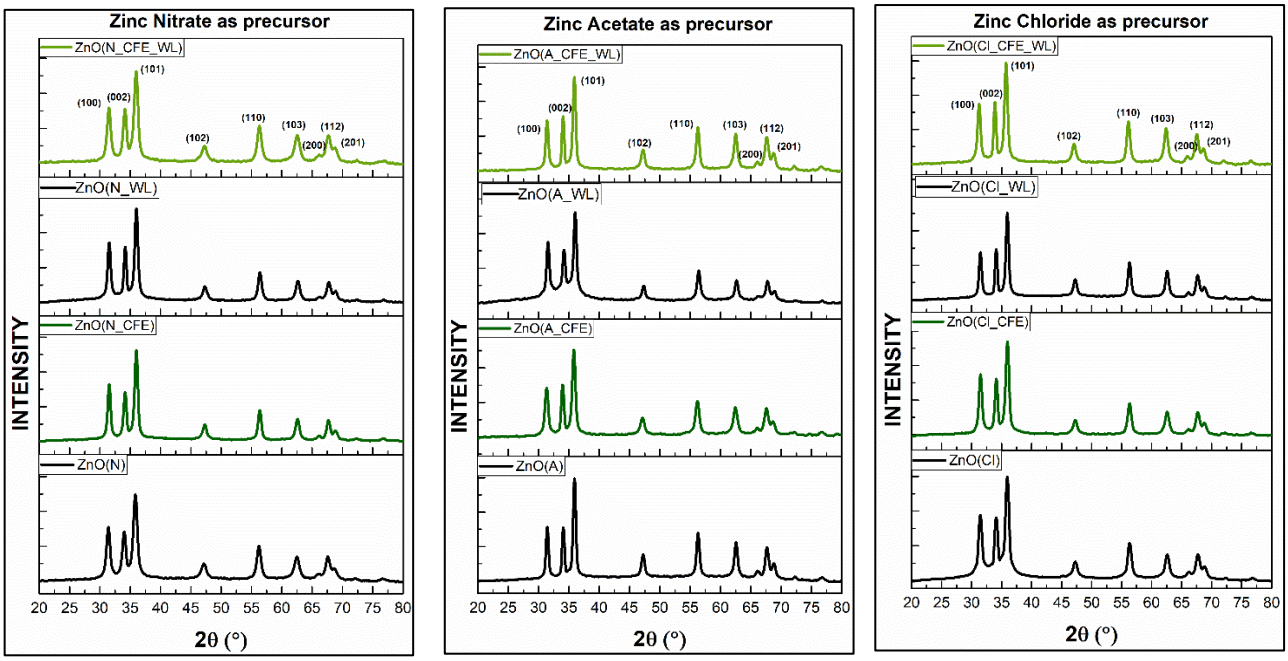

Figure 39. X-ray diffraction (XRD) spectra of ZnO: left XRD spectrum of ZnO synthesized with the zinc nitrate precursor, middle XRD spectrum of ZnO synthesized with the zinc acetate precursor, and right XRD spectrum of ZnO synthesized with the zinc chloride precursor with the use of brewer's yeast and combination of brewer's yeast and white LED radiation.

The diffraction peaks observed in the patterns can be attributed to a single phase of the hexagonal crystal structure, specifically space group $P6_3mc$ with space group number 186 (ICDD reference number (98-015-5780)20). Analysis of the spectra showed that no new peaks were detected after the use of yeast and the combination of the latter with white light irradiation, suggesting that this approach did not cause crystalline phases to appear or disappear.

Table 7 gives a breakdown of the structural analysis carried out on ZnO obtained through the biological synthesis. Equations 8,9, and 10 (paragraph 5.1) were used to determine the values for crystallite size, dislocation density, and lattice deformation.[101-102]

Table7. ZnO crystallite size (D), dislocation density(δ), and lattice strain(ε) for biological synthesis synthesized with zinc nitrate, zinc acetate, and zinc chloride.

hkl (101)	**ZnO (Zinc nitrate as a precursor)**		
	D(nm)	δ ($10^{-4}nm^{-2}$)	ε (10^{-4})
ZnO (N_CFE)	15.4312	41.9951	22.4632
ZnO (N)	24.2547	16.9983	14.2914
ZnO (N_CFE_WL)	16.9808	34.6806	20.4134
ZnO (N_WL)	24.2687	16.9788	14.2832
hkl (101)	**ZnO (Zinc acetate as a precursor)**		
ZnO (A_CFE)	18.8547	28.1289	18.3844
ZnO (A)	24.2583	16.9933	14.2893
ZnO (A_CFE_WL)	21.2182	22.2118	16.3367
ZnO (A_WL)	24.2499	17.0050	14.2942
hkl (101)	**ZnO (Zinc chloride as a precursor)**		
ZnO (Cl_CFE)	18.8646	28.0998	18.3749
ZnO (Cl)	24.2618	16.9885	14.2873
ZnO (Cl_CFE_WL)	21.2046	22.2402	16.3472
ZnO (Cl_WL)	21.2217	22.2044	16.3340

When comparing the samples with their respective controls, a significant difference in crystallite size, dislocation density, and lattice deformation was observed. The yeast cell-free extract (CFE) has a significant effect on the structural properties of ZnO, as evidenced by the significant decrease in crystallite size in the ZnO (N_CFE), ZnO (A_CFE), and ZnO (Cl_CFE) samples compared to their controls. Similarly, in the case of the ZnO (N_CFE_WL) and ZnO (A_CFE_WL) samples, the sizes are smaller than those of the control. However, the ZnO (Cl_CFE_WL) sample feature crystallite size comparable to its abiotic control (ZnO (Cl_WL) .

Moreover, the WL irradiation coupled with CFE use determined a similar increased in crystallite size for ZnO obtained from zinc acetate and chloride, whereas no substantial effect was detected upon using zinc nitrate as a precursor. This result could be traced back to the nature of the precursor used in the synthesis.

In terms of dislocation density and lattice strain, almost all biological samples, irradiated or not, show an increase in these two parameters. Specifically, ZnO (N_ CFE) and ZnO (N_CFE_WL) samples

show the highest levels of dislocation and lattice deformation, indicating a higher influence of the CFE when using zinc nitrate as a precursor. On the opposite, the ZnO (Cl_CFE_WL), showed dislocation and lattice deformation values comparable to those of its abiotic control.

The calculations for lattice parameters, degree of crystallinity, cell volume, and bond length were carried out using equations 11,12, 13, and 14 (paragraph 5.1).

Analysis of the XRD patterns of all samples, as shown by the data in Table 8, reveals a significant change in the crystal structure constants.

Table 8. Lattice structure parameters (a, c) degree of crystallinity (% DC), cell volume (V), and Zn–O bond length (L) for biological synthesis for samples synthesized with zinc nitrate, zinc acetate, and zinc chloride.

Sample	**ZnO (Zinc nitrate as a precursor)**						
	2 θ_{100} (°)	2 θ_{002} (°)	a (Å)	c (Å)	% DC	V (Å^3)	L (Å)
ZnO (N_CFE)	31.4332	34.0739	3.284	5.258	20.71	49.0980	1.9981
ZnO (N)	31.5253	34.2111	3.274	5.238	21.95	48.6288	1.9917
ZnO (N_CFE_WL)	31.5348	34.1448	3.273	5.248	20.85	48.6918	1.9925
ZnO (N_WL)	31.5858	34.2105	3.268	5.238	23.12	48.4483	1.9892
	ZnO (Zinc acetate as a precursor)						
	2 θ_{100} (°)	2 θ_{002} (°)	a (Å)	c (Å)	% DC	V (Å^3)	L (Å)
ZnO (A_CFE)	31.3831	33.9813	3.289	5.272	21.58	49.3812	2.0019
ZnO (A)	31.5626	34.2053	3.271	5.239	21.62	48.5249	1.9903
ZnO (A_CFE_WL)	31.4021	34.0546	3.287	5.261	19.25	49.2199	1.9998
ZnO (A_WL)	31.4445	34.0702	3.282	5.259	20.47	49.0688	1.9977
	ZnO (Zinc chloride as a precursor)						
	2 θ_{100} (°)	2 θ_{002} (°)	a (Å)	c (Å)	% DC	V (Å^3)	L (Å)
ZnO (Cl_CFE)	31.5152	34.1947	3.275	5.240	22.73	48.6819	1.9924
ZnO (Cl)	31.6006	34.2923	3.267	5.226	19.96	48.2921	1.9871
ZnO (Cl_CFE_WL)	31.2685	33.9074	3.300	5.283	21.11	49.83993	2.0081
ZnO (Cl_WL)	31.4911	34.1171	3.278	5.252	20.84	48.8621	1.9948

Examination of the results in table 8 shows that each sample exhibits an increase in the a and c parameters compared to their respective controls. This observation applies to both volume and length measurements. Analysing the values obtained in Table 8 several observations can be made. Considering the samples ZnO (N_CFE), ZnO (A_CFE), and ZnO (Cl_CFE), the lattice parameters, volume, and length show higher values than the respective controls. The use of brewer's yeast CFE results in a higher occurrence of defects or dislocations within the crystal lattice.[104] On the other hand, analysing the case of the samples ZnO (N_CFE_WL) and ZnO (A_CFE_WL), it can be observed that irradiation with white light combined with yeast does not further increase the number of defects along the crystal that we observed with yeast alone.

Observing the synthesis with zinc chloride for the sample ZnO (Cl_ CFE_WL), the lattice parameters, as well as the volume and length, show greater values than for all the other samples. When brewer's yeast is used in combination with white irradiation, there appears to be a greater presence of defects or dislocations along the crystal lattice in this case. In this case, a synergistic effect between the two variables (i.e., WL and CFE use) is observed, resulting in increased lattice values.

The trend of decreasing crystallinity can be observed in both irradiated and non-irradiated nitrate and acetate samples, indicating a similarity between them. However, a different pattern emerges in the chloride samples as the degree of crystallinity increases compared to the control. In addition, the data in table 8 shows that the peak positions of the (002) orientation undergo a shift upon the introduction of yeast CFE or the combination of radiation with it, suggesting a change in the lattice constant c. This change is thought to be related to the presence of residual stress within the crystal structure of ZnO. Figure 40 shows the ATR-FTIR spectra of ZnO NPs.

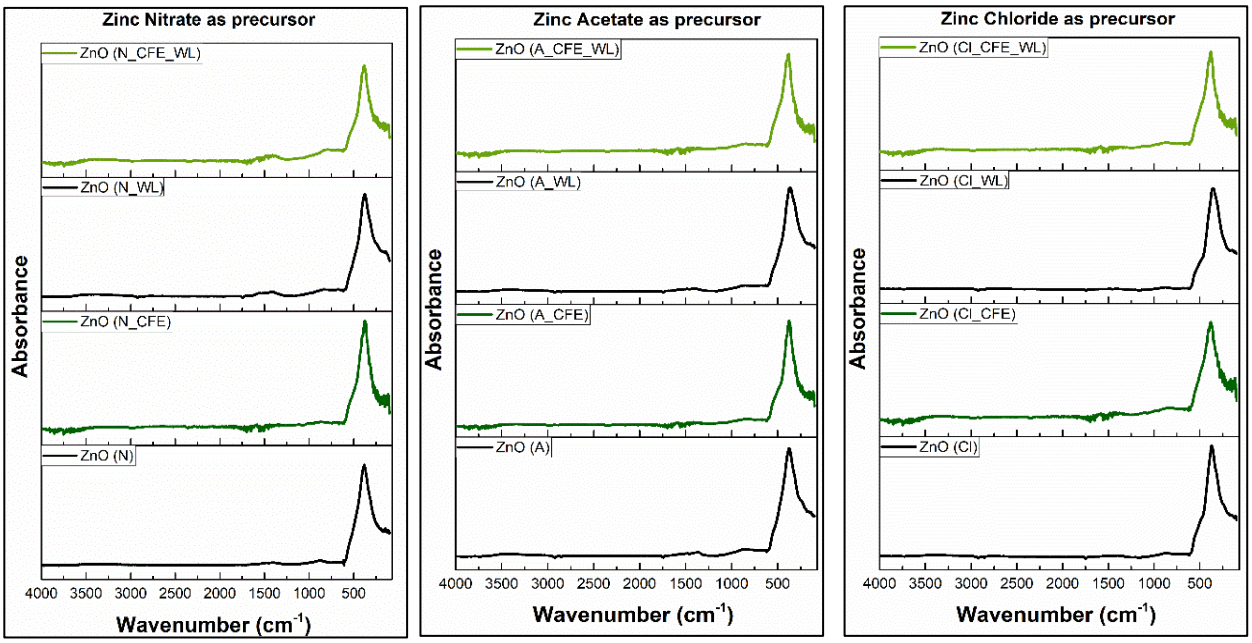

Figure 40. The ATR-FTIR spectra for the ZnO NPs: left ATR-FTIR spectrum of ZnO synthesized with the precursor zinc nitrate, middle ATR-FTIR spectrum of ZnO synthesized with the precursor zinc acetate, and right ATR-FTIR spectrum of ZnO synthesized with the precursor zinc chloride with the use of brewer's yeast and combination of brewer's yeast and white LED radiation.

For the biological samples, the wavenumber values are given in Table 9, together with the corresponding values for the control.

Table 9. The wavenumber values for the biological samples, together with the corresponding value for the control.

ZnO (Zinc nitrate as a precursor)		
Sample	Wavenumber (cm^{-1})	Assignment
ZnO (N_CFE)	378	ν Zn-O
ZnO (N)	376	ν Zn-O
ZnO (N_CFE_WL)	380	ν Zn-O
ZnO (N_WL)	380	ν Zn-O
ZnO (Zinc acetate as a precursor)		
Sample	Wavenumber (cm^{-1})	Assignment
ZnO (A_CFE)	377	ν Zn-O
ZnO (A)	376	ν Zn-O
ZnO (A_CFE_WL)	376	ν Zn-O
ZnO (A_WL)	365	ν Zn-O
ZnO (Zinc chloride as a precursor)		
Sample	Wavenumber (cm^{-1})	Assignment
ZnO (Cl_CFE)	380	ν Zn-O
ZnO (Cl)	372	ν Zn-O
ZnO (Cl _CFE_WL)	378	ν Zn-O
ZnO (Cl _WL)	357	ν Zn-O

From the values shown in Table 9, a change in wave number is observed in some cases when CFE is used alone or in combination with WL radiation (see samples ZnO (Cl_CFE), ZnO (A_CFE_WL) and ZnO (Cl_CFE_WL)). The vibrational and rotational structure of the molecular electronic state may be affected by the combination of CFE and WL. When capping is used in conjunction with radiation, it can cause changes in the number of atoms on the surface, leading to the formation of surface defects and changes in the lattice parameters of the crystal structure. These changes eventually lead to changes in the vibrational stretching mode of ZnO.The presence of oxygen or zinc vacancies is often cited as the main cause of defects.[151] The deformation that occurs within the crystal has a direct effect on the bond length and bond angle of the lattice[152], ultimately leading to the formation and modification of various defects in the crystal structure of ZnO. Previous research has shown that the introduction of extract molecules can induce a higher level of disorder in ZnO crystals.[104]

In addition, the hypothesis of a growth mechanism for green synthesized ZnO NPs is proposed, taking into account the potential contribution of phytochemicals in the extract. In the green synthesis

process, metal ions are encapsulated in an organic coating to ensure their stability after reduction. This encapsulation occurs in three stages: activation, growth, and termination. Substances present in the reaction medium may also act as covering agents and stabilizers for the nanoparticles.[153] It can be assumed that the Zn^{2+} ions of $Zn(CH_3COO)_2 \cdot 2H_2O$, for example, enter the growth and stabilization phase through the action of phytochemicals. Finally, the zinc ions bond with oxygen and the shape of the particle is formed. The number of biomolecules in the reaction medium should play a key role in the reduction, capping, and stabilization performance.[154] Consequently, these results effectively show the influence of the extract on the creation and/or correction of different defects within the ZnO band structure.

According to a literature report, the presence of capping agents during NP synthesis of ZnO can lead to intrinsic defects.[155] However, it is important to note that the effect of capping agents on defect formation in ZnO NPs is not a simple matter.[156]

The band gap values were calculated using the model described in paragraph 5.1. As an example, Figure 41 shows the band gap calculated for ZnO (A_CFE_WL). Table 10 shows the band gap values for all biological samples and their corresponding controls.

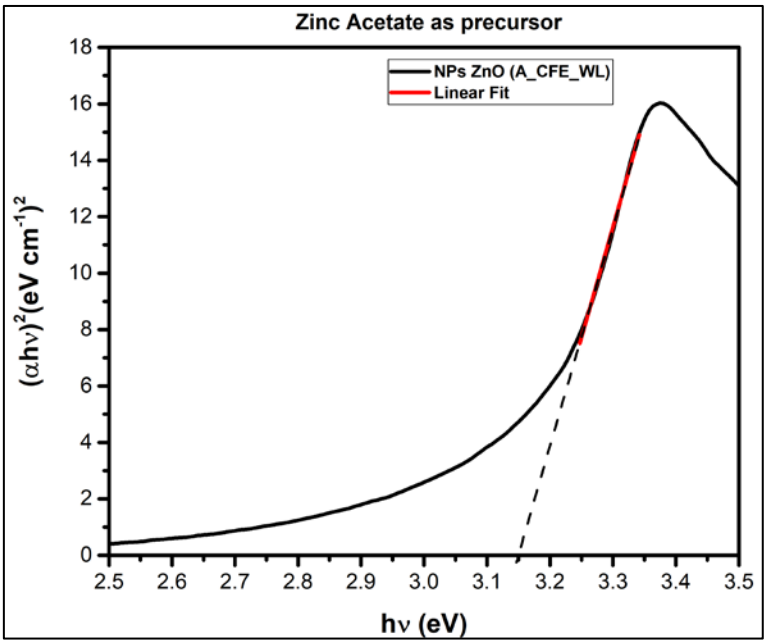

Figure 41. Tauc plot for ZnO NPs synthesized with the precursor zinc chloride with yeast and irradiation.

Table 10. Gap energy (Eg)values for the biological samples, together with the corresponding value for the control.

E_g (eV)	**ZnO (Zinc acetate as a precursor)**	**ZnO (Zinc acetate as a precursor)**	
ZnO (N_CFE)	3.18±0.02	ZnO (A_CFE)	2.92±0.01
ZnO (N)	3.03±0.08	ZnO (A)	2.79±0.03
ZnO (N_CFE_WL)	3.19±0.01	ZnO (A_CFE_WL)	3.13±0.03
ZnO (N_WL)	3.10±0.01	ZnO (A_WL)	2.83±0.04
E_g (eV)	**ZnO (Zinc chloride as a precursor)**		
ZnO (Cl_CFE)	3.12±0.02		
ZnO (Cl)	3.08±0.01		
ZnO (Cl_CFE_WL)	3.05±0.06		
ZnO (Cl_WL)	2.91±0.05		

For biological samples, different band gap values are observed compared to those calculated for chemically synthesized samples. [131] This band gap is supported by literature[104] data showing that the band gap energy of nanoparticles synthesized using biological synthesis is high in all samples. This suggests that brewer's yeast and WL irradiation have an influence on the modulation of different defect levels within ZnO.

The SEM micrographs in Figure 42 show samples synthesized using yeast CFE combined with WL irradiation.

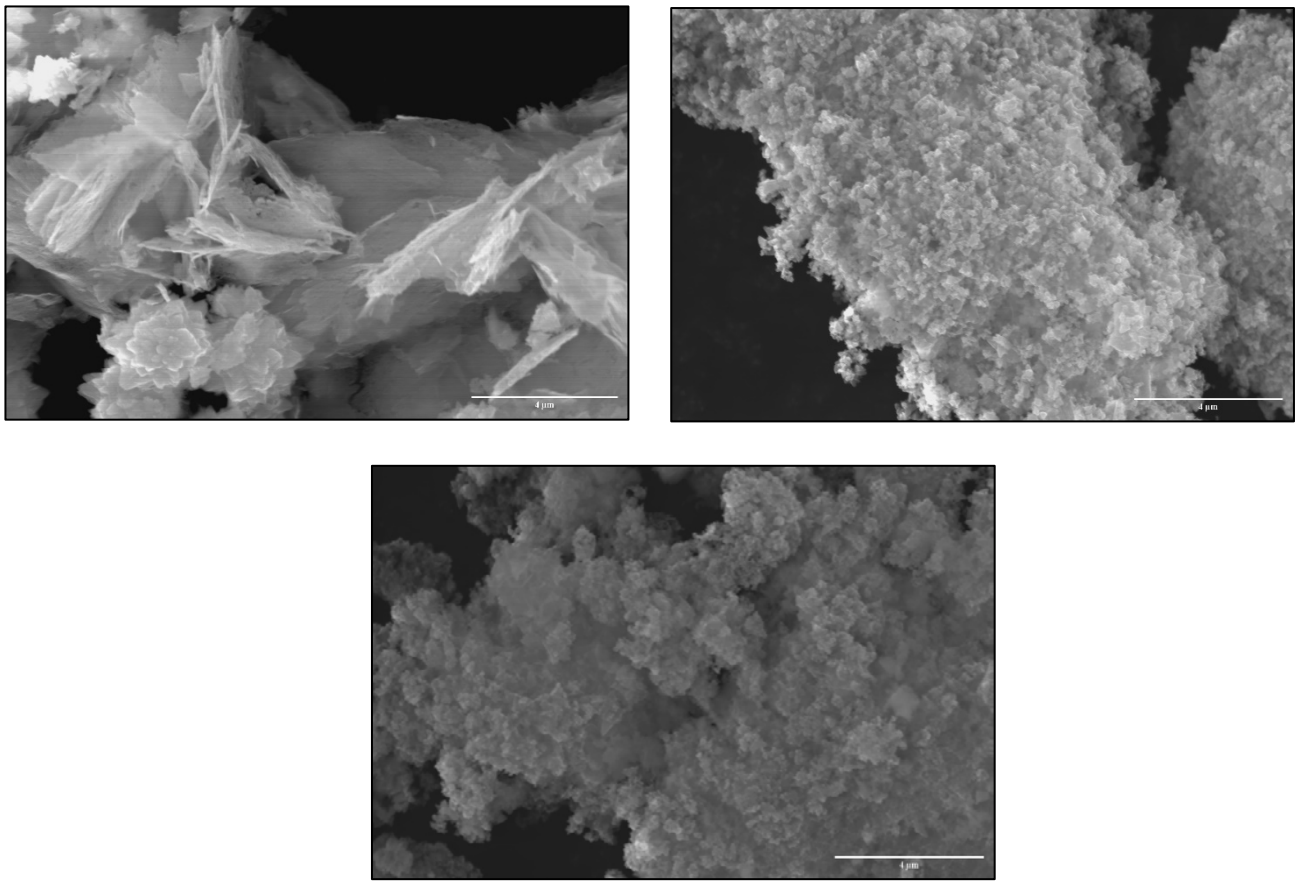

Figure 42. The SEM images of the biologically synthesized ZnO powders: top left the ZnO sample (N_CFE_WL), top right the zno sample (A_CFE_WL) and bottom the sample (Cl_CFE_WL). The scale bars in the figure SEM are 4 µm.

The ZnO (N_CFE_WL) sample showed a plated morphology with some aggregates resembling macroflowers (da indicare nella figura). On examining the A_CFE_WL and A_CFE_WL samples, however, it becomes evident that these micrographs share some similarities, as both show irregular aggregates with indistinct contours where different structures are virtually undistinguishable.

Overall, the results indicate that both irradiation and the use of yeast CFE affected the composition and physical properties of ZnO. However, it is equally important to consider the specific role played by the three different precursors used in this study: zinc nitrate salts, zinc acetate, and zinc chloride in both chemical and biological synthesis.

As described in the literature,[158] the observed variation in morphology can be attributed to the different adsorption strengths of the chloride, acetate, and nitrate anions on the surface. Chloride, being a halide, has a higher affinity for surface adsorption than the acetate and nitrate anions, which have weaker interactions. Particle growth is influenced by the interaction between the anions and the surface, with increased adsorption leading to a reduction in the growth process and the formation of smaller particles.[159]

The different functions of the three salts in particle formation were also confirmed by the observation that the nitrate anion acts as a non-coordinating ligand, leading to the expansion of the hexagonal wurtzite structure mainly along the c-axis (001 plane). In contrast, the acetate anion, acting as a chelating ligand, provides better regulation of the particle growth process.[160]

5.3. COPOLYMER SYNTHESIS:

Polysiloxanes, polyesters, polyurethanes, polyacrylics, and fluoropolymers have emerged as the polymers of choice in modern polymer composite systems due to their ability to provide the desired combination of properties and open up new opportunities for synergistic effects.[161-162] A prime example of such systems is polymer matrices incorporating siloxane groups derived from siloxanes and other organic polymeric materials.

The incorporation of siloxanes into polymeric materials has attracted considerable attention due to the possibility of combining the exceptional properties of polysiloxanes with specific properties of organic polymers.[163] These versatile polymers are widely used in a variety of applications and occupy a prominent position in the field of coatings, providing superior solutions to complex coating and protection problems.[164,165]

The chemistry of polysiloxanes provides valuable techniques for building these systems through the use of cross-linking reactions involving functional polysiloxanes.[166]

After careful analysis of the above factors, we have successfully created a linear silicone copolymer consisting of PDMS backbones, ureido units, and terminal catechol motifs. To achieve this, we made the necessary modifications to the synthesis procedure described in the literature, [167] as detailed in the Materials and Methods chapter, section 4.4.

Bis-aminopropyl terminated polysiloxanes were selected as the monomer, specifically with a PDMS structure of a specific chain length. The inherent flexibility of the PDMS structure will facilitate the movement of the polymer chains, allowing the material to heal.[168-169] To improve the inter- and intramolecular hydrogen bonding of the polymer, isophorone diisocyanate (IPDI) was chosen as the chain extender. This is because the isocyanate groups react readily with the amine group, even at low temperatures such as room temperature or 0°C, resulting in the formation of ureido units.[170-171]

In addition, the steric hindering effect of IPDI inhibits crystallization, thereby increasing chain mobility.[172]

Furthermore, the raw materials used in this study are readily available and conform to industry standards, making them highly suitable for large-scale production of supramolecular polysiloxanes. The copolymer design and the specific monomers used are shown in Figure 43.

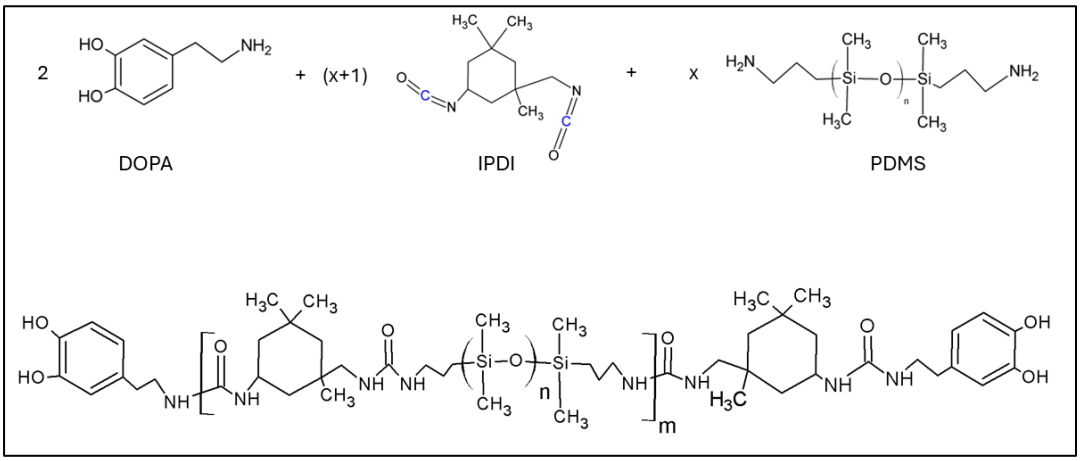

Figure 43. The design of the copolymer and the specific monomers used in the synthesis.

^{1}H and ^{13}C NMR, ATR-FT-IR spectroscopy, and XPS were used to validate the structure of the synthesized polymer.

Figures 44 and 45 show the ^{1}H NMR and ^{13}C NMR spectra respectively. Table 11 compares the chemical shifts of the copolymer with those of the individual monomers found in the literature.

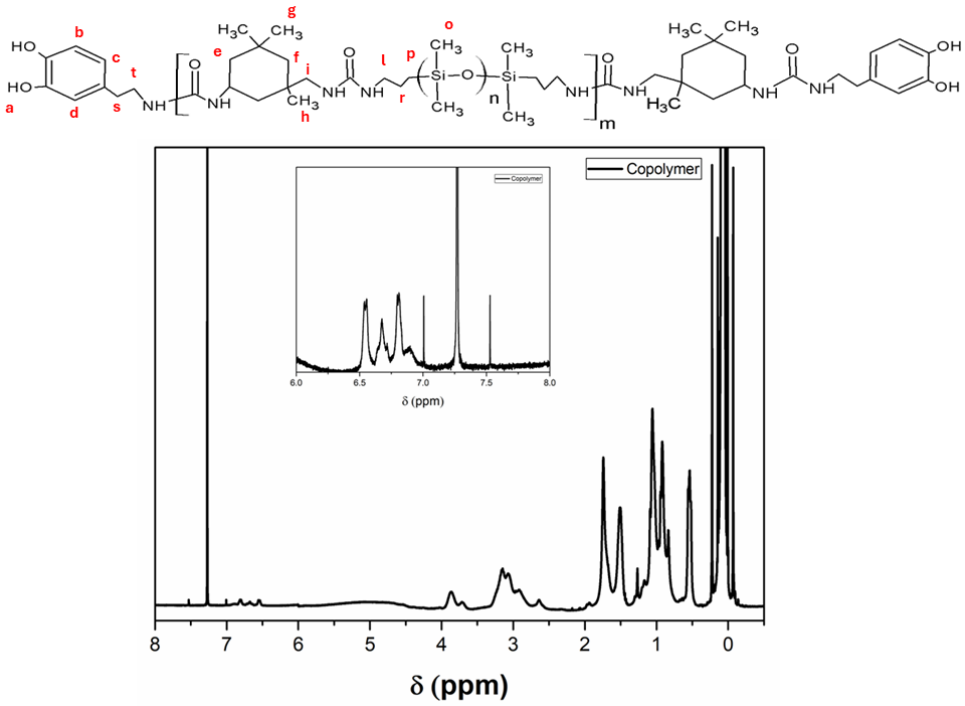

Figure 44. ^{1}H-NMR spectra of the copolymer and relative magnification to the region between 6.0 and 8.0 ppm of the spectrum.

Table 11. Assignments of the chemical shifts in the ^{1}H spectrum of the copolymer and relative chemical shifts of the individual monomers present in the literature.

Assignments		Copolymer (ppm)	Literature (ppm)
HO-CH-CH-OH	(**a**)	5.50-4.50	-
HO-C-CH	(**b**)	6.81	6.69 [173]
OH-C-CH=CH-C	(**c**)	6.55-6.53	6.48 [173]
OH-C-CH	(**d**)	6.64-6.72	6.64 [173]
CH_2-C(CH_3)$_2$- CH_2-C(CH_3)-CH_2	(**g**, **h**)	1.09-0.92	1.0-1.08 [174-175]
NH-CH-CH_2-C(CH_3)$_2$-CH_2	(**f**, **e**)	1.74	1.8 [174-175]
NH-CH_2-C	(**i**)	3.86-3.70	3.2-3.4 [174-175]
NH-CH_2-CH_2-CH_2-Si	(**l**)	3.16-2.89	2.64-2.7 [176-177]
NH-CH_2-CH_2-CH_2-Si	(**r**)	1.51-1.504	1.5 195 [176-177]
NH-CH_2-CH_2-CH_2-Si	(**p**)	0.56-0.52	0.51 195 [176-177]
CH_3-Si	(**o**)	0.22-0.07	0.05 195 [176-177]

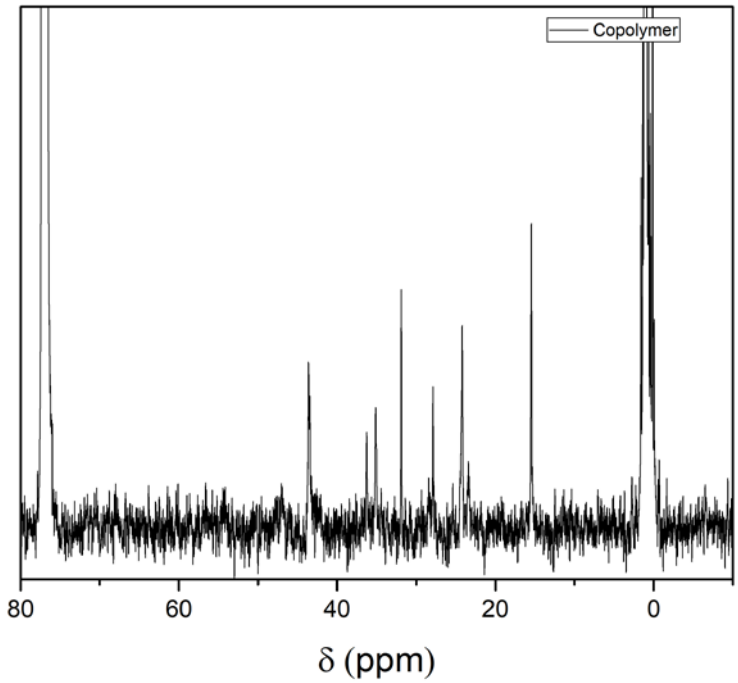

Figure 45.^{13}C-NMR spectra of the copolymer

The NMR spectrum of ^{13}C (Fig. 4) reveals the presence of the following signals: ($CDCl_3$, 43.6, 43.5 43.4, 36.29, 36.27, 36.19, 35.16, 35.11, 35.05, 31.88, 27.87, 24.19, 24.15, 24.21, 15.45, 1.57, 1.35, 1.15, 0.99, 0.62, 0.42, 0.17 ppm)

The chemical shift of the hydrogens labeled **b**, **c**, and **d** confirms the presence of dopamine in the copolymer, as these values correspond to the typical hydrogens present in the aromatic ring of dopamine.

Due to the overlapping contributions in the region between 2.91 and 3 ppm, the s- and t-bond signals could not be distinguished.

Comparing the values obtained in the ^{1}H NMR spectrum in Figure 44, with those present in the literature, an interesting observation concerns the shifts shown by the signals labelled **l** and **i**. Specifically, hydrogens involved in the bond NH-CH_2-CH_2-CH_2-Si (**l**) show a shift of about 0.60 ppm compared to the literature value given in the table. A similar observation is made for hydrogens associated with the bond NH-CH_2-C (**i**), which shifted of about 0.35 ppm from the literature value. This change in chemical shift could be due to a different chemical environment in which these hydrogens are found compared to the case of the single monomer. The observation made above suggests the possibility of intermolecular cross-linking between the different components of the polymer, indicating a successful synthesis.

To investigate the surface chemistry of the silicone film attenuated total reflectance infrared (ATR-IR) spectra were acquired. Figure 46 shows the spectra of the copolymer and the spectra associated with the individual monomers. The band assignments for the ATR-FTIR spectrum of the copolymer are given in Table 12.

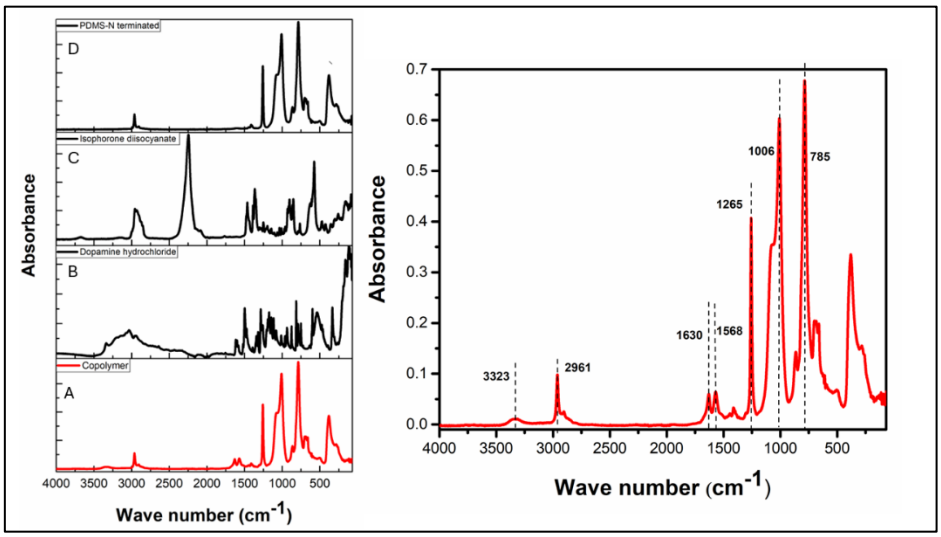

Figure 46. ATR-FTIR spectra on the left of the copolymer (A), dopamine hydrochloride (B), isophorone diisocyanate (C), and the N-terminated PDMS (D); on the right spectrum of the copolymer alone.

Table 12. Band assignments in ATR-FTIR spectra of copolymer.

Wavenumber(cm^{-1})	Assignment
3323	υ (N-H) hydrogen-bonded
2961	υ_{as} (C-H) in CH_3
1630	υ (C=O) hydrogen-bonded;AmideIstretch
1568	υ (C-N) + δ (N-H); AmideIIstretch&bend;
1413	δ_s (C-H); CH_3
1265	δ_s (C-H); CH_3
1009	υ_{as} (Si-O-Si)
864	δas (C-H) rocking;$Si(CH_3)_2$
785	υ_{as} (Si-C); $Si(CH_3)_2$
702	υ_s (Si-C); $Si(CH_3)_2$

On closer examination and analysis of the copolymer spectrum compared to that of PDMS alone, it is evident that two distinct peaks appear at 1630 cm^{-1} and 1568 cm^{-1}. These newly observed peaks provide evidence of the amide bond formation. This evidence is further supported in the spectrum where the isocyanate group stretching peak at 2245 cm^{-1} disappears, giving way to the formation of the amide bond in the copolymer. The presence of these two additional peaks and the absence of the corresponding isocyanate peak confirms the hypothesis derived from the analysis of the NMR spectra, namely the successful synthesis of the copolymer.

The analysis carried out by X-ray photoelectron spectroscopy further confirms what was observed in the NMR and ATR-FTIR spectra. Figure 47 shows the spectrum (XPS) while the experimental values of atomic concentration and stoichiometric composition are shown in Table 13.

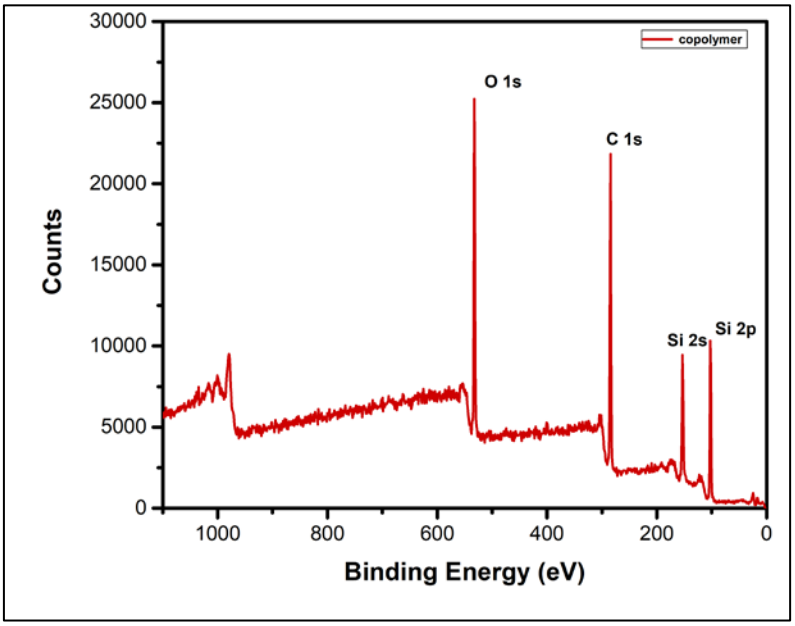

Figure 47. XPS spectrum of the supramolecular copolymer

.

Table 13. Experimental and stoichiometric atomic concentrations expressed in percentages.

	Experimental Atomic Concentration (%)	Stoichiometric Atomic Concentration (%)
Si 2p	21.18	20.89
C 1s	52.92	54.57
N1s	1.27	2.74
O 1s	24.63	21.80

As can be seen from the results reported in the table, the calculated experimental atomic concentration values confirmed the stoichiometric composition of the supramolecular copolymer, which was in line with the reported literature.

CHAPTER 6

6. PHOTOCATALYTIC TESTS:

6.1. PHOTOCATALYTIC ACTIVITY OF ZINC OXIDE POWDERS.

Solutions to the problems we humans create often come from nature itself, which acts as our inspiration. By closely observing the natural cycles that occur spontaneously, we can make scientific and technological progress. In the case of the photocatalytic process, we can draw an analogy with chlorophyll photosynthesis, a key biochemical mechanism used by plants to produce essential nutrients using sunlight (Figure 48). [178]

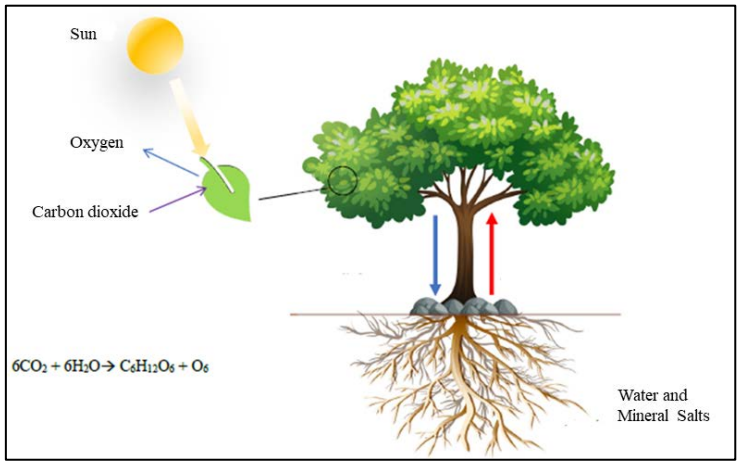

Figure 48. Illustration of the process of chlorophyll photosynthesis and related chemical reactions.

Sunlight acts as a catalyst for this reaction. The beginning of the preliminary research phase of the now-recognized photocatalytic process can be traced back to 1950 when Professor Kato Masuo began his revolutionary experiments. At the Kyoto Institute of Technology, this esteemed professor devoted his efforts to the development and widespread use of catalyst elements, which are chemical entities with the unique ability to alter the rate of a chemical reaction by accelerating or decelerating it.

In the early 1970s, Honda and Fujishima made a revolutionary discovery by using visible UV light to split water into hydrogen and oxygen through a process called electrolysis, resulting in:

$$H_2O + 2\,hv \longrightarrow \tfrac{1}{2}\,O_2 + H_2$$

This marked a significant advance in research that continued until 1979 when Professors Inoue and Fujishima revolutionized the field by studying the reaction of titanium dioxide crystals in water when exposed to sunlight.

Their publication ushered in the era of photocatalysis, drawing a direct parallel between the laboratory process and the natural phenomenon of photosynthesis. However, the scope of photocatalysis was initially limited to a specific range of light frequencies.[179]

In 2009, Professor Taoda Hiroshi achieved further success with the reaction by demonstrating its effectiveness under conditions of weaker light exposure, making the photocatalytic process more accessible. This process, known as photocatalysis, involves the use of certain semiconductor elements that, when exposed to sunlight, initiate chemical reactions involving reduction or oxidation, thereby accelerating the overall reaction. These semiconductors, known as photocatalysts, have strong oxidizing properties that enable them to break down inorganic and organic substances in their environment and convert them into harmless compounds such as water, salts, and carbon dioxide. When an electron is exposed to sunlight or artificial light, it undergoes a forbidden band transition, resulting in the creation of a vacancy or hole in the valence band, commonly referred to as H^+.[180]

Figure 49 illustrates how the interaction between electrons and gaps leads to the production of superoxide ions and hydroxyl radicals, which are responsible for both reduction and oxidation reactions.

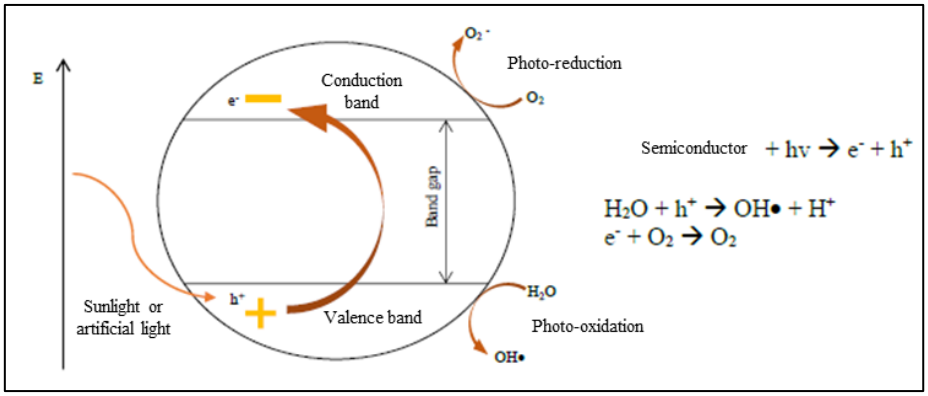

Figure 49. Illustration of photo-reduction and photo-oxidation reactions.

These reactions have a strong oxidizing effect and effectively break down pollutants in the atmosphere. The photocatalysis process begins when the photoinitiator absorbs enough energy to bridge the gap between the valence and conduction bands. This causes an electron to be lifted from the valence band to the conduction band, creating a gap (h^+) in the valence band and an excess of negative charge (e^-) in the conduction band. This change in the molecular structure creates an electron-lacuna pair, leading to an imbalance in the electronic charge. In conductive materials such

as metals, this pair is easily recombined. However, in semiconductors such as anatase (the crystalline form of titanium dioxide), these pairs last longer.[181]

After forming a hole and an electron, they migrate to the outer layer of the photocatalyst particles. Once there, they initiate a redox reaction in the presence of oxygen, air, water vapor, and liquid water. This allows the photocatalyst to regain its electronic equilibrium. As a result of these redox reactions, OH-free radicals are produced.[182]

These radicals then interact with the organic compounds absorbed or deposited on the surface of the photocatalyst, oxidizing them and transforming them into chemical species that no longer have the same environmental impact as the original compounds. It is important to note that the photocatalytic effect is a cyclic process and does not stop throughout the process. The samples were evaluated for their photocatalytic activity by measuring the degradation of methylene blue, which was chosen as a model pollutant based on its characteristics. This organic dye naturally loses its colour upon prolonged exposure to UV light, a process that can be enhanced by the presence of substances such as ZnO. Figure 50 shows as an example the UV-vis spectrum of the MB solution under 1 sun after treatment with ZnO synthesized with red light and using zinc chloride as a precursor.

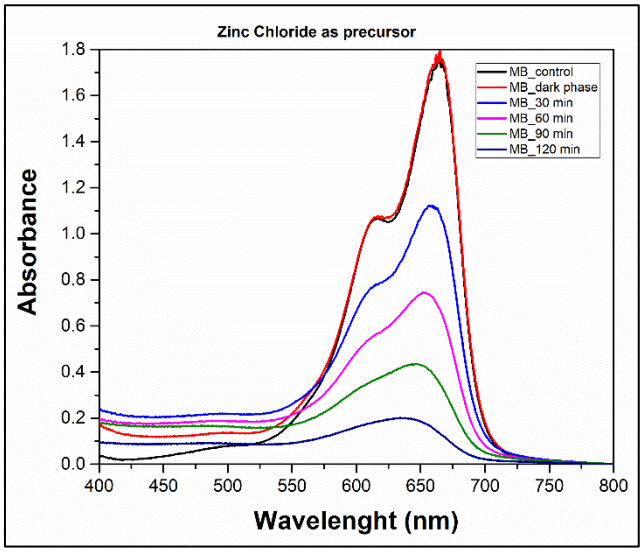

Figure 50. UV-vis spectrum of the MB solution under 1 sun after treatment with ZnO synthesized with red light and using zinc chloride as a precursor

The photodegradation rates for the chemically synthesized and biologically synthesized samples discussed in this thesis are shown in Tables 14 and 15 respectively.

Table 14. Photodegradation rates for ZnO samples synthesised with the different precursors and irradiated with white, blue, and red light and respective controls.

photodegradation rates (%)	**ZnO (Zinc nitrate as a precursor)**	**ZnO (Zinc acetate as a precursor)**	**ZnO (Zinc chloride as a precursor)**
control	87.7±0.1	78.3±0.2	63.0±0.2
WL	60.10±0.04	65.0±0.2	76.1±0.1
BL	71.1±0.2	51.4±0.2	55.4±0.1
RL	64.8±0.1	65.3±0.3	92.2±0.1

Table 15. Photodegradation rates for biologically synthesized ZnO samples and biologically combined with white light and respective controls.

photodegradation rates (%)	**ZnO (Zinc nitrate as a precursor)**
ZnO (N_CFE)	53.8±0.5
ZnO (N)	31.4±0.9
ZnO (N_CFE_WL)	66.9±0.3
ZnO (N_WL)	32.2±0.7
	ZnO (Zinc acetate as a precursor)
ZnO (A_CFE)	66.6±0.2
ZnO (A)	58,3±0.3
ZnO (A_CFE_WL)	60.06±0.05
ZnO (A_WL)	38.7±0.9
	ZnO (Zinc chloride as a precursor)
ZnO (Cl_CFE)	56.9±0.6
ZnO (Cl)	55.2±0.2
ZnO (Cl_CFE_WL)	96.68±0.05
ZnO (Cl_WL)	44.0±0.5

Looking at the data presented in the table, the photocatalytic efficiency of ZnO varies as a function of the synthesis procedure used. Specifically, ZnO (nitrate) and ZnO (acetate) samples produced under WL, BL, and RL irradiation significantly decreased their photocatalytic efficiency than the non-irradiated samples. In the case of ZnO (chloride) samples, only BL has a similar effect, whereas WL and RD improved the photocatalytic efficiency. Even more surprisingly, when exposed to RL, the photodegradation rate of ZnO (chloride) reaches 92%.

When analyzing biologically produced samples for nitrate samples, the photocatalytic characteristics show an improvement compared to the corresponding controls.

Regarding the biological synthesis process, a pattern similar to that of nitrate can also be observed for samples synthesized using zinc acetate. A particularly interesting scenario involves the use of zinc chloride as a precursor. the most interesting data comes from the combination of brewer's yeast and white light when zinc chloride is used as a precurosr, which results in an impressive 97% photodegradation after 120 minutes of exposure.

Previous research has shown that the properties of a material are determined by various factors such as particle size, crystal structure, morphology, and surface defects. Among these factors, intrinsic defects in metal oxides have attracted considerable interest due to their ability to modulate photocatalytic activity. Indeed, the presence of surface oxygen vacancies in ZnO is effective in producing a visible response and enhancing photocatalytic activity, as demonstrated by several studies in the literature.[183-184]

The consensus among researchers is that surface defects play a positive role in enhancing photocatalytic activity, while extensive structural defects have a detrimental effect on photocatalytic activity. [185-186] In addition, ZnO exhibits defect-rich chemistry, with different types of defects present in ZnO nanocrystals, including zinc vacancies (V_{Zn}), oxygen vacancies (V_O), zinc interstitials (Z_{ni}), oxygen interstitials (Oi), and oxygen antisites (O_{Zn}).[187-188] Photocatalytic activity can be enhanced or hindered by the presence of various defects, depending on the nature and location of these intrinsic imperfections. Consequently, the complex and controversial relationship between defect formation, defect structures, and photocatalytic activity underlines the complexity of this phenomenon.[189-190]

The decrease in catalytic activity observed in Table 14 is probably due to the generation of significant structural defects, particularly within the ZnO crystals, resulting from exposure to different light sources. These defects are thought to contribute to the reduction in photocatalytic activity. In contrast, samples that showed an increase in photocatalytic activity can be attributed to the presence of surface defects. [184] Considering a defect-free ZnO crystal, light-generated electrons and vacancies undergo rapid recombination, both within the crystal and on its surface. However, the situation becomes somewhat more complex when ZnO crystals containing defects are considered. The presence of surface defects, particularly clusters of defects, can effectively trap photogenerated holes and also promote the separation of photogenerated electron-lacuna pairs.[184-191]

In addition, the presence of surface defects in ZnO acts as a catalyst for the reaction between photogenerated holes and electron donors, effectively enhancing the photocatalytic process. Surface defects have a positive effect on the overall photocatalytic activity of ZnO.[192]

In other words, surface imperfections act as sites that capture and trap light-generated charge carriers, thereby improving the efficiency of charge separation and ultimately enhancing photocatalytic performance. In contrast, defects formed within the bulk of the material because of irradiation treatment function as centres where photogenerated charges recombine. As a result, the photocatalytic activity of the ZnO sample decreased significantly due to the reduced efficiency of charge separation, leading to a deterioration of its photocatalytic performance.[193-195]

The degradation rate of photocatalysis is governed by pseudo-first-order kinetics; Figure 51 shows the kinetic curves of MB degradation under 1 sun for zinc nitrate, zinc acetate, and zinc chloride samples by both chemical and biological routes.

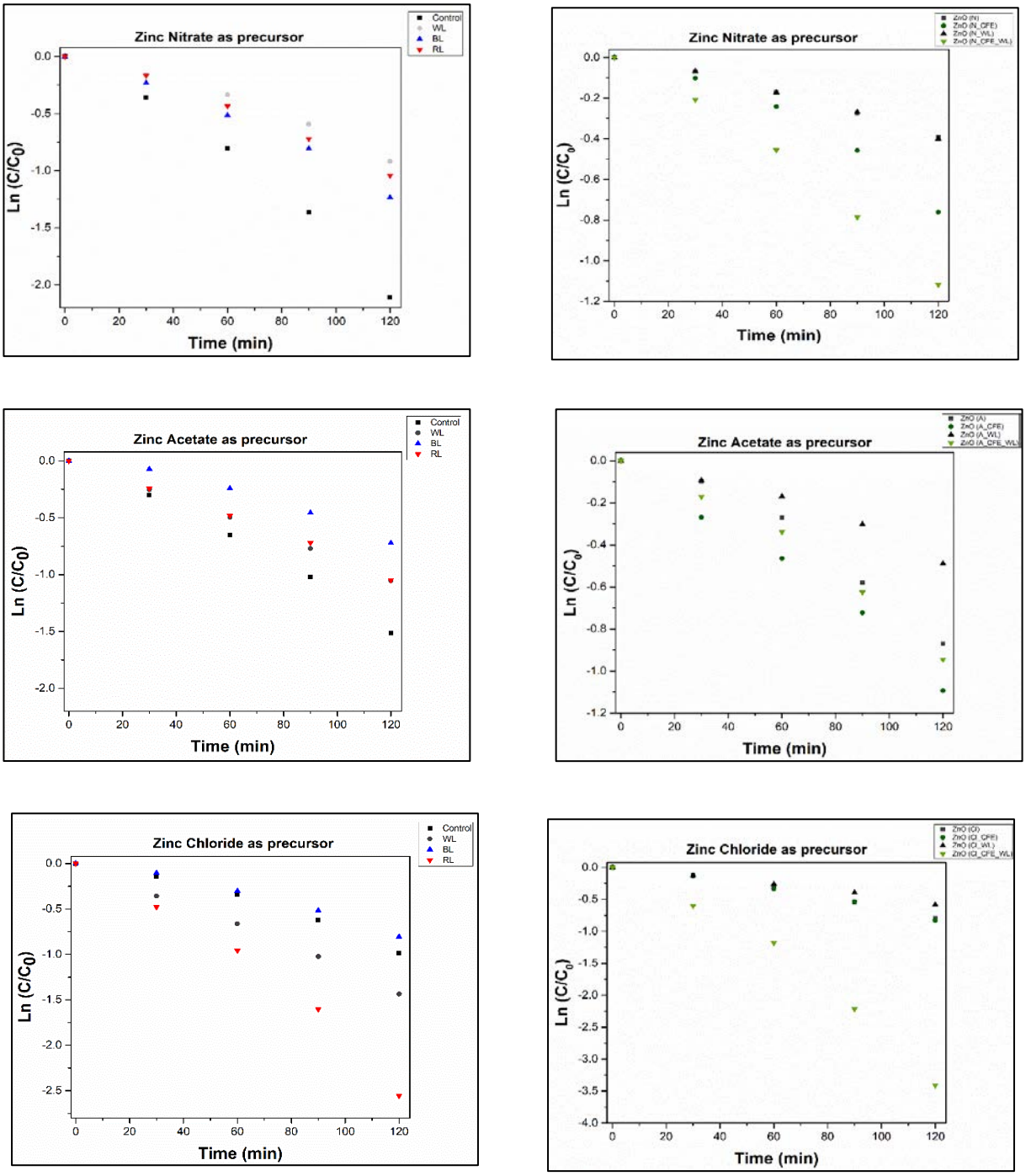

Figure 51. MB degradation kinetic curves under 1 Sun obtained for the different ZnO powders. The graphs on the left correspond to the samples synthesized chemically and irradiated with the different lights for the different precursors, those on the right correspond to the samples synthesized biologically and biologically combined with white light for the different precursors.

To determine the apparent rate constant (k), a linear regression model was employed, with the equation 17:

$$\ln(C\ /\ C_0) = -kt \qquad (17)$$

where C_0 represents the concentration after reaching adsorption-desorption equilibrium and C denotes the concentration after a specific duration of exposure to solar irradiation of the aqueous solution containing MB, k (min^{-1}) is the apparent rate constant for dye degradation .[196]

The values of the kinetic constants for the chemically and biologically synthesized samples discussed in this thesis are shown in Tables 16 and 17, respectively.

Table 16. Apparent rate constants (expressed in min^{-1}) of the degradation of the MB solution under solar irradiation of 1 Sun for the different precursors and irradiated with white, blue, and red light and respective controls.

Kinetic Constant (min^{-1})	**ZnO (Zinc nitrate as a precursor)**	**ZnO (Zinc acetate as a precursor)**	**ZnO (Zinc chloride as a precursor)**
control	(17.4±1.5) * 10^{-3}	(12.5±0.7) * 10^{-3}	(8.2±0.9) * 10^{-3}
WL	(7.5±0.7) * 10^{-3}	(9.0±0.2) * 10^{-3}	(11.8±0.3) * 10^{-3}
BL	(10.1±0.7) * 10^{-3}	(6.1±0.7) * 10^{-3}	(6.7±0.6) * 10^{-3}
RL	(8.8±0.6) * 10^{-3}	(8.6±0.3) * 10^{-3}	(20.8±1.9) * 10^{-3}

Table 17. Apparent rate constants (expressed in min-1) of MB solution degradation under solar irradiation equal to 1 Sun for biologically synthesized and biologically combined ZnO samples with white light and respective controls.

Kinetic Constant (min^{-1})	**ZnO (Zinc nitrate as a precursor)**
ZnO (N_CFE)	(6.2±0.8) * 10^{-3}
ZnO (N)	(3.3±0.1) * 10^{-3}
ZnO (N_CFE_WL)	(9.4±0.5) * 10^{-3}
ZnO (N_WL)	(3.4±0.2) * 10^{-3}
	ZnO (Zinc acetate as a precursor)
ZnO (A_CFE)	(8.8±0.6) * 10^{-3}
ZnO (A)	(7.4±0.9) * 10^{-3}
ZnO (A_CFE_WL)	(7.8±0.7) * 10^{-3}
ZnO (A_WL)	(4.0±0.4) * 10^{-3}
	ZnO (Zinc chloride as a precursor)
ZnO (Cl_CFE)	(6.9±0.5) * 10^{-3}
ZnO (Cl)	(6.7±0.5) * 10^{-3}
ZnO (Cl_CFE_WL)	(28.1±2.7) * 10^{-3}
ZnO (Cl_WL)	(4.8±0.2) * 10^{-3}

The degradation process of the organic dye starts when the ZnO samples undergo photooxidation, which activates the photocatalytic reaction. This process leads to the formation of an electron-lacuna pair, as shown in equation 21, which then interacts with the intermediates involved in the reaction, as shown in equation 18.

$$\text{ZnO+h}\nu \rightarrow \text{ZnO}\ (e_{CB}^{-} + h_{VB}^{+}) \qquad (18)$$

$$h_{VB}^{+} + MB \rightarrow MB^{\cdot +} \rightarrow oxidation\ of\ MB\ \ molecule \qquad (19)$$

The ZnO surface can attract and bind water molecules, which then react with h_{VB}^{+} to form $OH^{\cdot}$ radicals. These highly reactive radicals play an important role in the degradation of the MB dye. The generation of hydroxyl radicals can be achieved by the decomposition of water molecules (equation 20) or by the interaction between h_{VB}^{+} and OH^{-} ions (equations 21 and 22). These hydroxyl radicals are responsible for the complete degradation of the dyes. [197]

$$h_{VB}^{+} + H_2O \rightarrow H^{+} + OH^{\cdot} \quad (20)$$

$$h_{VB}^{+} + OH^{-} \rightarrow OH^{\cdot} \qquad (21)$$

$$OH^{\cdot} + MB \rightarrow oxidation\ of\ MB\ \ molecule \quad (22)$$

The ZnO (Cl_CFE_WL) sample gives the best result, with a photodegradation rate of 97% and a k value of $28 \cdot 10^{-3}.min^{-1}$

6.2. PHOTOCATALYTIC ACTIVITY OF THE COPOLYMER /ZnO.

Once the optimal ZnO candidate (Cl_CFE_WL) for the composite material has been determined, the sample was incorporated into the synthesized polymer matrix, and its photocatalytic activity was investigated.

Figure 52 shows UV-vis spectra of MB solution and kinetic curves of MB degradation under 1 sun after treatment with copolymer/ZnO (5 wt%) and copolymer/ZnO (10 wt%).

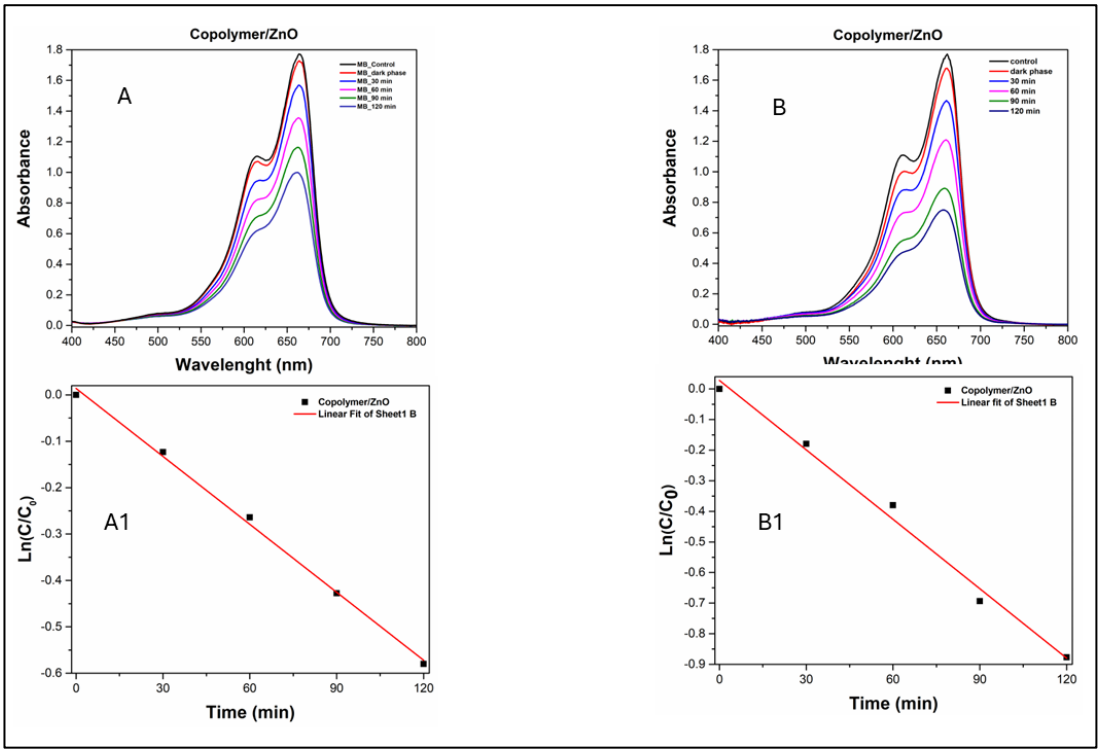

Figure 52. (A) UV-vis spectra of the MB solution after treatment with copolymer/ZnO (5% m/v) and (A1) MB degradation kinetic curve under 1 Sun obtained for the corresponding system. (B) UV-vis spectra of the MB solution after treatment with copolymer/ZnO (10% m/v) and (B1) MB degradation kinetic curve under 1 Sun obtained for the corresponding system.

The photodegradation rate for the samples discussed can be found in Table 18, together with the kinetic constant values.

Table 18. Apparent rate constants (expressed in min-1) of MB solution degradation under solar irradiation equal to 1 Sun for samples Copolymer/ZnO (5% wt) and Copolymer/ZnO (10% wt).

Sample	% photodegradation rates	Constant Kinetic (min^{-1})
Copolymer/ZnO (5% wt)	47±3	$(4.9\pm0.1) * 10^{-3}$
Copolymer/ZnO (10% wt)	56±2	$(7.6\pm0.4) *10^{-3}$

The photocatalytic decomposition kinetics of MB on copolymer films with different ZnO content shows a pseudo-first-order nature (Figure 51). The correlation between ln C_0/C and irradiation time is linear. Increasing the ZnO content from 5 wt% to 10 wt% results in a high rate of photocatalytic reaction, ranging from $4.9*10^{-3}$ min^{-1} to $7.6*10^{-3}$ min^{-1} after 2 h. Furthermore, the photocatalytic efficiency increases from 47% to 56%, as shown in the table. This improvement in efficiency can be attributed to the higher surface roughness, which leads to a larger surface area and consequently more active sites available for the photocatalytic reaction after ZnO loading.[198]

Comparing the values of the kinetic constants obtained with those reported in the literature for the apparent rate constants of MB degradation in visible light using nanocomposites containing ZnO incorporated in polymer matrices, it is evident that the values obtained exceed those documented in the literature. In particular, Di Mauro et al.[199] synthesized a ZnO/PMMA composite film that achieved a remarkable 40% dye degradation within 240 min, with a photodegradation rate of k $=2.6*10^{-3}$ min^{-} Lefatshe et al [200] prepared ZnO nanostructures in a cellulose host polymer, whose k value for the MB photodegradation under UV irradiation was $1.9*10^{-3}$ min^{-1}.

Furthermore, when comparing the efficiency of these materials with those composed of polymer matrix and TiO_2, the values observed also exceed those reported in the literature. The values obtained exceed those reported for poly (styrene-block-poly (acrylic acid) with TiO_2 gel ($0.44\text{-}1.7\cdot10^{-3}$ $min\text{-}^{1}$)[201] and are higher than those estimated for polysiloxane-TiO_2 nanocomposites ($7.6*10^{-3}$ min^{-1}, TiO_2 35%wt)[202] 6 e ($4.93*10^{-3}$ min^{-1}, TiO_2 35%wt).[203]

After irradiation for 120 minutes, the films consisting of polymer matrix and photocatalysts were subjected to ATR-FTIR characterization (Figure 53) to observe any changes in molecular structure caused by the irradiation treatment.

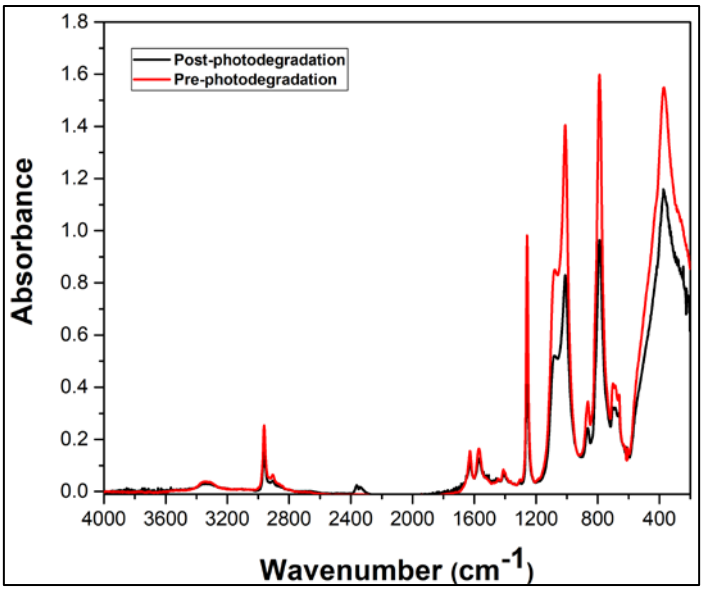

Figure 53. ATR-FTIR spectrum for the copolymer/ZnO system (10 wt%) before or after irradiation under solar irradiation equal to 1 Sun.

The spectrum shows the characteristic peaks of the copolymer (paragraph 5.3), and a peak at 374 typical of the stretching vibration of Zn-O. Besides, no structural changes are observed after photodegradation, indicating that the resulting ZnO/PMMA nanocomposite is stable and does not undergo structural degradation after irradiation.

CONCLUSIONS

The objective of this thesis project was to create composite nanomaterials by incorporating zinc oxide into a polymer matrix. Zinc oxide was selected because it possesses versatile properties, biocompatibility, and low toxicity. Polymeric materials were chosen for their convenience and ease of handling and production. The initial phase of the research focused on the synthesis of ZnO through a chemical and a biological approach. For both methods, we used three types of precursors: zinc nitrate, zinc acetate, and zinc chloride. Our exploration of chemical synthesis involved examining the impact of three types of radiation - white light, blue light, and red light - on the chemical and physical characteristics of the material, ultimately improving its photocatalytic properties when red light and the precursor zinc chloride were used. Similarly, in the field of biological synthesis, we investigated how the chemical-physical properties and photocatalytic capabilities of the material could be improved by using *S. cerevisiae* cell-free extract alone or a combination of this element and white light irradiation. XRD, ATR-FTIR, UV-Visible, and SEM approaches were used to characterize the obtained materials, and their photocatalytic properties were evaluated by studying the degradation of methylene blue.

Analysis of the XRD spectra showed that both the use of radiation alone and the CFE affected the structure of ZnO, as evidenced by the calculated cell parameter values. Both chemically and biologically synthesised samples showed significant differences in crystallite size, dislocation density, lattice deformation, and lattice parameters compared to their respective controls. This observation was further supported by an analysis of ATR-FTIR spectra and Energy gap calculations. Furthermore, SEM microscopy studies revealed morphological changes in both synthesis methods compared to the control group. These results are consistent with previous research and suggest the presence of defects within the zinc oxide crystal structure. Photocatalytic tests showed a remarkably high level of photodegradation for samples exposed to red light and zinc chloride precursor, with an approximate degradation rate of 92%. Similarly, the sample obtained by combining white light irradiation, yeast CFE, and zinc chloride precursor showed a photodegradation rate of around 97%.

In the second part of my thesis, a linear copolymer consisting of PDMS backbones, ureido units, and catechol motifs was prepared as a structure for the dispersion of nanostructured ZnO. Various characterisation techniques such as NMR, ATR-FTIR, and XPS were used to analyse the resulting material. The synthesis was considered successful based on the results obtained, which indicated the presence of intermolecular cross-linking between the different polymer components.

The final part of my research focused on the creation of a composite material consisting of the polymer matrix and ZnO. The effectiveness of the two samples in terms of photocatalytic performance was evaluated by studying the degradation of methylene blue adsorbed on their surfaces.

An increase of ZnO from 5 wt.% to 10 wt.% improved the rate of the photocatalytic reaction. Within a period of 2 h, the reaction rate increased from $4.9*10^{-3}$ min^{-1} to $7.6\cdot*0^{-3}$ min^{-1}. In addition, the efficiency of the photocatalytic process increased from 47% to 56%.

Comparing the values of the kinetic constants obtained in this study with those reported in the literature for the rate constants of MB degradation under visible light using nanocomposites containing ZnO incorporated in polymer matrices or those composed of polymer matrix and TiO_2, it was found that the values obtained are higher than those documented in the literature.

BIBLIOGRAPHY

1.Guo, D., Xie, G., & Luo, J. (2013). Mechanical properties of nanoparticles: basics and applications. *Journal of physics D: applied physics*, *47*(1), 013001.

2.Cao, G. (2004). *Nanostructures & nanomaterials: synthesis, properties & applications*. Imperial college press.

3.Korotcenkov, G., & Cho, B. K. (2010). INTRODUCTION TO NANOMATERIALS AND NANOTECHNOLOGY. *Chemical Sensors: Fundamentals of Sensing Materials Volume 2: Nanostructured Materials*, *2*, 1.

4.Rao, C. N. R., Müller, A., & Cheetham, A. K. (Eds.). (2006). *The chemistry of nanomaterials: synthesis, properties and applications*. John Wiley & Sons.

5.Roduner, E. (2006). Size matters: why nanomaterials are different. *Chemical society reviews*, *35*(7), 583-592.

6.Alivisatos, A. P. (1996). Perspectives on the physical chemistry of semiconductor nanocrystals. *The Journal of Physical Chemistry*, *100*(31), 13226-13239.

7.Rao, C. N. R., Kulkarni, G. U., Thomas, P. J., & Edwards, P. P. (2002). Size-dependent chemistry: properties of nanocrystals. *Chemistry–A European Journal*, *8*(1), 28-35.

8.Fernandez-Garcia, M., Martinez-Arias, A., Hanson, J. C., & Rodriguez, J. A. (2004). Nanostructured oxides in chemistry: characterization and properties. *Chemical reviews*, *104*(9), 4063-4104.

9.Abid, N., Khan, A. M., Shujait, S., Chaudhary, K., Ikram, M., Imran, M., ... & Maqbool, M. (2022). Synthesis of nanomaterials using various top-down and bottom-up approaches, influencing factors, advantages, and disadvantages: A review. *Advances in Colloid and Interface Science*, *300*, 102597.

10.Jamkhande, P. G., Ghule, N. W., Bamer, A. H., & Kalaskar, M. G. (2019). Metal nanoparticles synthesis: An overview on methods of preparation, advantages and disadvantages, and applications. *Journal of drug delivery science and technology*, *53*, 101174.

11.Charitidis, C. A., Georgiou, P., Koklioti, M. A., Trompeta, A. F., & Markakis, V. (2014). Manufacturing nanomaterials: from research to industry. *Manufacturing Review*, *1*, 11.

12.Kefeni, K. K., Msagati, T. A., & Mamba, B. B. (2017). Ferrite nanoparticles: synthesis, characterisation and applications in electronic device. *Materials Science and Engineering: B*, *215*, 37-55.

13.El-Khawaga, A. M., Zidan, A., & Abd El-Mageed, A. I. (2023). Preparation methods of different nanomaterials for various potential applications: A review. *Journal of Molecular Structure*, *1281*, 135148.

14.Nasrollahzadeh, M., Atarod, M., Sajjadi, M., Sajadi, S. M., & Issaabadi, Z. (2019). Plant-mediated green synthesis of nanostructures: mechanisms, characterization, and applications. In *Interface science and technology* (Vol. 28, pp. 199-322). Elsevier.

15.Chausali, N., Saxena, J., & Prasad, R. (2022). Recent trends in nanotechnology applications of bio-based packaging. *Journal of Agriculture and Food Research*, *7*, 100257.

16.Dasgupta, N., Ranjan, S., & Ramalingam, C. (2017). Applications of nanotechnology in agriculture and water quality management. *Environmental Chemistry Letters*, *15*, 591-605
.
17.Djurišić, A. B., Chen, X., Leung, Y. H., & Ng, A. M. C. (2012). ZnO nanostructures: growth, properties and applications. *Journal of Materials Chemistry*, *22*(14), 6526-6535.

18.Jangir, L. K., Kumari, Y., & Kumari, P. (2021). Zinc oxide-based light-emitting diodes and lasers. In *Nanostructured Zinc Oxide* (pp. 351-374). Elsevier.

19.Kołodziejczak-Radzimska, A., & Jesionowski, T. (2014). Zinc oxide—from synthesis to application: a review. *Materials*, *7*(4), 2833-2881.

20.Naveed Ul Haq, A., Nadhman, A., Ullah, I., Mustafa, G., Yasinzai, M., & Khan, I. (2017). Synthesis approaches of zinc oxide nanoparticles: the dilemma of ecotoxicity. *Journal of Nanomaterials*, *2017*.

21.Krol, A., Pomastowski, P., Rafińska, K., Railean-Plugaru, V., & Buszewski, B. (2018). Corrigendum to" Zinc oxide nanoparticles: synthesis, antiseptic activity and toxicity mechanism" Adv Colloid Interface Sci 249 (2017) 37-52. *Advances in colloid and interface science*, *254*, 100.

22.Sahu, D. R., Liu, C. P., Wang, R. C., Kuo, C. L., & Huang, J. L. (2013). Growth and application of ZnO nanostructures. *International Journal of Applied Ceramic Technology*, *10*(5), 814-838.

23.Özgür, Ü., Alivov, Y. I., Liu, C., Teke, A., Reshchikov, M. A., Doğan, S., ... & Morkoç, A. H. (2005). A comprehensive review of ZnO materials and devices. *Journal of applied physics*, *98*(4).

24.Xin-Yu, Z., Zhou-Wen, C., Yan-Peng, Q., Yan, F., Liang, Z., Li, Q., ... & Wen-Kui, W. (2007). Ab initio comparative study of zincblende and wurtzite ZnO. *Chinese Physics Letters*, *24*(4), 1032.

25.Heo, Y. W., Norton, D. P., & Pearton, S. J. (2005). Origin of green luminescence in ZnO thin film grown by molecular-beam epitaxy. *Journal of Applied Physics*, *98*(7).

26.HOUSECROFT, C. E. Catherine Housecroft, Alan G. Sharpe-Inorganic Chemistry-Prentice Hall (2012). *Vibrational spectroscopy*, *71*, 3-7.

27.Espitia, P. J. P., Soares, N. D. F. F., Coimbra, J. S. D. R., de Andrade, N. J., Cruz, R. S., & Medeiros, E. A. A. (2012). Zinc oxide nanoparticles: synthesis, antimicrobial activity and food packaging applications. *Food and bioprocess technology*, *5*, 1447-1464.

28.Agarwal, H., Kumar, S. V., & Rajeshkumar, S. (2017). A review on green synthesis of zinc oxide nanoparticles–An eco-friendly approach. *Resource-Efficient Technologies*, *3*(4), 406-413.

29.Mirzaei, H., & Darroudi, M. (2017). Zinc oxide nanoparticles: Biological synthesis and biomedical applications. *Ceramics International*, *43*(1), 907-914.

30.Gomez, J. L., & Tigli, O. (2013). Zinc oxide nanostructures: from growth to application. *Journal of Materials Science*, *48*, 612-624.

31.Madhumitha, G., Elango, G., & Roopan, S. M. (2016). Biotechnological aspects of ZnO nanoparticles: overview on synthesis and its applications. *Applied microbiology and biotechnology*, *100*, 571-581.

32.Uddin, M. J., Cesano, F., Scarano, D., Bonino, F., Agostini, G., Spoto, G., ... & Zecchina, A. (2008). Cotton textile fibres coated by Au/TiO2 films: Synthesis, characterization and self cleaning properties. *Journal of Photochemistry and Photobiology A: Chemistry*, *199*(1), 64-72.

33.Gao, Q., Zhu, Q., Guo, Y., & Yang, C. Q. (2009). Formation of highly hydrophobic surfaces on cotton and polyester fabrics using silica sol nanoparticles and nonfluorinated alkylsilane. *Industrial & Engineering Chemistry Research*, *48*(22), 9797-9803.

34.Atienzar, P., Ishwara, T., Illy, B. N., Ryan, M. P., O'Regan, B. C., Durrant, J. R., & Nelson, J. (2010). Control of photocurrent generation in polymer/ZnO nanorod solar cells by using a solution-processed TiO2 overlayer. *The Journal of Physical Chemistry Letters*, *1*(4), 708-713.

35.Tanasa, D., Vrinceanu, N., Nistor, A., Hristodor, C. M., Popovici, E., Bistricianu, I. L., ... & Broasca, G. (2012). Zinc oxide-linen fibrous composites: morphological, structural, chemical and humidity adsorptive attributes. *Textile research journal*, *82*(8), 832-844.

36.Vigneshwaran, N., Kumar, S., Kathe, A. A., Varadarajan, P. V., & Prasad, V. (2006). Functional finishing of cotton fabrics using zinc oxide–soluble starch nanocomposites. *Nanotechnology*, *17*(20), 5087.

37.Yadav, A., Prasad, V., Kathe, A. A., Raj, S., Yadav, D., Sundaramoorthy, C., & Vigneshwaran, N. (2006). Functional finishing in cotton fabrics using zinc oxide nanoparticles. *Bulletin of materials Science*, *29*, 641-645.

38.Mao, Z., Shi, Q., Zhang, L., & Cao, H. (2009). The formation and UV-blocking property of needle-shaped ZnO nanorod on cotton fabric. *Thin Solid Films*, *517*(8), 2681-2686.

39.Becheri, A., Dürr, M., Lo Nostro, P., & Baglioni, P. (2008). Synthesis and characterization of zinc oxide nanoparticles: application to textiles as UV-absorbers. *Journal of Nanoparticle Research*, *10*, 679-689.

40.Wang, R., Xin, J. H., Tao, X. M., & Daoud, W. A. (2004). ZnO nanorods grown on cotton fabrics at low temperature. *Chemical Physics Letters*, *398*(1-3), 250-255.

41.Jain, N., Bhargava, A., & Panwar, J. (2014). Enhanced photocatalytic degradation of methylene blue using biologically synthesized "protein-capped" ZnO nanoparticles. *Chemical Engineering Journal*, *243*, 549-555.

42.Lam, S. M., Sin, J. C., Abdullah, A. Z., & Mohamed, A. R. (2012). Degradation of wastewaters containing organic dyes photocatalysed by zinc oxide: a review. *Desalination and Water Treatment*, *41*(1-3), 131-169.

43.Lin, C. J., Lu, Y. T., Hsieh, C. H., & Chien, S. H. (2009). Surface modification of highly ordered TiO2 nanotube arrays for efficient photoelectrocatalytic water splitting. *Applied Physics Letters*, *94*(11).

44.Usman Ali, S. M., Ibupoto, Z. H., Chey, C. O., Nur, O., & Willander, M. (2011). Functionalized ZnO nanotube arrays for the selective determination of uric acid with immobilized uricase. *Chem. Sens*, *19*, 1-8.

45.Jianrong, C., Yuqing, M., Nongyue, H., Xiaohua, W., & Sijiao, L. (2004). Nanotechnology and biosensors. *Biotechnology advances*, *22*(7), 505-518.

46.Wang, D., Kou, R., Gil, M. P., Jakobson, H. P., Tang, J., Yu, D., & Lu, Y. (2005). Templated synthesis, characterization, and sensing application of macroscopic platinum nanowire network electrodes. *Journal of nanoscience and nanotechnology*, *5*(11), 1904-1909.

47.Topoglidis, E., Palomares, E., Astuti, Y., Green, A., Campbell, C. J., & Durrant, J. R. (2005). Immobilization and electrochemistry of negatively charged proteins on modified nanocrystalline metal oxide electrodes. *Electroanalysis: An International Journal Devoted to Fundamental and Practical Aspects of Electroanalysis*, *17*(12), 1035-1041.

48.Wang, J. X., Sun, X. W., Wei, A., Lei, Y., Cai, X. P., Li, C. M., & Dong, Z. L. (2006). Zinc oxide nanocomb biosensor for glucose detection. *Applied physics letters*, *88*(23).

49.Ali, S. M. U., Alvi, N. H., Ibupoto, Z., Nur, O., Willander, M., & Danielsson, B. (2011). Selective potentiometric determination of uric acid with uricase immobilized on ZnO nanowires. *Sensors and Actuators B: Chemical*, *152*(2), 241-247.

50.Brayner, R., Ferrari-Iliou, R., Brivois, N., Djediat, S., Benedetti, M. F., & Fiévet, F. (2006). Toxicological impact studies based on Escherichia coli bacteria in ultrafine ZnO nanoparticles colloidal medium. *Nano letters*, *6*(4), 866-870.

51.Stoimenov, P. K., Klinger, R. L., Marchin, G. L., & Klabunde, K. J. (2002). Metal oxide nanoparticles as bactericidal agents. *Langmuir*, *18*(17), 6679-6686.

52.Fortuny, A., Bengoa, C., Font, J., & Fabregat, A. (1999). Bimetallic catalysts for continuous catalytic wet air oxidation of phenol. *Journal of hazardous materials*, *64*(2), 181-193.

53.Shanmugam, S., Viswanathan, B., & Varadarajan, T. K. (2006). A novel single step chemical route for noble metal nanoparticles embedded organic–inorganic composite films. *Materials Chemistry and Physics*, *95*(1), 51-55.

54.Padmavathy, N., & Vijayaraghavan, R. (2008). Enhanced bioactivity of ZnO nanoparticles—an antimicrobial study. *Science and technology of advanced materials*.

55.Fakirov, S. (2017). *Fundamentals of polymer science for engineers*. John Wiley & Sons.

56.Brazel, C. S., & Rosen, S. L. (2012). *Fundamental principles of polymeric materials*. John Wiley & Sons.

57.Saheb, D. N., & Jog, J. P. (1999). Natural fiber polymer composites: a review. *Advances in Polymer Technology: Journal of the Polymer Processing Institute*, *18*(4), 351-363.

58.Morawetz, H. (2002). *Polymers: the origins and growth of a science*. Courier Corporation.

59.Rösler, J., Harders, H., & Bäker, M. (2007). *Mechanical behaviour of engineering materials: metals, ceramics, polymers, and composites*. Springer Science & Business Media.

60.Saraf, R. F., & Porter, R. S. (1988). Deformation of semicrystalline polymers via crystal–crystal phase transition. *Journal of Polymer Science Part B: Polymer Physics*, *26*(5), 1049-1057.

61.Tobolsky, A., & Eyring, H. (1943). Mechanical properties of polymeric materials. *The Journal of chemical physics*, *11*(3), 125-134.

62.Nasir, A., Kausar, A., & Younus, A. (2015). A review on preparation, properties and applications of polymeric nanoparticle-based materials. *Polymer-Plastics Technology and Engineering*, *54*(4), 325-341.

63.Ellis B. e R. Smith (2009). *Polymers, a property database* (2nd edition.). CRC press

64.Odian, G. (2004). *Principles of polymerization*. John Wiley & Sons.

65.Sperling, L. H. (2005). *Introduction to physical polymer science*. John Wiley & Sons.

66.Ward, I. M., & Sweeney, J. (2012). *Mechanical properties of solid polymers*. John Wiley & Sons.

67.Van Krevelen, D. W., & Te Nijenhuis, K. (2009). *Properties of polymers: their correlation with chemical structure; their numerical estimation and prediction from additive group contributions*. Elsevier.

68.Menczel, J. D., & Prime, R. B. (Eds.). (2009). Thermal analysis of polymers.

69.Wang, R. M., Zheng, S. R., & Zheng, Y. G. (2011). *Polymer matrix composites and technology*. Elsevier.

70.Vijay Kumar, V., Balaganesan, G., Lee, J. K. Y., Neisiany, R. E., Surendran, S., & Ramakrishna, S. (2019). A review of recent advances in nanoengineered polymer composites. *Polymers*, *11*(4), 644.

71.Chawla, K. K., & Chawla, K. K. (2019). Polymer matrix composites. *Composite Materials: Science and Engineering*, 139-198.

72.Neşer, G. (2017). Polymer based composites in marine use: history and future trends. *Procedia engineering*, *194*, 19-24.

73.Pilipović, A., Ilinčić, P., Petruša, J., & Domitran, Z. (2020). Influence of polymer composites and memory foam on energy absorption in vehicle application. *Polymers*, *12*(6), 1222.

74.Suddin, M. N., Salit, M. S., Ismail, N., Abd, M., & Zainuddin, S. (2004). Total design of polymer composite automotive bumper fascia. *J Sci Technol*, *12*, 39-45.

75.Ravishankar, B., Nayak, S. K., & Kader, M. A. (2019). Hybrid composites for automotive applications–A review. *Journal of Reinforced Plastics and Composites*, *38*(18), 835-845.

76.Rajak, D. K., Pagar, D. D., Menezes, P. L., & Linul, E. (2019). Fiber-reinforced polymer composites: Manufacturing, properties, and applications. *Polymers*, *11*(10), 1667.

77.Mohammed, L., Ansari, M. N., Pua, G., Jawaid, M., & Islam, M. S. (2015). A review on natural fiber reinforced polymer composite and its applications. *International journal of polymer science*, *2015*.

78.Mohammed, L., Ansari, M. N., Pua, G., Jawaid, M., & Islam, M. S. (2015). A review on natural fiber reinforced polymer composite and its applications. *International journal of polymer science*, *2015*.

79.Zagho, M. M., Hussein, E. A., & Elzatahry, A. A. (2018). Recent overviews in functional polymer composites for biomedical applications. *Polymers*, *10*(7), 739.

80.Yunas, J., Mulyanti, B., Hamidah, I., Mohd Said, M., Pawinanto, R. E., Wan Ali, W. A. F., ... & Yeop Majlis, B. (2020). Polymer-based MEMS electromagnetic actuator for biomedical application: A review. *Polymers*, *12*(5), 1184.

81.Ghalia, M. A., & Dahman, Y. (2016). Advanced nanobiomaterials in tissue engineering: Synthesis, properties, and applications. In *Nanobiomaterials in soft tissue engineering* (pp. 141-172). William Andrew Publishing.

82.Arumugam, S., Kandasamy, J., Md Shah, A. U., Hameed Sultan, M. T., Safri, S. N. A., Abdul Majid, M. S., ... & Mustapha, F. (2020). Investigations on the mechanical properties of glass fiber/sisal fiber/chitosan reinforced hybrid polymer sandwich composite scaffolds for bone fracture fixation applications. *Polymers*, *12*(7), 1501.

83.Srivastava, P., & Kalam, S. A. (2019). Natural polymers as potential antiaging constituents. *Pharmacognosy-Medicinal Plants*, 1-25.

84.Davies, P. (2016). Environmental degradation of composites for marine structures: new materials and new applications. *Philosophical Transactions of the Royal Society A: Mathematical, Physical and Engineering Sciences*, *374*(2071), 20150272.

85.Shenoi, R. A., Dulieu-Barton, J. M., Quinn, S., Blake, J. I. R., & Boyd, S. W. (2011). Composite materials for marine applications: key challenges for the future. In *Composite Materials: A vision for the Future* (pp. 69-89). Springer London.

86.L. Colleselli, M.Mutschlechner, M.Spruck, P.Vrabl, S.Zeilinger and H.Schöbel, Light-mediated biosynthesis of size-tuned silver nanoparticles using Saccharomyces cerevisiae extract. At the time of writing the following thesis, the article is under revision.

87.Walter, A., & Schöbel, H. (2023). Shed light on photosynthetic organisms: a physical perspective to correct light measurements. *Photosynthesis Research*, *156*(3), 325-336.

88.de Oliveira Jr, O., Marystela, F. L., de Lima Leite, F., & Da Róz, A. L. (Eds.). (2017). *Nanocharacterization techniques*. William Andrew.

89.Wang, H., & Chu, P. K. (2013). Surface characterization of biomaterials. In *Characterization of biomaterials* (pp. 105-174). Academic Press.

90.Norrish, K., & Taylor, R. (1962). Quantitative analysis by X-ray diffraction. *Clay minerals bulletin*, *5*(28), 98-109.

91.Pawar, A. R., Khade, P. D., & Sabale, S. K. (2020). Infrared spectroscopy: a review. *World J Pharm Res*, *9*, 465-478.

92.Ertl, G., & Küppers, J. (1985). *Low energy electrons and surface chemistry* (Vol. 87, p. 143). Weinheim: Vch.

93.Diehl, B. (2008). Principles in NMR spectroscopy. In *NMR Spectroscopy in Pharmaceutical Analysis* (pp. 1-41). Elsevier.

94.Ikram, M., Rashid, M., Haider, A., Naz, S., Haider, J., Raza, A., ... & Maqbool, M. (2021). A review of photocatalytic characterization, and environmental cleaning, of metal oxide nanostructured materials. *Sustainable Materials and Technologies*, *30*, e00343.

95.Sajjad, A., Bhatti, S. H., Ali, Z., Jaffari, G. H., Khan, N. A., Rizvi, Z. F., & Zia, M. (2021). Photoinduced fabrication of zinc oxide nanoparticles: Transformation of morphological and biological response on light irradiance. ACS omega, 6(17), 11783-11793.

96.Sakamoto, M., Fujistuka, M., & Majima, T. (2009). Light as a construction tool of metal nanoparticles: Synthesis and mechanism. *Journal of Photochemistry and Photobiology C: Photochemistry Reviews*, *10*(1), 33-56.

97.Ha, S. W., Lee, J. K., & Beck Jr, G. R. (2017). Synthesis of pH stable, blue light-emitting diode-excited, fluorescent silica nanoparticles and effects on cell behavior. *International Journal of Nanomedicine*, 8699-8710.

98.Soren, S., Kumar, S., Mishra, S., Jena, P. K., Verma, S. K., & Parhi, P. (2018). Evaluation of antibacterial and antioxidant potential of the zinc oxide nanoparticles synthesized by aqueous and polyol method. *Microbial pathogenesis*, *119*, 145-151.

99.Itoh, N. (1998). Subthreshold radiation-induced processes in the bulk and on surfaces and interfaces of solids. *Nuclear Instruments and Methods in Physics Research Section B: Beam Interactions with Materials and Atoms*, *135*(1-4), 175-183.

100.Arshak, K., & Korostynska, O. (2006). Response of metal oxide thin film structures to radiation. *Materials Science and Engineering: B*, *133*(1-3), 1-7.

101.Solati, E., Dejam, L., & Dorranian, D. (2014). Effect of laser pulse energy and wavelength on the structure, morphology and optical properties of ZnO nanoparticles. *Optics & Laser Technology*, *58*, 26-32.

102.Shkir, M., Kilany, M., & Yahia, I. S. (2017). Facile microwave-assisted synthesis of tungsten-doped hydroxyapatite nanorods: a systematic structural, morphological, dielectric, radiation and microbial activity studies. *Ceramics International*, *43*(17), 14923-14931.

103.Suryanarayana, C., Norton, M. G., Suryanarayana, C., & Norton, M. G. (1998). *X-rays and Diffraction* (pp. 3-19). Springer US.

104.Sarkar, T., Kundu, S., Ghorai, G., Sahoo, P. K., & Bhattacharjee, A. (2023). Structural, spectroscopic and morphology studies on green synthesized ZnO nanoparticles. *Advances in Natural Sciences: Nanoscience and Nanotechnology*, *14*(3), 035001.

105.Kaur, P., Kaur, S., Arora, D., Kandasami, A., & Singh, D. P. (2019). Correlation among lattice strain, defect formation and luminescence properties of transition metal doped ZnO nano-crystals prepared via low temperature technique. *Materials Research Express*, *6*(11), 115920.

106.Huang, G. R., Huang, J. C., & Tsai, W. Y. (2016). Origin of sample size effect: Stochastic dislocation formation in crystalline metals at small scales. *Scientific Reports*, *6*(1), 39242.

107.Li, J. L., & Gu, M. (2009). Gold-nanoparticle-enhanced cancer photothermal therapy. *IEEE Journal of selected topics in quantum electronics*, *16*(4), 989-996.

108.Ü. Özgür, V. Avrutin, H. Morkoç, (2013) Chapter 16 - Zinc oxide materials and devices grown by MBE,Elsevier, Pages 369-416,

109.Cullity, B. D. (1956). *Elements of X-ray Diffraction*. Addison-Wesley Publishing.

110.Sajjad, A., Bhatti, S. H., Ali, Z., Jaffari, G. H., Khan, N. A., Rizvi, Z. F., & Zia, M. (2021). Photoinduced fabrication of zinc oxide nanoparticles: Transformation of morphological and biological response on light irradiance. *ACS omega*, *6*(17), 11783-11793.

111.Krishna, R., Wade, J., Jones, A. N., Lasithiotakis, M., Mummery, P. M., & Marsden, B. J. (2017). An understanding of lattice strain, defects and disorder in nuclear graphite. Carbon, 124, 314-333.

112.Qi, W. H., & Wang, M. P. (2005). Size and shape dependent lattice parameters of metallic nanoparticles. *Journal of Nanoparticle Research*, *7*, 51-57.

113.B. Santara, B., Giri, P. K., Imakita, K., & Fujii, M. (2014). Microscopic origin of lattice contraction and expansion in undoped rutile TiO2 nanostructures. *Journal of Physics D: Applied Physics*, *47*(21), 215302.

114.Diehm, P. M., Ágoston, P., & Albe, K. (2012). Size-dependent lattice expansion in nanoparticles: reality or anomaly?. *ChemPhysChem*, *13*(10), 2443-2454.

115.Ahmad, M. I., & Bhattacharya, S. S. (2009). Size effect on the lattice parameters of nanocrystalline anatase. *Applied Physics Letters*, *95*(19).

116.Kalita, A., & Kalita, M. P. C. (2015). Size dependence of lattice parameters in ZnO nanocrystals. *Applied Physics A*, *121*, 521-524.

117.Sun, C. Q. (2007). Size dependence of nanostructures: Impact of bond order deficiency. *Progress in solid state chemistry*, *35*(1), 1-159.

118.Sun, C. Q. (2009). Thermo-mechanical behavior of low-dimensional systems: The local bond average approach. *Progress in Materials Science*, *54*(2), 179-307.

119.Nie, M., Zhao, Y., & Zeng, Y. (2014). Effects of annealing and laser irradiation on optical and electrical properties of ZnO thin films. Journal of Laser Applications, 26(2).

120.Thongam, D. D., Gupta, J., & Sahu, N. K. (2019). Effect of induced defects on the properties of ZnO nanocrystals: surfactant role and spectroscopic analysis. *SN Applied Sciences*, *1*(9), 1030.

121.Qadisiyah, A. (2022). Studying the effect of irradiation time in preparing zinc oxide nanoparticles prepared by microwave method.

122.Johannes, A. Z., Pingak, R. K., & Bukit, M. (2020, April). Tauc Plot Software: Calculating energy gap values of organic materials based on Ultraviolet-Visible absorbance spectrum. In *IOP conference series: materials science and engineering* (Vol. 823, No. 1, p. 012030). IOP Publishing.

123.Monemar, B. (1974). Fundamental energy gap of GaN from photoluminescence excitation spectra. Physical Review B, 10(2), 676.

124.Scafetta, M. D., Cordi, A. M., Rondinelli, J. M., & May, S. J. (2014). Band structure and optical transitions in LaFeO3: theory and experiment. Journal of Physics: Condensed Matter, 26(50), 505502.

125.Jiang, S., Fang, Y., Li, R., Xiao, H., Crowley, J., Wang, C., ... & Fang, J. (2016). Pressure-dependent polymorphism and band-gap tuning of methylammonium lead iodide perovskite. *Angewandte Chemie International Edition*, *55*(22), 6540-6544.

126.Tauc, J., Grigorovici, R., & Vancu, A. (1966). Optical properties and electronic structure of amorphous germanium. *physica status solidi (b)*, *15*(2), 627-637.

127.Mok, T. M., & O'Leary, S. K. (2007). The dependence of the Tauc and Cody optical gaps associated with hydrogenated amorphous silicon on the film thickness: αl Experimental limitations and the impact of curvature in the Tauc and Cody plots. *Journal of Applied Physics*, *102*(11).

128.Sánchez-Vergara, M. E., Alonso-Huitron, J. C., Rodriguez-Gómez, A., & Reider-Burstin, J. N. (2012). Determination of the optical GAP in thin films of amorphous dilithium phthalocyanine using the Tauc and Cody models. *Molecules*, *17*(9), 10000-10013.

129.Tauc, J. (1968). Optical properties and electronic structure of amorphous Ge and Si. *Materials research bulletin*, *3*(1), 37-46.

130.Russell, H. B., Andriotis, A. N., Menon, M., Jasinski, J. B., Martinez-Garcia, A., & Sunkara, M. K. (2016). Direct band gap gallium antimony phosphide (GaSbxP1− x) alloys. *Scientific reports*, *6*(1), 20822.

131.Abdelghani, G. M., Ahmed, A. B., & Al-Zubaidi, A. B. (2022). Synthesis, characterization, and the influence of energy of irradiation on optical properties of ZnO nanostructures. Scientific Reports, 12(1), 20016.

132.Gurylev, V., & Perng, T. P. (2021). Defect engineering of ZnO: Review on oxygen and zinc vacancies. Journal of the European Ceramic Society, 41(10), 4977-4996.

133.Wang, J., Wang, Z., Huang, B., Ma, Y., Liu, Y., Qin, X., ... & Dai, Y. (2012). Oxygen vacancy induced band-gap narrowing and enhanced visible light photocatalytic activity of ZnO. ACS applied materials & interfaces, 4(8), 4024-4030.

134.Ansari, S. A., Khan, M. M., Kalathil, S., Nisar, A., Lee, J., & Cho, M. H. (2013). Oxygen vacancy induced band gap narrowing of ZnO nanostructures by an electrochemically active biofilm. Nanoscale, 5(19), 9238-9246.

135.Xia, T., Wallenmeyer, P., Anderson, A., Murowchick, J., Liu, L., & Chen, X. (2014). Hydrogenated black ZnO nanoparticles with enhanced photocatalytic performance. RSC advances, 4(78), 41654-41658.

136.Lu, X., Wang, G., Xie, S., Shi, J., Li, W., Tong, Y., & Li, Y. (2012). Efficient photocatalytic hydrogen evolution over hydrogenated ZnO nanorod arrays. Chemical communications, 48(62), 7717-7719.

137.La Porta, F. A., Andres, J., Vismara, M. V. G., Graeff, C. F. D. O., Sambrano, J. R., Li, M. S., ... & Longo, E. (2014). Correlation between structural and electronic order–disorder effects and optical properties in ZnO nanocrystals. Journal of Materials Chemistry C, 2(47), 10164-10174.

138.Ghose, S., & Jana, D. (2019). Defect dependent inverted shift of band structure for ZnO nanoparticles. *Materials Research Express*, *6*(10), 105907.

139.Mikhailov, M. M., Neshchimenko, V. V., Li, C., & Vlasov, V. A. (2018). Blue shift in absorption edge of polycrystalline zinc oxide modified by nanoparticles before and after irradiation exposure. *Nuclear Instruments and Methods in Physics Research Section B: Beam Interactions with Materials and Atoms*, *418*, 18-26.

140.Hofmann, D. M., Pfisterer, D., Sann, J., Meyer, B. K., Tena-Zaera, R., Munoz-Sanjose, V., ... & Pensl, G. (2007). Properties of the oxygen vacancy in ZnO. Applied Physics A, 88, 147-151.

141.Lu, C. H., & Yeh, C. H. (2000). Influence of hydrothermal conditions on the morphology and particle size of zinc oxide powder. *Ceramics International*, *26*(4), 351-357.

142.Basnet, P., Chanu, T. I., Samanta, D., & Chatterjee, S. (2018). A review on bio-synthesized zinc oxide nanoparticles using plant extracts as reductants and stabilizing agents. Journal of Photochemistry and Photobiology B: Biology, 183, 201-221.

143.Kalpana, V. N., Kataru, B. A. S., Sravani, N., Vigneshwari, T., Panneerselvam, A., & Rajeswari, V. D. (2018). Biosynthesis of zinc oxide nanoparticles using culture filtrates of Aspergillus niger: Antimicrobial textiles and dye degradation studies. *OpenNano*, *3*, 48-55.

144.Saratale, R. G., Karuppusamy, I., Saratale, G. D., Pugazhendhi, A., Kumar, G., Park, Y., ... & Shin, H. S. (2018). A comprehensive review on green nanomaterials using biological systems: Recent perception and their future applications. Colloids and Surfaces B: Biointerfaces, 170, 20-35.

145.Kurtzman, C., Fell, J. W., & Boekhout, T. (Eds.). (2011). The yeasts: a taxonomic study. Elsevier.

146.Wegerhoff, S., & Engell, S. (2016). Control of the production of Saccharomyces cerevisiae on the basis of a reduced metabolic model. *IFAC-PapersOnLine*, *49*(26), 201-206.

147.Chiselitcedilla˜ a, N., Usatii, A., & Efremova, N. (2017). The effects of ZnO nanoparticles in combination with alcohol on biosynthetic potential of Saccharomyces cerevisiae.

148.Korbekandi, H., Mohseni, S., Mardani Jouneghani, R., Pourhossein, M., & Iravani, S. (2016). Biosynthesis of silver nanoparticles using Saccharomyces cerevisiae. *Artificial cells, nanomedicine, and biotechnology*, *44*(1), 235-239.

149.Parapouli, M., Vasileiadis, A., Afendra, A. S., & Hatziloukas, E. (2020). Saccharomyces cerevisiae and its industrial applications. *AIMS microbiology*, *6*(1), 1.

150.Sriramulu, M., & Sumathi, S. (2018). Biosynthesis of palladium nanoparticles using Saccharomyces cerevisiae extract and its photocatalytic degradation behaviour. *Advances in Natural Sciences: Nanoscience and Nanotechnology*, *9*(2), 025018.

151.Ramani, M., Ponnusamy, S., & Muthamizhchelvan, C. (2012). Zinc oxide nanoparticles: A study of defect level blue–green emission. *Optical Materials*, *34*(5), 817-820.

152.Bindu, P., & Thomas, S. (2014). Estimation of lattice strain in ZnO nanoparticles: X-ray peak profile analysis. *Journal of Theoretical and Applied Physics*, *8*, 123-134.

153.Singh, J., Dutta, T., Kim, K. H., Rawat, M., Samddar, P., & Kumar, P. (2018). 'Green'synthesis of metals and their oxide nanoparticles: applications for environmental remediation. *Journal of nanobiotechnology*, *16*, 1-24.

154.Huston, M., DeBella, M., DiBella, M., & Gupta, A. (2021). Green synthesis of nanomaterials. *Nanomaterials*, *11*(8), 2130.

155.Guo, L., Yang, S., Yang, C., Yu, P., Wang, J., Ge, W., & Wong, G. K. (2000). Highly monodisperse polymer-capped ZnO nanoparticles: Preparation and optical properties. *Applied physics letters*, *76*(20), 2901-2903.

156.Makarov, V. V., Love, A. J., Sinitsyna, O. V., Makarova, S. S., Yaminsky, I. V., Taliansky, M. E., & Kalinina, N. O. (2014). "Green" nanotechnologies: synthesis of metal nanoparticles using plants. *Acta Naturae (англоязычная версия)*, *6*(1 (20)), 35-44.

157.Dutta, R. K., Nenavathu, B. P., & Gangishetty, M. K. (2013). Correlation between defects in capped ZnO nanoparticles and their antibacterial activity. Journal of photochemistry and photobiology B: Biology, 126, 105-111.

158.Matussin, S. N., Rahman, A., & Khan, M. M. (2022). Role of Anions in the Synthesis and Crystal Growth of Selected Semiconductors. Frontiers in Chemistry, 10, 881518.

159.Hu, Z., Oskam, G., Penn, R. L., Pesika, N., & Searson, P. C. (2003). The influence of anion on the coarsening kinetics of ZnO nanoparticles. *The Journal of Physical Chemistry B*, *107*(14), 3124-3130.

160.Barreto, G. P., Morales, G., & Quintanilla, M. L. L. (2013). Microwave assisted synthesis of ZnO nanoparticles: effect of precursor reagents, temperature, irradiation time, and additives on nano-ZnO morphology development. *Journal of Materials*, *2013*, 1-11.

161.Zielecka, M., Bujnowska, E., & Bajdor, K. (2007). Siloxane-containing polymer matrices as coating materials. *Journal of Coatings Technology and Research*, *4*(3), 275-281.

162.Nakaya, T. (1996). Development of a staining preventive coating for architecture. *Progress in Organic coatings*, *27*(1-4), 173-180.

163.Owens, D. K., & Wendt, R. C. (1969). Estimation of the surface free energy of polymers. *Journal of applied polymer science*, *13*(8), 1741-1747.

164.Allen, K. W. (1979). The nature of adhesives. *British Polymer Journal*, *11*(2), 50-53.

165.Nun, E., Oles, M., & Schleich, B. (2002, September). Lotus-Effect®–surfaces. In *Macromolecular Symposia* (Vol. 187, No. 1, pp. 677-682). Weinheim: WILEY-VCH Verlag.

166.Zielecka, M., & Bujnowska, E. (2006). Silicone-containing polymer matrices as protective coatings: Properties and applications. *Progress in Organic Coatings*, *55*(2), 160-167.

167.Yi, B., Liu, P., Hou, C., Cao, C., Zhang, J., Sun, H., & Yao, X. (2019). Dual-cross-linked supramolecular polysiloxanes for mechanically tunable, damage-healable and oil-repellent polymeric coatings. ACS applied materials & interfaces, 11(50), 47382-47389.

168.Yilgör, E., & Yilgör, I. (2014). Silicone containing copolymers: Synthesis, properties and applications. *Progress in Polymer Science*, *39*(6), 1165-1195.

169.Zhang, J., Liu, P., Yi, B., Wang, Z., Huang, X., Jiang, L., & Yao, X. (2019). Bio-inspired elastic liquid-infused material for on-demand underwater manipulation of air bubbles. *ACS nano*, *13*(9), 10596-10602.

170.Li, C. Y., Chen, J. H., Chien, P. C., Chiu, W. Y., Chen, R. S., & Don, T. M. (2007). Preparation of poly (IPDI-PTMO-siloxanes) and influence of siloxane structure on reactivity and mechanical properties. *Polymer Engineering & Science*, *47*(5), 625-632.

171.Holten-Andersen, N., Harrington, M. J., Birkedal, H., Lee, B. P., Messersmith, P. B., Lee, K. Y. C., & Waite, J. H. (2011). pH-induced metal-ligand cross-links inspired by mussel yield self-healing polymer networks with near-covalent elastic moduli. *Proceedings of the National Academy of Sciences*, *108*(7), 2651-2655.

172.Saiz-Poseu, J., Mancebo-Aracil, J., Nador, F., Busqué, F., & Ruiz-Molina, D. (2019). The chemistry behind catechol-based adhesion. *Angewandte Chemie International Edition*, *58*(3), 696-714.

173.Koochaki, M. S., Khorasani, S. N., Neisiany, R. E., Ashrafi, A., Trasatti, S. P., & Magni, M. (2021). A highly responsive healing agent for the autonomous repair of anti-corrosion coatings on wet surfaces. In operando assessment of the self-healing process. Journal of Materials Science, 56(2), 1794-1813.

174.Mazurek, M. M., & Rokicki, G. (2013). Investigations on the synthesis and properties of biodegradable poly (ester-carbonate-urea-urethane) s. Polish Journal of Chemical Technology, 15(4), 80-88.

175.Chen, X., Liu, X., Lei, J., Xu, L., Zhao, Z., Kausar, F., & Yuan, W. Z. (2018). Synthesis, clustering-triggered emission, explosive detection and cell imaging of nonaromatic polyurethanes. Molecular Systems Design & Engineering, 3(2), 364-375.

176.Riehle, N., Götz, T., Kandelbauer, A., Tovar, G. E., & Lorenz, G. (2018). Data on the synthesis and mechanical characterization of polysiloxane-based urea-elastomers prepared from amino-terminated polydimethylsiloxanes and polydimethyl-methyl-phenyl-siloxane-copolymers. Data in brief, 18, 1784-1794.

177.Riehle, N., Thude, S., Kandelbauer, A., Tovar, G. E., & Lorenz, G. (2019). Synthesis of soft polysiloxane-urea elastomers for intraocular lens application. JoVE (Journal of Vi*sualized Experiments)*, (145), e58590.

178.Augugliaro, V., Loddo, V., Pagliaro, M., Palmisano, G., & Palmisano, L. (2010). *Clean by light irradiation: Practical applications of supported TiO2*. Royal Society of Chemistry.

179.Lee, K. M., Lai, C. W., Ngai, K. S., & Juan, J. C. (2016). Recent developments of zinc oxide based photocatalyst in water treatment technology: a review. Water research, 88, 428-448.

180.Sanchez, E., & Lopez, T. (1995). Effect of the preparation method on the band gap of titania and platinum-titania sol-gel materials. *Materials Letters*, *25*(5-6), 271-275.

181.Serpone, N., Maruthamuthu, P., Pichat, P., Pelizzetti, E., & Hidaka, H. (1995). Exploiting the interparticle electron transfer process in the photocatalysed oxidation of phenol, 2-chlorophenol and pentachlorophenol: chemical evidence for electron and hole transfer between coupled semiconductors. Journal of Photochemistry and Photobiology A: Chemistry, 85(3), 247-255.

182.Kato, S., Hirano, Y., Iwata, M., Sano, T., Takeuchi, K., & Matsuzawa, S. (2005). Photocatalytic degradation of gaseous sulfur compounds by silver-deposited titanium dioxide. Applied Catalysis B: Environmental, 57(2), 109-115.

183.Kong, M., Li, Y., Chen, X., Tian, T., Fang, P., Zheng, F., & Zhao, X. (2011). Tuning the relative concentration ratio of bulk defects to surface defects in TiO2 nanocrystals leads to high photocatalytic efficiency. *Journal of the American Chemical Society*, *133*(41), 16414-16417.

184.Chen, D., Wang, Z., Ren, T., Ding, H., Yao, W., Zong, R., & Zhu, Y. (2014). Influence of defects on the photocatalytic activity of ZnO. The Journal of Physical Chemistry C, 118(28), 15300-15307.

185.Páez, C. A., Poelman, D., Pirard, J. P., & Heinrichs, B. (2010). Unpredictable photocatalytic ability of H2-reduced rutile-TiO2 xerogel in the degradation of dye-pollutants under UV and visible light irradiation. *Applied Catalysis B: Environmental*, *94*(3-4), 263-271.

186.Zhuang, J., Weng, S., Dai, W., Liu, P., & Liu, Q. (2012). Effects of interface defects on charge transfer and photoinduced properties of TiO2 bilayer films. *The Journal of Physical Chemistry C*, *116*(48), 25354-25361.

187.Zheng, Y., Chen, C., Zhan, Y., Lin, X., Zheng, Q., Wei, K., ... & Zhu, Y. (2007). Luminescence and photocatalytic activity of ZnO nanocrystals: correlation between structure and property. *Inorganic chemistry*, *46*(16), 6675-6682.

188.Kar, S., Pal, B. N., Chaudhuri, S., & Chakravorty, D. (2006). One-dimensional ZnO nanostructure arrays: Synthesis and characterization. *The Journal of Physical Chemistry B*, *110*(10), 4605-4611.

189.Hu, H., Huang, X., Deng, C., Chen, X., & Qian, Y. (2007). Hydrothermal synthesis of ZnO nanowires and nanobelts on a large scale. *Materials Chemistry and Physics*, *106*(1), 58-62.

190.Yang, Y., Yan, H., Fu, Z., Yang, B., Xia, L., Xu, Y., ... & Li, F. (2006). Photoluminescence and Raman studies of electrochemically as-grown and annealed ZnO films. *Solid state communications*, *138*(10-11), 521-525.

191.Zheng, Y., Chen, C., Zhan, Y., Lin, X., Zheng, Q., Wei, K., ... & Zhu, Y. (2007). Luminescence and photocatalytic activity of ZnO nanocrystals: correlation between structure and property. *Inorganic chemistry*, *46*(16), 6675-6682.

192.Guo, M. Y., Ng, A. M. C., Liu, F., Djurisic, A. B., Chan, W. K., Su, H., & Wong, K. S. (2011). Effect of native defects on photocatalytic properties of ZnO. *The Journal of Physical Chemistry C*, *115*(22), 11095-11101.

193.Ischenko, V., Polarz, S., Grote, D., Stavarache, V., Fink, K., & Driess, M. (2005). Zinc oxide nanoparticles with defects. *Advanced functional materials*, *15*(12), 1945-1954.

194.Justicia, I., Ordejón, P., Canto, G., Mozos, J. L., Fraxedas, J., Battiston, G. A., ... & Figueras, A. (2002). Designed self-doped titanium oxide thin films for efficient visible-light photocatalysis. *Advanced materials*, *14*(19), 1399-1402.

195.Zhang, X., Qin, J., Xue, Y., Yu, P., Zhang, B., Wang, L., & Liu, R. (2014). Effect of aspect ratio and surface defects on the photocatalytic activity of ZnO nanorods. Scientific reports, 4(1), 4596.

196.Dulian, P., Nachit, W., Jaglarz, J., Zięba, P., Kanak, J., & Żukowski, W. (2019). Photocatalytic methylene blue degradation on multilayer transparent TiO2 coatings. *Optical Materials*, *90*, 264-272.

197.Pardeshi, S. K., & Patil, A. B. (2009). Effect of morphology and crystallite size on solar photocatalytic activity of zinc oxide synthesized by solution free mechanochemical method. *Journal of Molecular Catalysis A: Chemical*, *308*(1-2), 32-40.

198.Hickman, R., Walker, E., & Chowdhury, S. (2018). TiO2-PDMS composite sponge for adsorption and solar mediated photodegradation of dye pollutants. *Journal of water process engineering*, *24*, 74-82.

199.Di Mauro, A., Cantarella, M., Nicotra, G., Pellegrino, G., Gulino, A., Brundo, M. V., ... & Impellizzeri, G. (2017). Novel synthesis of ZnO/PMMA nanocomposites for photocatalytic applications. *Scientific reports*, *7*(1), 40895.

200.Lefatshe, K., Muiva, C. M., & Kebaabetswe, L. P. (2017). Extraction of nanocellulose and in-situ casting of ZnO/cellulose nanocomposite with enhanced photocatalytic and antibacterial activity. *Carbohydrate polymers*, *164*, 301-308.

201.Ren, Y., Li, W., Cao, Z., Jiao, Y., Xu, J., Liu, P., ... & Li, X. (2020). Robust TiO2 nanorods-SiO2 core-shell coating with high-performance self-cleaning properties under visible light. *Applied Surface Science*, *509*, 145377.

202.Chiappara, C., Arrabito, G., Ferrara, V., Scopelliti, M., Sancataldo, G., Vetri, V., ... & Pignataro, B. (2021). Improved photocatalytic activity of polysiloxane TiO2 composites by thermally induced nanoparticle bulk clustering and dye adsorption. *Langmuir*, *37*(34), 10354-10365.

203.Aleeva, Y., Ferrara, V., Bonasera, A., Martino, D. C., & Pignataro, B. (2021). Superhydrophobic TiO2/fluorinated polysiloxane hybrid coatings with controlled morphology for solar photocatalysis. Colloids and Surfaces A: Physicochemical and Engineering Aspects, 631, 127633.

Appendix figures and tables

Figure 1. Graphic showing the scale of nanoparticles, including organic compounds, viruses, bacteria, and cells compared to a macroscale

Figure 2: Density of states for metals (left) and semiconductors (right). The Fermi level is in the middle of the band for metals, and kT should exceed the energy jump between levels even at room temperature and for nanometric dimensions. For semiconductors, the jump is larger and increases for smaller sizes (bottom).

Figure 3. Graphic showing the top-down approach and the bottom-up approach.

Figure 4. Some relevant areas in which nanotechnologies have found established applications.

Figure 5. Physical properties of ZnO

Figure 6. Stick and ball representation of ZnO crystal structures: (a) cubic rocksalt, (b) cubic zinc blende, and (c) hexagonal wurtzite. The shaded grey and black spheres denote Zn and O atoms, respectively

Figure 7. Schematic representation of a wurtzite ZnO structure having lattice constants *a* in the basal plane and *c* in the basal direction; *u* parameter is expressed as the bond length, or the nearest-neighbour distance *b* divided by *c* (0.375 in ideal crystal), and α and β (109.47° in ideal crystal) are the bond angles.

Figure 8. Major synthetic techniques used for ZnO nanoparticle synthesis.

Figure 9. Diagram of vapor–liquid–solid deposition. The Au catalyst forms eutectic alloy drops that become supersaturated allowing for ZnO nanowires to form.

Figure 10. Diagram of physical vapor deposition. The two-temperature zone furnace consists of high temperature zone where sublimation occurs and a low-temperature zone where sublimated ZnO deposits onto the substrates. Ar is usually used as the carrier while O2 is used as the reactant gas.

Figure 11. Precursors for the biosynthesis of ZnO nanoparticles

Figure.12. Different structures of ZnO; one dimension: (a) nanospings, (b) nanorings, (c) nanohelix, (d) nanocombs, (e) nanowires, (f) nanorods; two sizes: (g) nanosheets, (h) nanopellets, (i) nanoplates; three dimensions: (k) and (l) nanoflowers, (m) nanomesosphere; (n) nanourchins

Figure 13. Applications of nano-structured zinc oxide

Figure 14. Classification of polymeric materials.

Figure 15. Macromolecular structures of polymers: a) linear, b) cross-linked c) branched.[5]

Figure 16 Amorphous polymer

Figure 17. Different types of isomerism

Figure 18. The physical state of polymeric materials as a function of temperature: state transitions.[67]

Figure 19. Applications of polymers.

Figure 20. Photographic representation of the chemical synthesis of ZnO with blue light (left), red light (center), and white light (left) in the incubator including an adapted LED system

Figure 21. Photography of the apparatus for biological synthesis of ZnO with light in the incubator including an adapted LED system.

Figure 22. Setup of white light irradiation experiments in the incubator including an adapted LED system

Figure 23. (a) The mixture containing the copolymer and ZnO is heated to 80 °C for 1 hour, allowing partial removal of EtOAc. (b) While still at 80 °C, the nanomaterial/polymer blend is drop-cast onto a glass slide to produce a thick coating until the EtOAc is completely removed by drying the composite film at 80 °C.(c)Photograph of the casting on a glass slide and the resulting system at a concentration of 10% w/v of the ZnO nanomaterial.

Figure 24. Geometric representation of Bragg's law.

Figure 25. Diagram of an SEM microscope

Figure 26. Graphic representation of the phenomenon that occurs when a beam of light passes from an optically denser medium to one that is optically less dense.

Figure 27. Schematic representation of ATR-FTIR system

Figure 28. Diagram of the photoemission phenomenon

Figure 30. Operating principle of NMR.

Figure 31. Methylene blue molecule structure

Figure 32. Mechanism of photoinduced ZnO NPs synthesized under different light conditions.

Figure 33. X-ray diffraction (XRD) spectra of ZnO: left XRD spectrum of ZnO synthesized with the precursor zinc nitrate, middle XRD spectrum of ZnO synthesized with the precursor zinc acetate and right XRD spectrum of ZnO synthesized with the precursor zinc chloride with and without irradiation.

Figure 34. The ATR-FTIR spectra for the ZnO NPs before and after irradiations. left ATR-FTIR spectrum of ZnO synthesized with the precursor zinc nitrate, middle ATR-FTIR spectrum of ZnO synthesized with the precursor zinc acetate, and right ATR-FTIR spectrum of ZnO synthesized with the precursor zinc chloride.

Figure 35. Tauc plot for ZnO NPs synthesized with the precursor zinc chloride without irradiation.

Figure 36. The SEM images of the ZnO powders before and after irradiation with Red light for zinc nitrate precursor. The scale bars in the figure SEM are 4 µm.

Figure 37. The SEM images of the ZnO powders before and after irradiation with Red light for zinc acetate precursor. The scale bars in the figure SEM are 1 µm and 4 µm.

Figure 38. The SEM images of the ZnO powders before and after irradiation with Red light for zinc chloride precursor. The scale bars in the figure SEM are 4 µm.

Figure 39. X-ray diffraction (XRD) spectra of ZnO: left XRD spectrum of ZnO synthesized with the zinc nitrate precursor, middle XRD spectrum of ZnO synthesized with the zinc acetate precursor, and right XRD spectrum of ZnO synthesized with the zinc chloride precursor with the use of brewer's yeast and combination of brewer's yeast and white LED radiation.

Figure 40. The ATR-FTIR spectra for the ZnO NPs: left ATR-FTIR spectrum of ZnO synthesized with the precursor zinc nitrate, middle ATR-FTIR spectrum of ZnO synthesized with the precursor zinc acetate, and right ATR-FTIR spectrum of ZnO synthesized with the precursor zinc chloride with the use of brewer's yeast and combination of brewer's yeast and white LED radiation.

Figure 41. Tauc plot for ZnO NPs synthesized with the precursor zinc chloride with yeast and irradiation.

Figure 42. The SEM images of the biologically synthesized ZnO powders: top left the ZnO sample (N_CFE_WL), top right the ZnO sample (A_CFE_WL) and bottom the sample (Cl_CFE_WL) The scale bars in the figure SEM are 4 µm.

Figure 43. The design of the copolymer and the specific monomers used in the synthesis.

Figure 44. ^{1}H-NMR spectra of the copolymer and relative magnification to the region between 6.0 and 8.0 ppm of the spectrum.

Figure 45. ^{13}C-NMR spectra of the copolymer

Figure 46. ATR-FTIR spectra on the left of the copolymer (A), dopamine hydrochloride (B), isophorone diisocyanate (C), and the N-terminated PDMS (D); on the right spectrum of the copolymer alone.

Figure 47. XPS spectrum of the supramolecular copolymer

Figure 48. Illustration of the process of chlorophyll photosynthesis and related chemical reactions.

Figure 49. Illustration of photo-reduction and photo-oxidation reactions.

Figure 50. UV-vis spectrum of the MB solution under 1 sun after treatment with ZnO synthesized with red light and using zinc chloride as a precursor

Figure 51. MB degradation kinetic curves under 1 Sun obtained for the different ZnO powders. The graphs on the left correspond to the samples synthesized chemically and irradiated with the different lights for the different precursors, those on the right correspond to the samples synthesized biologically and biologically combined with white light for the different precursors.

Figure 52. (A) UV-vis spectra of the MB solution after treatment with copolymer/ZnO (5% m/v) and (A1) MB degradation kinetic curve under 1 Sun obtained for the corresponding system. (B) UV-vis spectra of the MB solution after treatment with copolymer/ZnO (10% m/v) and (B1) MB degradation kinetic curve under 1 Sun obtained for the corresponding system.

Figure 53. ATR-FTIR spectrum for the copolymer/ZnO system (10 wt%) before or after irradiation under solar irradiation equal to 1 Sun.

Table 1. Quantity of each zinc salt used in the synthesis of ZnO for chemicals.

Tabel 2. mL of each zinc salt solution and yeast solution (CFE) used in the biological synthesis of ZnO.

Table 3. average crystallite size (D), dislocation density(δ), lattice strain (ε) before and after irradiation with LED lights for samples synthesized with zinc nitrate, zinc acetate, and zinc chloride.

Table 4. The lattice structure parameters (2 θ_{001} (°),2 θ_{002} (°), a (Å) c (Å) the degree of crystallinity (% DC), cell volume (V ($Å^3$)) and the length of the Zn–O bond L (Å)) before and after irradiation with LED lights for samples synthesized with zinc nitrate, zinc acetate, and zinc chloride.

Table 5. The wave number values for the three irradiated samples, together with the corresponding value for the control.

Table 6. Energy gap (E_g) values for the three irradiated samples, together with the corresponding value for the control

Table7. ZnO crystallite size (D), dislocation density(δ), and lattice strain(ε) for biological synthesis synthesized with zinc nitrate, zinc acetate, and zinc chloride.
Table 8. Lattice structure parameters (a, c) degree of crystallinity (% DC), cell volume (V), and Zn–O bond length (L) for biological synthesis for samples synthesized with zinc nitrate, zinc acetate, and zinc chloride.

Table 9. The wavenumber values for the biological samples, together with the corresponding value for the control.

Table 10. Gap energy (Eg)values for the biological samples, together with the corresponding value for the control.

Table 11. Assignments of the chemical shifts in the ^1H spectrum of the copolymer and relative chemical shifts of the individual monomers present in the literature.

Table 12. Band assignments in ATR-FTIR spectra of copolymer.

Table 13. Experimental and stoichiometric atomic concentrations expressed in percentages.

Table 14. Photodegradation rates for ZnO samples synthesised with the different precursors and irradiated with white, blue, and red light and respective controls.

Table 15. Photodegradation rates for biologically synthesized ZnO samples and biologically combined with white light and respective controls.

Table 16. Apparent rate constants (expressed in min^{-1}) of the degradation of the MB solution under solar irradiation of 1 Sun for the different precursors and irradiated with white, blue, and red light and respective controls.

Table 17. Apparent rate constants (expressed in min-1) of MB solution degradation under solar irradiation equal to 1 Sun for biologically synthesized and biologically combined ZnO samples with white light and respective controls.

Table 18. Apparent rate constants (expressed in min-1) of MB solution degradation under solar irradiation equal to 1 Sun for samples Copolymer/ZnO (5% wt) and Copolymer/ZnO (10% wt).

PHD IN Technology and Sciences for the Human Health, XXXVI CYCLE

Courses with final evaluation

1. Course “Physical Chemistry of Materials”, Laurea Magistrale in Chimica. Reference Teacher prof. Bruno Pignataro, A.A. 2021-2022
2. Course “Theories, techniques and instrumentations for the determination of bioanalites. Reference Teacher Dr. Giuseppe Arrabito A.A. 2021-2022
3. Course 3D Microscopy and super resolution Reference Teacher Dr. Giuseppe Sancataldo A.A. 2021-2022
4. Course Microbiologia con Esercitazioni. Reference Teacher Dr.Alessandro Presentato. A.A. 2021-2022

Conferences/workshop attendance

1. I vaccini e le nuove tecnologie dott.ssa MARIAGRAZIA PIZZA Senior Scientific Director Bacterial Vaccines GSK Vaccines, Siena,
2. La chimica al tempo del covid, Commissione Rapporti con l’Industria della Società Chimica Italiana (SCI).
3. La carta europea dei ricercatori, Università degli studi di Palermo
4. Understanding virus assembly via quantitative fluorescence microscopy, Prof. Salvatore Chiantia,– Cell Membrane Biophysics – University of Potsdam
5. Open Sesame: how SARS-CoV-2 enters and infects human cells, Prof. Giuseppe Balistreri, Group Leader and Adjunct Professor University of Helsinki, Finland and Adjunct Associate Professor The University of Queensland, Brisbane, Australia
6. SARS-CoV-2 vaccines: how are they made, and will they work?”. Prof. Giuseppe Balistreri, Group Leader and Adjunct Professor University of Helsinki, Finland and Adjunct Associate Professor The University of Queensland, Brisbane, Australia.
7. Reaxys SCI Early Career Researcher Award 2021
8. Training AFM: Microscopia a FORZA ATOMICA, Prof. Gianpiero Buscarino ATEN CENTER
9. How to design and set up confocal fluorescence microscopy experiments: fundamentals, tips and tricks. Dr Giuseppe Sancataldo e Prof Valeria Vetri ATEN CENTER
10. Meeting online con UAI
11. SHARPER 2020
12. CONVEGNO DELLA SEZIONE SICILIA 2021, SOCIETA' CHIMICA ITALIANA, piattaforma online.

13. Alternanza scuola-lavoro (PCTO- “Dentro il colore”)
14. Sharper 2022- La notte dei ricercatori -. Come combattere la resistenza multifarmaco: l’aiuto che ci forniscono le nanotecnologie.
15. Congresso Congiunto delle Sezione Calabria e Sicilia
16. FIRST SYMPOSIUM FOR YOUNG CHEMISTS; INNOVATION AND SUSTAINABILITY.
17. XL CONVEGNO NAZIONALE DELLA DIVISIONE DI CHIMICA ORGANICA DELLA SOCIETA' CHIMICA ITALIANA

Schools’ attendance (Summer, Winter, etc.)

1. 1st Summer School: Surface-Confined Synthesis and Advanced Surface Characterization Tools, Project Coordinator: Prof. Davide Bonifazi, University of Vienna, Austria School Organizers: Prof. Willi Auwärter and Prof. Ruben Costa, Technische Universität München, Germany, online platform Zoom.

Presented Posters at Conferences/workshop

1. 20-23 Giugno 2022 “Design and characterization of self-cleaning and antibacterial surfaces functionalized with nanocomposites for biosafety applications”. First Symposium for young chemists; Innovation and Sustainability (SYNC 2022 Roma).
2. XL CONVEGNO NAZIONALE DELLA DIVISIONE DI CHIMICA ORGANICA DELLA SOCIETA' CHIMICA ITALIANA, Università degli Studi di Palermo , Poster:Nanosponge-C3N4 composites as photocatalysts for selective partial alcohol oxidation in aqueous suspensions.
3. Congresso Congiunto delle Sezione Calabria e Sicilia, Universita' degli studi di Palermo. Poster: Synthesis and Characterization of Zinc Oxide Nanopowders: Comparative Analysis of Chemical and Biological Routes and their Integration into a Polymeric Matrix for biocidal surfaces.
4. FIRST STEBICEF YOUNG RESEARCH WORKSHOP POSTER: Nanocomposites for the development of selfcleaning and antibacterial surfaces with applications in the field of biosecurity

Papers (published, submitted)

1. Arrabito, G., Delisi, A., Giuliano, G., Prestopino, G., Medaglia, P. G., Ferrara, V., **Arcidiacono,** F., Scopelliti, M., Chillura Martino, D F., Pignataro, B. Self-Cleaning Bending Sensors Based on Semitransparent ZnO Nanostructured Films. ACS Applied Engineering Materials, 1(5), 1384-1396 https://doi.org/10.1021/acsaenm.3c00082

2. García-López, E. I., **Arcidiacono**, F., Di Vincenzo, A., Palmisano, L., Lo Meo, P., & Marcì, G. (2023). Nanosponge-C3N4 composites as photocatalysts for selective partial alcohol oxidation in aqueous suspension. Photochemical & Photobiological Sciences, 22(7), 1517-1526 https://doi.org/10.1007/s43630-023-00394-5

3. Sciatti, A., Marzullo, P., Chirco, G., Piacenza, E., **Arcidiacono**, F., Dellù, E., & Martino, D. F. C. (2023). Bone diagenesis of archaeological human remains from Apulia (Italy) investigated by ATR-FTIR and XRF spectroscopy. Materials Letters, 335, 133782. https://doi.org/10.1016/j.matlet.2022.133782

4. Paola Marzullo, Lucia Nucci, Elena Piacenza, **Federica Arcidiacono**, Delia Francesca Chillura Martino, Rare Japanese fabrics of the Ragusa-Kiyohara collection.A spectroscopic characterization Rivista: IMEKO TC-4 International Conference on Metrology for Archaeology and Cultural

Other activities:
Periodo di formazione estero, presso: Management Center Innsbruck (MCI) Luogo: Innsbruck (AUSTRIA) Durata: 6 (mesi).

Synthesis and characterisation of zinc oxide nanomaterials using LED light. Characterisation of nanostructured material based on polymers and zinc oxide nanoparticles.